

# Sheffield Hallam University

*The structure and properties of manganese maraging alloys.*

TEKIN, A.

Available from the Sheffield Hallam University Research Archive (SHURA) at:

<http://shura.shu.ac.uk/20432/>

## A Sheffield Hallam University thesis

This thesis is protected by copyright which belongs to the author.

The content must not be changed in any way or sold commercially in any format or medium without the formal permission of the author.

When referring to this work, full bibliographic details including the author, title, awarding institution and date of the thesis must be given.

Please visit <http://shura.shu.ac.uk/20432/> and <http://shura.shu.ac.uk/information.html> for further details about copyright and re-use permissions.

# **THE STRUCTURE AND PROPERTIES OF MANGANESE MANGANING ALLOYS**

A. Tekin

A thesis submitted in partial fulfilment of the  
requirements of  
Sheffield Hallam University  
for the degree of Doctor of Philosophy

Department of Metallurgy

1974

ProQuest Number: 10701078

All rights reserved

INFORMATION TO ALL USERS

The quality of this reproduction is dependent upon the quality of the copy submitted.

In the unlikely event that the author did not send a complete manuscript and there are missing pages, these will be noted. Also, if material had to be removed, a note will indicate the deletion.



ProQuest 10701078

Published by ProQuest LLC (2017). Copyright of the Dissertation is held by the Author.

All rights reserved.

This work is protected against unauthorized copying under Title 17, United States Code  
Microform Edition © ProQuest LLC.

ProQuest LLC.  
789 East Eisenhower Parkway  
P.O. Box 1346  
Ann Arbor, MI 48106 – 1346

## PREFACE

This dissertation is submitted for the degree of Doctor of Philosophy of the Council for National Academic Awards. The research was carried out between January, 1971 to June, 1974 in the department of Metallurgy. During this period the author has attended the following courses:

- (i) Electron microscopy
- (ii) Quantitative x-ray diffraction
- (iii) Numerical analysis
- (iv) High strength steels

The author has also attended the following conferences:

- (i) Influence of second phase particles on the properties of steels. Scarborough (BISRA/ISI 24-24 March, 1971).
- (ii) Modern metallography in Metallurgy, Liverpool (Inst. Met. 28th to 30th September, 1971.)
- (iii) Grain boundary conference, London (Inst. Met. ISI 25th November, 1971.)

The results obtained and the theories developed are to the best of my knowledge original except where reference is made to the work of others.

No part of this dissertation has been submitted for a degree at any University or College.

## ABSTRACT

The microstructures of Fe-Mn-Co and Fe-Mn-Co-Mo alloys in various conditions of heat treatment have been studied using optical and thin foil transmission electron microscopy techniques. After homogenizing in the austenite phase field, the structure at room temperature is lath martensite (bcc -  $\alpha$  - martensite, and cph -  $\epsilon$  martensite) or lath martensite and retained austenite. The influence of ageing on the matrix structure has been examined in detail by volume fraction phase analysis using X-ray diffraction. The martensitic structure can be strengthened by ageing at temperatures in the range 350<sup>o</sup>- 550<sup>o</sup>C. The precipitates responsible for this strengthening were tentatively identified as fcc  $\delta$  - phase and a hexagonal phase (A<sub>3</sub>B type). Overaging in these alloys is mainly due to the reversion of the matrix to austenite. The effect of ageing on the ductility and toughness of the alloys has shown that embrittlement occurs as a result of ageing in the temperature range between 350<sup>o</sup>- 500<sup>o</sup>C. Improvement in toughness of the alloys can be achieved by ageing above the embrittlement range without severely reducing the strength of the alloys.

The influence of deformation on the matrix structure both at room temperature and -196<sup>o</sup>C was also investigated. The relationship between mechanical properties and matrix structure after deformation and deformation and ageing has also been studied. The best combination of strength and toughness was achieved by a deformation and ageing process. This was due to a combination of the precipitate dispersion in a fine substructure.

# CONTENTS

1. INTRODUCTION
2. REVIEW OF LITERATURE
  - 2.1 Martensitic Transformations
    - 2.1.1 General characteristics of Martensitic Transformations.
    - 2.1.2 Crystallographic Theory of Martensitic Transformations.
  - 2.2 Modes of Austenite Decomposition
    - 2.2.1 Equiaxed Ferrite
    - 2.2.2 Massive Ferrite
    - 2.2.3 Lath Martensite
      - 2.2.3.1 Crystallography of lath Martensite
    - 2.2.4 Twin Martensite
    - 2.2.5 Epsilon Martensite
  - 2.3 Stacking Faults in the FCC Structure
    - 2.3.1 Nature of Stacking faults
    - 2.3.2 The Role of Stacking Faults in Martensitic Transformations.
      - 2.3.2.1 The FCC  $\rightarrow$  CPH Transformation
      - 2.3.2.2 The CPH  $\rightarrow$  BCC Transformation
    - 2.3.3. Measurements of Stacking Fault Energy
      - 2.3.3.1 Node Radii Technique
      - 2.3.3.2 Twin Frequency Method
  - 2.4 Strength of Martensite
    - 2.4.1 Solid Solution Hardening by Interstitial elements.
    - 2.4.2 Solid Solution Hardening by Substitutional elements.
    - 2.4.3 Grain size
    - 2.4.4. Substructure Strengthening.

- 2.5 The Influence of Deformation on the Martensitic Transformations.
- 2.6 Fe-Mn Alloys.
- 2.7 Fe-Mn-Co Alloys
- 2.8 Maraging Steels.
  - 2.8.1 Manganese Maraging Alloys
  - 2.8.2 Austenite Reversion
- 2.9 Brittleness in Manganese Steels
- 3. EXPERIMENTAL PROCEDURE
  - 3.1 Alloy Preparation
  - 3.2 Specimen Preparation
  - 3.3 Thin Foil Preparation
  - 3.4 Dilatometry
  - 3.5 X-ray Diffraction
  - 3.6 Tensile Testing
  - 3.7 Impact Testing
  - 3.8 Hardness Testing
- 4. EXPERIMENTAL RESULTS
  - 4.1 Dilatometric Analysis
  - 4.2 Matrix Composition After Water Quenching
  - 4.3 Martensite Transformation
    - 4.3.1 Habit Plane Determination
    - 4.3.2 Orientation Relationship between  $\gamma$ ,  $\epsilon$  and  $\alpha'$
  - 4.4 The Effect of Deformation on the Matrix Structure
    - 4.4.1 Deformation at Room Temperature
    - 4.4.2 Deformation at  $-196^{\circ}\text{C}$
  - 4.5 Ageing Behaviour
    - 4.5.1 Ageing After Water Quenching

- 4.5.2 Deformation and Ageing
- 4.6 Formation of Precipitate
- 4.7 Austenite Reversion
- 4.8 Mechanical Properties of Quenched and Aged Alloys.
  - 4.8.1 Toughness Data
  - 4.8.2 Hardness Data
  - 4.8.3 Tensile Test
- 5. DISCUSSION
- 6. CONCLUSIONS
- 7. ACKNOWLEDGEMENTS

In recent years, because of the cost involved, interest has been shown in reducing the nickel content of maraging steels. Manganese was one of the elements chosen for replacement because of its cheapness and close similarity to nickel in its effect on the structure and properties of iron alloys.

Fe-Mn-Co alloys have been previously reported to suffer from intergranular embrittlement in the quenched and also aged condition. (43) This embrittlement is also related to the occurrence of bcc lath martensite. On the contrary,  $\epsilon$  martensite has been reported to have a much higher ductility than lath martensite. In view of the brittleness the aim of the present work has been to investigate the alloys in the range where  $\epsilon$  martensite occurs.

Two base compositions have been studied in detail i.e., Fe-13%Mn-5%Co and Fe-17%Mn-7%Co. These two compositions were chosen because the equilibrium matrix composition at room temperature consisted of the  $\alpha$  and  $\epsilon$  phases and the  $\alpha$ ,  $\epsilon$  and  $\delta$  phases respectively.

The influence of precipitation in the different matrices has been investigated using Molybdenum additions of approximately 2% and 5%.

The final part of this thesis is concerned with the relationship between microstructure and mechanical properties obtained by different mechanical and thermal treatments or a combination of the two types of treatments.

## 2. REVIEW OF LITERATURE

### 2.1 Martensitic Transformation

#### 2.1.1 General Characteristics of Martensitic Transformation

The Martensitic transformation is a diffusionless process. Martensite forms by a shear mechanism which involves minimum atomic displacement without interchange in the position of neighbouring atoms. Transformation proceeds athermally and to induce complete transformation requires continuous cooling through the  $M_s-M_f$  temperature range. In some cases however, isothermal martensitic transformations have been reported. (1) (2)

There is a shape strain associated with transformation as a result of which surface tilts are observed when a pre-polished specimen is transformed martensitically. However, this is not a sufficient criterion for defining the martensitic transformation as surface tilting has been reported in other types of phase transformation. (3) (4)

The parent and product phases in a martensitic transformation are crystallographically related across a habit plane. The habit plane is defined as the common interphase between parent and product phase.

The martensitic phase can exist in many crystal forms depending upon the alloy system. In some cases two martensitic crystal structures may occur in one alloy system as in Fe-Mn alloys where bcc and cph martensite are often observed. (48) (88)

Martensitic transformation can sometimes be induced above

the Ms temperature on deforming the parent lattice. The highest temperature at which martensite can form under stress is called the Md temperature. The morphology and crystal structure of the strain induced martensite may or may not be the same as the martensite formed in the absence of deformation.

If the parent phase is held for a certain time during transformation before cooling further, transformation does not start immediately on cooling to the lower temperature. This phenomenon is called stabilisation. The amount of martensite formed at the lower temperature due to stabilisation is also less than that produced by direct cooling.

### 2.1.2 Crystallographic Theory of Martensitic Transformation

Early work on the theory of martensitic transformations was based on the idea that the body centred tetragonal lattice could be obtained from the face centred lattice by approximately 20% contraction along the 'z' axis and 12% expansion along the 'x' and 'y' axes of the martensite. This distortion is known as Bain strain or Bain distortion and involves very small atomic movements. (5) (See Fig.6).

In 1930 Kurdjumov and Sachs determined the orientation relationship between the parent ( $\gamma$ ) and the product ( $\alpha$ ) phases

$$(111)_{\gamma} // (110)_{\alpha} \text{ and } \langle \bar{1}\bar{1}0 \rangle_{\gamma} // \langle \bar{1}\bar{1} \rangle_{\alpha}$$

They proposed that this was accomplished by two shears,  $(111)_{\gamma} \langle 112 \rangle_{\gamma}$

and  $(112)_{\alpha} \langle 111 \rangle_{\alpha}$ . However this was found insufficient for determining the orientation relationship and the relationship has been associated with a  $(225)_{\gamma}$  or a  $(111)_{\gamma}$  habit plane. Later

(7)

Nishiyama determined a relationship which differed from the Kurdjumov-Sachs relationship by a rotation of  $5^{\circ}16'$  about (011) plane. The orientation relationship was as follows:

$$(111)_{\gamma} // (110)_{\alpha} \quad \text{and} \quad \langle 211 \rangle_{\gamma} // \langle 110 \rangle_{\alpha}$$

He proposed that the transformation resembled twinning since only a single shear, on  $(111)_{\gamma} \langle 112 \rangle_{\gamma}$  was involved. This shear was also insufficient to produce the product phase from parent phase. It is therefore a  $(259)_{\gamma}$  habit plane <sup>which</sup> is associated with the relationship.

(8)

Greninger and Troiano suggested a shear theory which successfully predicted the observed habit plane, orientation relationship and shape deformation for a number of martensitic transformations. This theory is phenomenological and involves a Bain distortion occurring simultaneously with an inhomogenous shear. The theory applies reasonably well to Fe-C, Fe-Ni and Fe-Ni-C martensites with a  $(259)_{\gamma}$  habit plane by supposing that slip or twinning occurs on  $(112)_{\gamma}$  plane.

(9)

According to Wechsler, Lieberman and Read the theories of martensitic transformations may be simplified into the forms:

$E = RGF$  where

E is the total shape change

R is the rigid body rotation

G is the lattice invariant shear

F is the homogenous lattice deformation or Bain strain

Total lattice deformation which relates the two cells

in their correct orientation relationship is produced by the combination of Bain strain and rigid body rotation.

The lattice correspondence relates the atom positions in the parent phase to their positions in the martensitic product phase. The Bain correspondence is the most likely for fcc to bcc martensitic transformation since it involves the smallest atom movement. This relationship may be regarded as a homogeneous deformation of one lattice into another. A geometrical development indicates that in order to produce the observed habit plane a further deformation is required. This is the lattice invariant strain which produces an undistorted plane to exist between parent and product. The condition of an invariant plane strain along the habit plane is only realised by the introduction of some simple shear deformation, e.g., twinning or slip. Since the habit plane is unrotated and undistorted a rigid body rotation is required in order to rotate the habit plane back into the same position in the parent phase prior to homogeneous deformation.

(10)

The Bowles-Mackenzie theory is basically the same except that a Dilatation Parameter is introduced to allow a small amount of distortion in the habit plane, thus altering the Bain principal strains and therefore the predicted habit plane. This theory infers that shears are performed on two planes so that each produces an invariant plane strain possibly simultaneous twinning on two different planes. The theory may be represented by matrix algebra as follows:

$$E \cdot \bar{G}^{-1} = R \cdot F \quad \text{Where}$$

$\bar{G}^{-1}$  = lattice invariant shear in the opposite direction

to G

The only variable which can be altered is  $G$ , the lattice invariant shear.

Although the Bowles-Mackenzie theory also predicts a  $(225)\gamma$  habit plane there is no experimental justification for the inclusion of a Dilatation parameter. However, the use of multiple shear e.g., twinning on intersecting planes does predict the  $(225)\gamma$  habit plane without including the dilatation parameter.

## 2.2 Modes of Austenite Decomposition

A number of transformation products may be formed when an alloy is cooled from the austenite phase field to some temperature at or below ambient.

### 2.2.1 Equiaxed Ferrite

Austenite decomposes to ferrite during cooling by long range diffusion and growth. The product phase is body centred cubic with a low dislocation density. The growth of the product is unaffected by the prior austenite grain size and no surface tilting or shape change occurs.

### 2.2.2 Massive Ferrite

A recent review of massive transformations has been made by (11) Massalski. Massive ferrite occurs with more rapid cooling rates and it depends only on short range diffusion. Massive ferrite consists of irregular ferrite grains which are often difficult to distinguish from equiaxed ferrite by optical microscopy. It has been suggested that over-etching produces etch pitting and that x-ray line broadening (12) due to the high dislocation density is also observed.

### 2.2.3 Lath Martensite

Lath martensite is defined as a series of straight sided  
slabs which do not cross the prior grain boundaries and do not occur  
in more than four orientations within any single austenite grain.  
Lath martensite transformation generally occurs athermally. There  
are however, a number of iron alloys in which laths are produced  
isothermally. In these cases the Ms temperature shows a slight  
decrease when the cooling rate is increased. There is a close  
similarity between isothermally formed lath martensite and bainite. (13)  
Lath martensite is sometimes referred to as "Massive Martensite", (14)  
"Slipped Martensite" (15) and "Self accommodating Martensite". (16)

Massive Martensites are observed in pure iron, (17) (18)  
(19) Fe-Cr, (20) Fe-Cu, (21) Fe-N, (22) Fe-C and (23) Fe-Ni alloys.

Examination by thin foil electron microscopy has revealed  
that the structure consists of a series of heavily dislocated laths  
with widths ranging from 0.2 - 1.0  $\mu\text{m}$  and lengths 10 - 50  $\mu\text{m}$ . The  
width of the laths decreases with decreasing transformation temper-  
ature and also increasing amount of alloying elements. (24) (25) The  
increasing wavy appearance of the laths with increasing transform-  
ation temperature is taken as an indication that a recovery process  
has taken place after transformation. (24)

The observation of surface tilting on a pre-polished surface  
is thought to be related to the parallel bundles of laths which are  
observed in the microstructure after etching. (23) (26) (27)

### 2.2.3.1 Crystallography of Lath Martensite

The predominant orientation relationship for lath martensite is consistent with the Kurdjumov-Sachs orientation relationship,  $\{111\}_{\gamma} // \{110\}_{\alpha} \langle 110 \rangle_{\gamma} // \langle 111 \rangle_{\alpha}$  with a  $\{111\}_{\gamma}$  habit plane. Although the  $\{111\}_{\gamma}$  plane is generally accepted as the habit plane of lath martensite, different habit planes have been observed in a number of alloys. Notable amongst these are alloys with low stacking faults energies such as 18% Cr 8% Ni stainless steels. Three principal habit planes have been previously reported in a number of alloys, e.g.,  $(225)_{\gamma}$ <sup>(28)</sup>,  $(259)_{\gamma}$ <sup>(29)</sup> and  $(112)_{\gamma}$ <sup>(30)</sup>.

Shear on the system  $(110)_{\gamma} \langle 110 \rangle_{\gamma} = (112)_{\alpha} \langle 11\bar{1} \rangle_{\alpha}$  may account for both the  $\{259\}_{\gamma}$  and  $\{225\}_{\gamma}$  habit planes but this is unable to predict the  $\{111\}_{\gamma}$  habit plane. Kelly et al<sup>(30) (31)</sup> have observed that shear  $(111) \langle 1\bar{2}1 \rangle_{\gamma} = (101)_{\alpha} \langle \bar{1}01 \rangle_{\alpha}$  could satisfactorily predict the  $(\bar{1}\bar{1}2)_{\gamma}$  habit plane in 18% stainless steels. They also concluded that adjacent lath pairs must be twin related as this is the way of achieving four variants of the  $(112)_{\gamma}$  habit plane in any austenite grain.

(23)

Later Bryans et al suggested that the total shape change is about  $6\frac{1}{2}^{\circ}$  shear along  $\langle 110 \rangle_{\alpha}$  direction but this leads to a distortion in the habit plane. He also proposed that this distortion is accommodated by an adjacent lath formed in the opposite shear direction. Distortion may disappear by this mechanism but this does not take into account distortion brought about on a single lath produced by the transformation.

The orientation relationship between adjacent laths by assuming Kurdjumov-Sachs relationship is classified as follows:-

- (a) Adjacent laths are of the same orientation and rotated  $180^\circ$  about the interface normal to produce a separating boundary.
- (b) Adjacent laths are twin related.
- (c) Adjacent laths are related by  $10^\circ$  about the interface normal.

Case (c) is reported to be the most favoured condition by many workers. (13) (19) Case (b) is also reported by Kelly et al. (32)

However, Chilton et al, (33) while agreeing with the idea that adjacent laths take up different variation of the Kurdjumov-Sachs relationship, suggested that laths are not always twin related. They proposed that there were four groups of relationship, but since two of them could yield diffraction patterns in which the zone axis differs by less than  $10^\circ$  from twin orientation, and also the limited accuracy of electron diffraction techniques. The relationship between adjacent laths is slightly altered. (33)  
This is as follows:-

- (a) Less than  $5^\circ$  off twin relationship
- (b) More than  $5^\circ$  off twin relationship
- (c)  $10^\circ$  misorientated about  $\langle 110 \rangle_\alpha$  direction.

The growth direction of lath martensite has generally been observed to be along the  $\langle 111 \rangle_\alpha$  direction although laths lying parallel to the  $\langle 110 \rangle_\alpha$  direction have also been reported. (19)

#### 2.2.4 Twinned Martensite

Twinned martensite is produced in iron based alloys by the formation of twins to accommodate the habit plane misfit. (34) The crystal structure change from slipped martensite to twinned martensite in Fe-C and Fe-Ni alloys is associated with a change from bcc to bct lattice at approximately 2.85 w.t% interstitial concentration. (35)

(31) According to Kelly the transformation from slipped to twinned martensite in Fe-C alloys is associated with a change in their habit plane from a  $(111)_\gamma$  plane to the  $\{225\}_\gamma$  plane. A further change occurs from the  $\{225\}_\gamma$  to the  $\{3,10,15\}_\gamma$  plane above 1.4% interstitial content (carbon), this change is accompanied by a change in morphology which is referred to as 'Lenticular' or 'Acicular'. A similar effect is also observed in Fe-Ni alloys (above approximately 28% Ni) where a bcc martensite structure is formed in contrast to the Fe-C alloy which has a bct structure.

Many suggestions have been put forward to explain the change from slipped to twinned martensite. One theory is that twinned martensite is formed just below a critical  $M_s$  temperature of approximately 200°C. (36) This does not appear to apply on the basis that slipped martensite is also formed well below room temperature as in 18/8 stainless steel. Secondly, it has been suggested that alloying elements which lower the austenite stacking fault energy promote the formation of twinned martensite. (30) This is in agreement with the report that nickel lowers the stacking fault energy. (37) (67) There have been, however, some cases in which nickel may raise the stacking fault energy of austenite. (38) (39)

A recent suggestion on the criterion for the transformation

from slipped to twinned martensite is concerned with the driving force required for transformation. According to this proposal transition (21) from lath to twinned martensite occurs at about 1350J/Mole. Above this value transformation is suggested to occur by twinning. The influence of temperature on the martensite transformations has been (40) studied by Zener. He suggested that a critical ordering temperature was necessary for carbon atoms for transition from bcc to bct in Fe-C alloy. This argument cannot be applied to Fe-Ni alloys which have a bcc structure with very little interstitial concentration.

(17)

G. Krauss and A.R. Marder examined the influence of alloy composition and transformation temperature on the transition from lath to twinned martensite. They concluded that alloys which tend to stabilize austenite, e.g., C, N, Ni, Pt and Mn lower the Ms temperature and make possible the transition to the twinned martensite whereas ferrite stabilizers i.e., "loop formers" such as Sn, Cr, W, V and Mo tend to prevent the formation of austenite with a low Ms temperature and hence the transition to twinned martensite.

#### 2.2.5 Epsilon Martensite

Epsilon martensite which has a hexagonal close packed structure is produced either by cooling from austenite or by a pressure induced (41) shear deformation. The structure consists of parallel straight sided bands lying along the  $\{111\}_\gamma$  planes. The orientation relationship between  $\epsilon$  and  $\gamma$  obeys the Kurdjumov-Sachs relationship as follows:-

$$\begin{array}{lll}
 (111)_\gamma & // & (0001)_\epsilon \\
 \langle 110 \rangle_\gamma & // & \langle 1\bar{2}10 \rangle_\epsilon \\
 \langle 112 \rangle_\gamma & // & \langle 10\bar{1}1 \rangle_\epsilon
 \end{array}$$

(0001) plane is the habit plane of epsilon martensite.  $\epsilon$  martensite occurs in Fe-Mn and Fe-Ni-Cr alloys after cooling from austenite. In Fe-Ni-Cr alloys martensite is induced by deformation at room temperature. In Fe-Mn alloys  $\epsilon$  is often associated with bcc  $\alpha$  martensite after subzero deformation. In some cases  $\epsilon$  martensite also occurs with austenite and bcc  $\alpha$  martensite.

It has been suggested that  $\epsilon$  forms from austenite by the formation of Shockley partial extended dislocations on every alternate (111) plane. This could be achieved by a pole mechanism consisting of a single Shockley partial dislocation rotated about a screw dislocation. (42)

## 2.2 Stacking Faults in the FCC Structure

### 2.2.1 Nature of Stacking Faults.

Close-packed metallic structures are often represented as layers of hexagonal nets of atoms stacked one over the other in a regular sequence. The fcc structure is given by the stacking of (111) planes in the sequence ABC ABC and the close packed hexagonal structure by the stacking of (0001) planes in the sequence ABABAB. A stacking fault may be defined as the planar surface of separation between two regions of a crystal which have the same orientation but which do not form a continuous lattice. When such a surface lies parallel to the closest packed planes in a crystal, its energy is the lowest; therefore, in fcc and cph structures, stacking faults are energetically acceptable only when they lie parallel to the (111) or (0001) planes, and can be represented as interruptions in the regular stacking sequence of closed planes.

Considering the fcc lattice, the normal stacking sequence ABC ABC can be changed by faulting to any of the following sequences (43) in the manner shown in the table A.

Table A

Structure	Type	Stacking Sequence	Intrinsic I Extrinsic E	Other Classification
1 fcc	1V	AECAB/AECAB	I	Deformation fault
2 fcc	2V	AECABACAEC	E	Double deform- ation fault
3 fcc+twin		ABCAB/ACBACE/AEC		Growth/Twin fault
4 cph	1V	ABAB/ACAC	I	Growth fault
5 cph	2V	ABABA/C/AEC	I	Deformation fault

An intrinsic fault is where the atomic pattern of the two regions of the crystals extends to the composition plane which may or may not be an atomic plane. In contrast in case 2 the composition plane is an atomic plane and is not continuous with the atomic pattern in the regions of the crystal on either side of it. The extrinsic fault can be considered as two (44) intrinsic faults on adjacent planes. The stacking sequence in case (3) represents a twinned fcc lattice. The twin boundary was referred to as a growth fault. However, considering faults as being either intrinsic or extrinsic, the twinned structure can be regarded as the result of an intrinsic fault, on every successive plane in the sequence. Double deformation or extrinsic faults in fcc, on alternate planes will produce a twin

but deformation does not produce an extrinsic fault in cph. If LV faults occur on every alternate plane in the fcc lattice, then a cph lattice results as in case (4). Thus with a high faulting density, an fcc lattice can show a continuous transition between fcc, twinned fcc and cph structure.

(45)

Toth et al have investigated stacking fault formation in cobalt and shown that deformation faults in the fcc structure are intrinsic. This is in agreement with other workers who have studied stacking faults in Cu-Al, Cu-Ge, Ni-Co and stainless steel.

(46)

Stacking faults are produced by dislocation reactions. A lattice dislocation  $a/2 \langle 011 \rangle$  in the  $(\bar{1}\bar{1}\bar{1})$  planes dissociate as follows:

$$a/2 \langle 011 \rangle = a/6 \langle 112 \rangle + a/6 \langle 121 \rangle$$

The vector termed "Burgers vector" represents a displacement of the type  $a/6 \langle 112 \rangle$ . A partial dislocation with this type of Burgers vector is a glissile Shockley partial dislocation. When the Burgers vector is perpendicular to the planes of the faults, the partial is a sessile Frank partial with Burgers vector of type  $a/3 \langle 111 \rangle$ .

### 2.3.2 The Role of Stacking Faults in Martensitic Transformations.

#### 2.3.2.1 The FCC to CPH Transformation

Transformation from the fcc structure to the cph structure is a special case of martensitic transformation where the parent and product phase are fully coherent. As discussed in the previous section an intrinsic (LV) fault on every alternate  $\{111\}$  plane in an fcc structure would produce a cph structure. The faulting could either be

independent in which case, all the three available  $a/6 \langle 112 \rangle$  type shear vectors would operate and no shape change would result or one particular shear direction could be active in which case, a shape change would be expected. Observations on Co and Co-Ni alloys have revealed a macroscopic shear, suggesting that independent faulting is unlikely. (47) The growth of cph on every alternate  $(111)_\gamma$  planes has been compared with the mechanism proposed for the formation of a mechanical twin by Cottrell-Hilby. (48)

(49)  
Lollman has investigated martensitic transformation in Cobalt and suggested a dynamical mechanism that a stress field is created by the intersection of a fault with another on an intersecting  $\{111\}_\gamma$  plane and to compensate this stress an  $a/6 \langle 112 \rangle$  partial is nucleated on the next plane. He also suggests that a compensating fault runs into another fault on any of the other three  $\{111\}_\gamma$  planes and results in the formation of laths of the cph phase.

(50)  
Venables et al studied the martensite transformation in stainless steel by electron microscopy. The role of cph  $\epsilon$  martensite as an intermediate phase in the sequence  $\gamma_{fcc} \rightarrow \epsilon_{cph} \rightarrow \alpha_{bcc}$  has been widely discussed. They concluded that  $\epsilon$  martensite is produced by faulting in the austenite. In Fe-Mn-C alloys White and Honeycombe suggest from x-ray and replica observation that martensite is nucleated at the stacking faults. (51)  
(52)  
Mishiyama and Shimizu studied martensite formation in low carbon manganese alloys and concluded that  $\epsilon$  martensite is associated with profuse faulting in the austenite. Later Marsh investigated the transformation of fcc to cph in Co-Fe alloys (53)

in detail. He has proposed that nucleation occurs at the intersection of stacking faults and twin boundary interfaces with grain boundaries. Marsh concluded that the rate of nucleation was dependent on grain size, plastic deformation and annealing temperature. He also suggests that fault interfaces may act as obstacles to  $\epsilon$  nucleation if removed from grain boundaries. Growth of  $\epsilon$  is produced by the clustering of partials mutually stabilized by the intersecting of the stress field.

The mechanism of formation of  $\epsilon$  phase produced by deformation in 18/8 stainless steel has been studied recently by Fujita and Ueda.<sup>(54)</sup> It was shown that the  $\epsilon$  phase is formed by an irregular overlapping process in which the stacking faults are formed on  $\{111\}_\gamma$  slip planes in the fcc matrix at first and then further stacking faults are easily induced on  $\{111\}_\gamma$  planes near the original fault planes due to minimizing both the bulk free energy and the total energy of stacking faults. No screw pole mechanism has been observed as suggested by Seeger.<sup>(55)</sup>

#### 2.3.2.2 The GPH to BCC Transformation.

$\epsilon$  martensite is found in association with bcc martensite in a number of highly alloyed steels. This type of  $\alpha$  martensite which appears to be formed in low stacking fault austenite has been extensively studied by X-ray optical and electron microscopy.<sup>(14) (28) (29) (50) (56)</sup>

The close association of  $\alpha$  and  $\epsilon$  phases has provoked much discussion on the question as to whether  $\epsilon$  forms first and  $\alpha$  nucleates within the  $\epsilon$  or the austenite transforms directly to  $\alpha$  with the  $\epsilon$  being formed as a consequence of the large shear strain. The nucleation of  $\alpha$  from  $\epsilon$  has been reported by Cina.<sup>(57)</sup> This observation

is in agreement with the work of Reed who showed by extensive optical and electron microscopy investigations that 18/8 stainless steels transform to both  $\epsilon$  and  $\alpha$  phases on cooling. The  $\alpha$  is formed isothermally and only in small amounts on cooling although considerably large quantities of  $\alpha$  are formed on cold rolling at  $-196^\circ\text{C}$ .  $\epsilon$  phase was believed to be formed by the faulting of every other  $\{111\}_\gamma$  plane. The  $\alpha$  phase is formed as long thin plates lying within the  $\epsilon$  bands. The long axis of the  $\alpha$  phase was parallel to  $\langle 110 \rangle_\gamma$  and the habit plane was  $\{225\}_\gamma$  plane.

(14)

Kelly and Nutting observed no  $\epsilon$  phase in 18/8 stainless steels containing  $\alpha$  martensite on either cooling or deformation at  $-196^\circ\text{C}$ . The  $\alpha$  martensite which they have observed appeared as needles in  $\{111\}$  planes and twin related having Kurdjumov-Sachs orientation relationship.

(50)

Venables observed both the phases on deforming an 18/8 steel at  $-196^\circ\text{C}$ . The  $\alpha$  phase was always found to be in contact with the  $\epsilon$  phase and preferentially nucleated at the intersection of on two sets of  $\{111\}_\gamma$  planes. The habit plane was found to be  $\{225\}_\gamma$  plane and observed orientation relationship were:

$$\begin{array}{l} (111)_\gamma \quad // \quad (0001)_\epsilon \quad // \quad (011)_\alpha \\ \langle 011 \rangle_\gamma \quad // \quad \langle 12\bar{1}0 \rangle_\epsilon \quad // \quad \langle 111 \rangle_\alpha \end{array}$$

(29)

Lagneborg studied the martensitic transformations in two steels of slightly different composition, Steel I contained 18% Cr-7.2%Ni, 1%Mn and 0.45%Si and steel II contained 16.5% Cr - 8.3% Ni, 1% Mn, 1% Si and 0.7% Mo. In both steels  $\alpha$  and  $\epsilon$  phases formed both on cooling and on deformation. The morphology of the phases in both

cases were found to be different. On cooling the martensite had a shape of long plates, the long dimensions of which were in the plane of the  $\epsilon$  discs while the martensite induced by deformation always occurred as needles in contact with discs of  $\epsilon$ . The  $\alpha$  martensite in steel I had  $\langle 110 \rangle_{\gamma}$  long direction on  $(225)_{\gamma}$  habit plane while steel II had  $(259)_{\gamma}$  habit plane. There was a difference in the nature of inhomogeneous deformation as well. Slip took place in steel I on two  $\{110\}_{\gamma}$  planes at  $60^{\circ}$  to one another, while in steel II the imperfections observed were on  $\{112\}_{\alpha}$  planes. Lagneborg also observed that the martensite formed on cooling was partially isothermal. Small amounts of prior deformation stimulated the transformation strongly whilst large amounts decreased the tendency to transformation.

Extensive electron microscopic studies were carried out in  
(28)  
18% Cr- 12%Ni steels by Dash and Otte who found that  $\alpha$  phase contained a high density of dislocations without any stacking faults. The  $\epsilon$  phase which they observed was always heavily faulted and did not contain dislocations. In contrast to the findings of several other investigators, Dash and Otte reported that  $\alpha$  phase could occur independently of  $\epsilon$  while  $\epsilon$  phase always impinge on  $\alpha$  crystals. They also observed that the widths of  $\epsilon$  bands and the density of faults dependent on the size and relative distance between  $\alpha$  crystals. With this observation, Dash and Otte concluded that  $\epsilon$  is not an intermediate phase in the  $\gamma \rightarrow \alpha$  transformation but forms as a consequence of the large strain induced in  $\alpha$  adjacent to  $\epsilon$ .

(59)

Breedis examined the cph to bcc transformation in Fe-Ni-Cr alloys and showed that the amount of  $\epsilon$  associated with  $\alpha$  decreased by replacing chromium with nickel. This was related to the stacking fault energy which increases with nickel content. He has therefore argued that  $\epsilon$  could not occur spontaneously as the stacking fault energy was not zero, thus  $\epsilon$  is formed by the presence of  $\alpha$ .

(60)

Goldman et al have suggested that a different  $M_s$  temperature should be observed for the  $\gamma$  to  $\epsilon$  transformation from that due to the  $\gamma$  to  $\alpha$  or  $\epsilon$  to  $\alpha$  transformation. Since the separate  $M_s$  temperature was not detected, they concluded that  $\epsilon$  was an intermediate phase.

(61)

Schumann however, for the  $\gamma$  to  $\epsilon$  transformation did observe a distinct  $M_s$  temperature. He found in Fe-13.83% Mn alloy that the  $M_s$  temperature for the  $\gamma$  to  $\epsilon$  transformation was about  $160^\circ\text{C}$ , for the  $\epsilon$  to  $\alpha$  transformation was  $140^\circ\text{C}$ . On the other hand he had some difficulty in detecting the  $M_s$  temperature in Fe-11.18% Mn and Fe-12.75% Mn alloys which were mainly  $\alpha$ .

(62) (63)

Manganon and Thomas did not observe either  $\alpha$  or  $\epsilon$  in an 18/8 stainless steel on cooling. Both these phases formed on deformation. The  $\epsilon$  phase which they observed was reported as a faulted phase and its amount depended on the rate of deformation. The amount of  $\epsilon$  reached a maximum at about 5% deformation and decreased after, while the amount of  $\alpha$  increased steadily with increasing deformation.  $\epsilon$  phase was formed independently of  $\alpha$  while the  $\alpha$  phase was preferentially nucleated at the intersection of  $\epsilon$  bands.

(64)

Recently Grunes et al showed that the nucleus of  $\alpha$  in an

Fe-15% Mn alloy occurred preferentially at the intersection of  $\epsilon$  bands and observed a high density of dislocations at the  $\gamma/\epsilon$  and  $\epsilon/\alpha$  interfaces. The orientation relationship they observed are:

$$\begin{array}{l} (111)_\gamma \quad // \quad (001)_\epsilon \quad // \quad (110)_\alpha \\ \langle 110 \rangle_\gamma \quad // \quad \langle 0112 \rangle_\epsilon \quad // \quad \langle 011 \rangle_\alpha \end{array}$$

### 2.3.3 Measurement of Stacking Fault Energy

#### 2.3.3.1 Node Radii Technique:

According to this method stacking fault energy may be determined with a simplified formula as follows: <sup>(65)</sup> (See Fig.7).

$$\gamma_{SF} = \frac{G \cdot b^2}{2R} \dots\dots\dots (1)$$

- $\gamma_{SF}$  - Stacking fault energy
- b - Burger Vector
- R - Radius of curvature
- G - Shear Modulus

This is the only method of direct measurement of stacking fault energy. In the case of low stacking fault energy measurements i.e.,  $< 20 \text{ erg/cm}^2$  the accuracy of values measured is reasonably good, while greater values required some correction. This is due to the effect of neighbouring dislocations on the node. <sup>(65)</sup>

#### 2.3.3.2 Twin Frequency Method:

This may be formulated as follows:- <sup>(66)</sup>

$$v = 0.13 \frac{\gamma_{\epsilon\beta}}{\gamma_{\text{tb}}} \dots\dots\dots (2)$$

Where

$\gamma_{tb}$  - twin boundary energy

$\gamma_{gb}$  - grain boundary energy

$\nu$  - twin frequency

Twin frequency is measured by counting the number of coherent twin boundaries per austenite grain, by averaging a number of grains. The relationship between stacking fault energy and twin boundary is given as follows:-  
(67)

$$\frac{\gamma_{SF}}{\gamma_{tb}} = 1.6 - 2.8 \dots\dots\dots 3 (a)$$

The experimental results indicates that the ratio is less than or greater than 2 depending on whether the stacking fault energy is low or high. With the assumption of  $\frac{\gamma_{SF}}{\gamma_{tb}} = 2$  and substitution, a relationship between stacking fault energy and twin boundary energy can be determined as shown in equation 3(b).  
(67)

$$\gamma_{SF} = 0.26 \frac{\gamma_{gb}}{\nu} \dots\dots\dots 3 (b)$$

#### 2.4 Strength of Martensite

The factors which affect the strength of martensite may be classified as follows:  
(68)

- (a) solid solution hardening by interstitial elements
- (b) solid solution hardening by substitutional elements
- (c) grain size
- (d) strengthening by substructure

##### 2.4.1 Solid Solution Hardening by interstitial elements

Solid solution hardening by carbon is the most favoured strengthening mechanism proposed for martensite. The effect of carbon on the strength of martensite was first developed into a

quantitative theory by Winchell and Cohen. They showed that, providing care was taken to prevent ageing during or after quench, or to correct for this ageing, the strength of martensite varied linearly with the cube root of the carbon content up to 0.4%C. In addition to showing the expected remarkable increase in strength of martensite with carbon content, Winchell and Cohen made two other very important observations. Firstly, ageing of martensite with associated changes in strength occurred at temperatures as low as  $-40^{\circ}\text{C}$ . This means that, if the properties of a martensite where all the carbon is in solution are to be measured, great care must be taken to prevent ageing. The second observation is even more significant. The hardness of the 0.82%C - 16.7% Ni martensite was found to be 685 HV at  $-196^{\circ}\text{C}$ , while 0.02%C - 30.5% Ni martensite was 340 HV at  $-196^{\circ}\text{C}$ . They suggested that the change in strength due to differences in nickel content between 10% and 30% Ni is negligible. The difference between these two hardness values is produced by the addition of carbon. Winchell and Cohen states that the strengthening mechanism is due to the segregation of carbon atoms. The ageing experiments which they carried out on high carbon steels support the view that carbon can also move rapidly in the body centred tetragonal structure, and the effect of this rapid migration of carbon on the mechanical properties of martensite can be quite dramatic.

#### 2.4.2 Solid Solution Hardening by Substitutional elements

Substitutional elements are known to increase the strength of martensite. Substitutional elements such as Nickel can lead to an increase in strength of martensite while chromium is the least

effective solid solution strengthener. However, when Nickel is added to carbon steels, so many other effects such as change in  $M_s$  and in the amount of precipitation during the quench are introduced that it is impossible to isolate the solid solution hardening effect of nickel. Consequently it is suggested that the strengthening effects of elements in substitutional solid solution may be strongly influenced by slight variation in the interstitial contents. It is also suggested that substitutional strengthening may be either the direct effect of dislocation interaction with solute atoms or an indirect effect in which dislocation mobility is changed by the variation of stacking fault energy. (70) The hardening of Copper by substitutional impurities produced by the elastic interactions of solute atoms supports the view of Petch. (70) (71)

#### 2.4.3 Grain Size

The effect of grain size on the yield stress may be formulated as follows:- (70)

$$\sigma_y = \sigma_i + K_y \cdot d^{-\frac{1}{2}} \dots \dots \dots (4)$$

where

- $\sigma_y$  = yield stress
- $\sigma_i$  = lattice friction stress
- $K_y$  = a locking parameter
- $d$  = grain diameter

The effect of grain size on the yield stress is thus dependent upon the locking parameter, which depends on the segregation of interstitial atoms in bcc metals.

In Fe-Ni alloys, Speich and Warlimont have investigated the effect of carbon on the width of martensite laths. They suggested that there was a direct relationship between the size of individual laths in the martensite with the prior austenite grain size and concluded that carbon reduced the lath size in the  $\alpha$  martensite.

#### 2.4.4 Substructure Strengthening

It is suggested that the formation of twins during martensite transformation contributes to the strength of martensite. Further investigations on this twin hardening model predicts that at a given carbon content a twin martensite will be stronger than an untwinned martensite, and not all twinned martensite should be of equal strength.

Padcliffe and Schatz investigated martensite structure changes from laths containing a high density of dislocations at 25% Ni to internally twinned plates at 30% Ni and found no appreciable change in strength. It is therefore argued that, since the dislocation density in internally twinned martensite is relatively low, then if the twins had no effect on the strength, the internally twinned martensite should be weaker than lath martensite. The similarity in the strength of the two structures then leads to the conclusion that the twins provide a strengthening effect which approximately balances the loss in strength due to the decrease in dislocation density.

#### 2.5 Influence of Deformation on the Strengthening of Martensite

Martensitic transformations are strongly promoted by deformation in a range of temperature above  $M_s$ . A limiting temperature is

known as  $M_d$ , above <sup>which</sup>  $\lambda$  no further transformation will occur by deformation.  $A_d$  is a temperature below which the  $A_s$  may not be reduced by further deformation of martensite prior to the reverse transformation.

Martensite in ferrous alloys has an extremely high work hardening rate. Deformation of austenite below the re-crystallization temperature, which is known as ausforming, is an effective method for strengthening martensitic alloys. It is suggested that precipitation of carbides which pin dislocations during deformation, produces a high dislocation density and results in a decrease in  $M_s$  temperature. (74) (75)

A further treatment of strain tempering is applied to ausformed steels to increase the yield stress without loss in ductility.

Zerolling is a method of strengthening for alloys which have a  $M_s$  temperature below room temperature. Deformation of austenite is carried out below the  $M_d$  temperature in order to produce martensite from austenite. This method increases the yield stress with little loss in ductility. In certain alloy steels the formation of martensite during deformation can enhance their strength as well as ductility. (76)

These steels which are called TRIP steels should have  $M_s$  and  $M_d$  lower than room temperature so that austenite is retained when the steel is quenched to room temperature. The quenched steels are then deformed at about  $450^\circ\text{C}$ . The composition of the steels should be such that this deformation raises the  $M_d$  to above room temperature so that when the steels are finally tested during use strain induced martensite is formed to increase the strength and ductility.

A number of investigations have been carried out to explain the influence of phase change produced by deformation on the strengthening of martensite. Yershova et al (77) examined the phase transformation which takes place during heat treatment and deformation in Fe-Mn alloys. The structure of a 0.06% C - 19.7% Mn alloy in the quenched condition contained  $\gamma$  +  $\epsilon$  phases. It was found that the amount of  $\epsilon$  phase existing at various quenching temperatures was independent of quenching rate. This was in contrast to the findings of Parr. White (51) and Honeycombe investigated the work hardening behaviour of a wide range of Fe-Mn-C alloys and observed  $\alpha$  martensite nucleated in  $\epsilon$  martensite during deformation at  $-196^{\circ}\text{C}$ . Yegolev and Begochev (78) studied Fe-Mn alloys containing Molybdenum and Titanium and showed that the formation of  $\epsilon$  martensite, as a result of deformation, decreases with increasing amount of alloying elements at the expense of  $\alpha$  martensite. The effect of cold deformation on the microstructure and mechanical properties of an fcc Fe-Ni-Co-Cr-Mo alloy has been investigated by Mitchels and Forbes Jones. (80) The strength which was achieved by 20% deformation was attributed to an increase in dislocation content. It was shown that greater amounts of deformation resulted in the formation of deformation twins which increase in density. This hardening mechanism is in contrast with that reported to be operating in a similar fcc Co-Ni-Cr-Mo alloy, in which strengthening is attributed to the formation of a deformation induced fine cph  $\epsilon$  phase.

The influence of deformation in Fe-Mn-Co alloys has been recently examined by Stacey. (48) It was shown that considerable increase in the amount of  $\alpha$  martensite is achieved by up to 20% deformation at

room temperature. This was associated with an increase in strength.  
(81)  
The same behaviour was also found in Fe-Mn alloys.

## 2.6 Fe-Mn Alloys

The addition of Manganese to iron results in an increase in  
(82)  
strength. This increase in strength occurs in alloys up to 12%  
Manganese. The formation of  $\epsilon$  martensite, which occurs above 12% Mn,  
(83)  
is associated with a decrease in strength.

It has been shown that the addition of manganese to Fe-C  
alloys improves the impact properties. This is due to the grain refine-  
(84)  
ment of the grain boundary carbide.

(85) (86)

Fe-Mn alloys up to 40% Mn have been investigated in detail.  
In the (4-10)% Mn alloys lath martensite with the (111) habit plane  
forms irrespective of the cooling rate in the range from  $\frac{1}{2}^{\circ}$  C/min to  
4000 $^{\circ}$ C/min. Alloys between 10-15% Mn contain  $\alpha+\epsilon$  with no retained  
austenite, and the maximum  $\epsilon$  contents of 85-90% occurs at 15% Mn. In  
the alloy range 15-28% Mn the matrix structure is  $\gamma+\epsilon$ . Alloys  
containing more than 28% Mn do not transform on cooling to room temper-  
ature and consist entirely of austenite.

The structure produced by continuous cooling in Fe-Mn alloys  
may be explained by the influence of manganese on the kinetics of  
austenite decomposition and on the stacking fault energy of the  
austenite. (81) Manganese is an austenite-stabilizing element which  
lowers the transformation temperature and also retards the rate of  
transformation. Furthermore, manganese also lowers the austenite  
stacking fault energy, (81) and it seems reasonable to assume that the

appearance of  $\epsilon$  martensite, which is essentially composed of stacking faults on every alternate  $(111)_\gamma$  austenite plane, occurs when the austenite stacking fault energy approaches zero i.e., at about 10% Mn. Within the range 0-10% Mn transformation is largely controlled by the effects of manganese on the kinetics of the  $\gamma \rightarrow \alpha$  transformation, and this is illustrated by the changing sequence of massive ferrite, bainite, and martensite as the manganese concentration increases. In alloys containing more than 10% Mn the transformation is influenced by the low stacking fault energy and high driving force required for the  $\gamma \rightarrow \alpha$  transformation.  $\epsilon$  martensite therefore, appears as an intermediate stage in the  $\gamma \rightarrow \alpha$  sequence since its formation requires a smaller driving force. (81)

It has been shown that in Fe-Mn alloys containing more than 10% Mn, two differing morphologies of  $\alpha$ -martensite existed which are also associated with  $\epsilon$  martensite. These structures appear to be either blocky or lenticular in contrast to the normal straight sided lath martensite. The structure in the 4-10% Mn alloys show poor impact properties by intergranular brittle fracture at the prior austenite grain boundaries. (85) The toughness of this material can be improved by tempering above 600°C. However, this is accompanied by decrease in both tensile stress and yield stress. (88) (88) Schumann suggested that on tempering at 600°C, precipitation of plates of austenite may stop the crack propagation, thus resulting in an improvement in impact properties.

(85)  
Bolton has recently studied the various contributions to

the athermal component of flow stress in Fe-Mn alloys. This may be formulated as follows:-

$$\bar{\sigma}_0 = \Delta\bar{\sigma}_\alpha + \Delta\bar{\sigma}_s + \Delta\bar{\sigma}_d \quad (5)$$

where

$\bar{\sigma}_0$  is the athermal component of flow stress

$\Delta\bar{\sigma}_\alpha$  is the athermal contribution due to the flow stress of pure annealed iron.

$\Delta\bar{\sigma}_s$  is the athermal contribution due to solid solution hardening.

$\Delta\bar{\sigma}_d$  is the athermal contribution due to dislocation substructure.

where

$$\Delta\bar{\sigma}_\alpha = 25\%$$

$$\Delta\bar{\sigma}_s = 30\%$$

$$\Delta\bar{\sigma}_d = 45\%$$

For Fe-Ni alloys the contributions have been determined and these were as follows:-  
(87)

$$\Delta\bar{\sigma}_\alpha = 25\%$$

$$\Delta\bar{\sigma}_s = 34\%$$

$$\Delta\bar{\sigma}_d = 41\%$$

(85)

These results did not differ from the findings of Bolton.

## 2.7 Fe-Mn-Co alloys (57)

Cina investigated Fe-Mn-Co alloys and found that the

contribution of cobalt to the strength of the Fe-Mn alloys was higher than either Chromium and Nickel.

(88)  
Schumann observed a great amount of  $\epsilon$  phase in the Fe-Mn alloy with 5% Co. This was in contrast to the suggestion made by Cina regarding the addition of third elements i.e. Co is less effective than Manganese in producing  $\epsilon$  martensite.

The influence of ageing on the Fe-Mn-Co alloys have been investigated by Suzuki. (89) Age hardening was observed at 500-550°C in the ageing process of the decomposition of Fe-Mn-Co martensite structure in the comma-shaped region around the compositional range of 15% Mn (20-50)% Co to 18% Mn 50% Co. He concluded that the hardening occurred due to the internal strain caused by compositional fluctuations or fine dispersions of austenite highly concentrated with solute atoms as in the case of hardening in Fe-Ni-Co or Fe-Ni-Mn alloys. (90)

The structure and properties of Fe-Mn-Co alloys have been examined recently by Stacey. (48) His findings can be summarized as follows:

- (a) The addition of cobalt to Fe-Mn alloys promotes the formation of bcc  $\alpha$  martensite. This is associated with an increase in strength but no improvement in ductility.
- (b) The influence of cobalt on the stacking fault energy depends on the Manganese concentration. There is no obvious correlation between the volume fraction of  $\epsilon$  martensite and the stacking fault energy. Cobalt appears to reduce the amount of  $\epsilon$  in the 12.5% Mn

alloys. This is in contrast to the idea of  
(61)  
Schumann who suggested that Cobalt promotes  
the formation of  $\epsilon$  by lowering the stacking  
fault energy of austenite.

- (c) The addition of cobalt to any alloy with 17.5% Mn increases the strength without loss in ductility. This alloy appears to have a suitable matrix for maraging.
- (d) The orientation relationship between  $\alpha$  lath martensite and austenite is the Kurdjumov-Sachs relationship.
- (e) The amount of  $\alpha$  martensite is increased by deformation. The 17.5% Mn alloy can be strengthened by deformation and ageing without drastic reduction in ductility.

## 2.8 Maraging Steels

Maraging steels are a group of high strength steels characterised by their low carbon contents. The term "Maraging" refers to the development of the final strength by transforming austenite to martensite and subsequent ageing of the martensitic matrix. Although there have been a great number of investigations made on the subject of strengthening mechanism in maraging steels, the exact nature of the hardening precipitates is still in doubt in many alloys. It is now generally accepted however, that the hardening precipitate in the Co/Fe alloy is  $\text{Fe}_3\text{Co}$ , which dissolves on prolonged ageing to form

the  $\text{Fe}_2\text{Mo}$  Laves phase or  $\sqrt{3}$  phase. <sup>(91)</sup> The  $\text{Ni}_3\text{Mo}$  phase, a hexagonal structure which is considered to be partially coherent with the matrix. <sup>(92)</sup> The  $\text{Ni}_3\text{Mo}$  and  $\text{Ni}_3\text{Ti}$  intermediate phases are considered to form because of their partial coherency with the matrix whilst the equilibrium Laves phase would be completely incoherent and hence more difficult to nucleate.

The strength of maraging steels can be readily explained by the observed precipitate distribution although the exact nature of the deformation mechanism is not known. There have been relatively few attempts to explain the reason for the good toughness of maraging steels. A few of the factors which may be responsible for the relatively unique behaviour of maraging steels are discussed below. It is obvious that many of the properties of maraging steels are inherited from the Fe-18% Ni matrix since the deformation behaviour of maraging steels is very similar to those observed by Floreen, <sup>(91)</sup> in a binary alloy of this composition. However, Floreen showed that the particular hardening mechanism is very important since optimum strength and toughness are only obtained if hardening is induced by a combination of Cobalt and Molybdenum. It is therefore important to consider this combination as to whether it is in fact responsible for the high toughness values. <sup>(93)</sup> Floreen showed that various ternary precipitation hardening systems based on Fe-18% Ni, all become brittle at strength levels of 110 tons force/sq.inch. In supporting the contention that the Co and Mo combination is unique, in a subsequent paper by Floreen and Speich <sup>(94)</sup> it was shown that the addition of 2% Mo to Fe-Ni-Co-Ti and Fe-Ni-Co-Al alloys resulted in a marked improvement

in toughness. This addition reduced the degree of precipitation in the grain boundary and it was therefore concluded that the cleanliness of the grain boundaries rather than the hardening mechanism was the important factor controlling toughness. This effect was considered to be similar to the beneficial effect of Molybdenum in suppressing temper embrittlement.

The role of Cobalt in maraging steels is also rather obscure but recently it has been suggested that Cobalt reduces the stacking fault energy of the matrix in addition to its effect on the solubility of Molybdenum. (95) (96) Although cobalt is reported to reduce the solubility of molybdenum in maraging steels, resulting in an increased precipitation hardening effect, (79) (95) (96) Panerjee et al suggest that the hardening effects are directly additive with no synergistic effect. The reduction in stacking fault energy produced by cobalt additions was found to result in a smaller dislocation cell structure after cold deformation of Fe-Ni-Co martensite. It is unlikely however, that such a cell structure would improve the toughness of maraging-type alloys since Floreen (97) showed that slip in the Fe-18% Ni alloy was largely unaffected by the sub-boundaries present in this structure. It might also be expected that a reduction in stacking fault energy inhibit cross slip, resulting in an increase in the localised slip on restricted slip systems, which Floreen observed in the binary Fe-Ni alloy. Such a restriction of slip is usually considered to increase the stress concentration at the head of dislocation pile ups and increases the tendency for brittle failure. (95) (96) Panerjee et al also

observed that cobalt additions increased the tendency for twinning to occur at low temperatures, which tend to increase the brittle failure. The reduced stacking fault energy produced by cobalt additions was shown to reduce the tendency to form sub-boundaries, the density of dislocations within the matrix being increased. This was thought to increase the number of nucleation sites for precipitates, producing a finer, more uniform distribution, which is considered beneficial to the toughness of the alloy. It would appear however, that the cobalt addition to maraging alloys is unlikely to be responsible for their good toughness, and in fact may be detrimental in this respect.

(98)

Conrad has determined the flow stress of maraging alloys in terms of athermal component, which is sensitive to temperature and strain rate and an athermal component which is proportional to the shear modulus and varies with temperature. The thermal component may be significant in controlling the impact transition behaviour of maraging steels since an increase in the thermal component may be expected to result in brittle behaviour at lower temperatures. Conrad concluded that <sup>the</sup> strengthening mechanism in maraging steels was athermal in nature and arose from the presence of the precipitate particles but, it is difficult to see why other types of precipitate should not have a similar effect.

(91)

Floreen considers that the  $\text{Ni}_3\text{Mo}$  particles may have a special significance, however, since other precipitates result in a reduced toughness. He has noted that the  $\text{Ni}_3\text{Mo}$  precipitate is metastable and proposed that the metastability may result in local enrichment of the

matrix in nickel, as a result of precipitate dissolution. It is suggested that this may allow austenite to nucleate on the precipitates, the austenite then preventing void formation and thus delaying ductile failure. This proposal may be responsible for the observed combination of properties in 18% Ni-Co-Mo steels, and would explain to some extent the critical nature of the composition since lower nickel contents would retard austenite formation during ageing. However, it is possible to argue that all precipitates are metastable since the normal coarsening of precipitates is continually in progress and involves a continual solution of finer precipitates with the solute being re-precipitate on coarser particles. Thus it could be argued that austenite formation on existing precipitates is as likely to occur with other types of precipitates as it is with Ni<sub>3</sub>Mo; with precipitates having a fcc lattice.

Another important factor governing the strength and toughness of maraging steels is their fine grain size. This aspect has received relatively little attention by most authors but could be considered of vital importance in more conventional steels. The only reference relating to the effect of grain size which is known to the author, is that of Detert. (92) He examined 15% Ni maraging steel and showed that remarkable strength and ductility appeared after annealing temperatures up to 1100°C, but a further increase in annealing temperature to 1100°C increased the notch sensitivity to such an extent that tensile specimens broke at the fillet. Again it can be argued that grain size control is not the most important aspect controlling the ductility of those steels since Detert obtained a yield strength of 145 tons force/sq.inch

in his alloy, combined with a reduction in area of 21.5% although the grain size has 20-40 $\mu$ . These properties were obtained after solution annealing at 1000 $^{\circ}$ C and it is probable that a more conventional annealing temperature would further improve the ductility.

### 2.8.1 Manganese Maraging alloys:

It is known that the Fe-Ni and the Fe-Mn alloy systems have similar equilibrium diagrams and show similar phase transformation behaviours. Consequently, manganese has often been substituted for nickel in maraging steels. Patterson et al have shown that substitution of manganese for nickel does not markedly affect the mechanical properties of the 18% Ni maraging steels. In some cases they have reported that the properties achieved by the addition of 2% Mn to a 12% Ni maraging steels were superior than 18% Ni maraging steel. A number of workers have found brittleness in the presence of large quantities of manganese in Fe-Mn alloys. Therefore, partial replacement has been attempted. Patterson et al suggests that when nickel is partially replaced by manganese, Fe<sub>2</sub>CoMo ordering reaction is suppressed by a Mn-Ti or Mn-Co. Goldman and Nance showed that the intensive hardening in Fe-Mn-Ni-Ti is due to both the ordering and precipitation reaction. They also suggested the presence of manganese in the equilibrium precipitate (Fe-Ni-Mn)<sub>2</sub>Ti where nickel and manganese atoms substitute for Fe atoms in the precipitate Fe<sub>2</sub>Ti.

### 2.8.2 Austenite Reversion

The formation of austenite during the ageing of maraging steels has recently received a great deal of attention. Austenite

(101)  
is responsible for softening at long ageing times. It is  
also associated with a change in electrical conductivity, fatigue  
(102)  
properties and stress corrosion cracking.

When the martensite is reheated, one of two things may  
happen. If the alloy is brought to a temperature below  $A_s$  temper-  
ature (i.e. the start of the  $\alpha \rightarrow \gamma$  transformation), the martensite  
will decompose into the equilibrium austenite and ferrite  
(103)  
compositions. The rate of this reversion reaction depends upon  
the temperature. For maraging steels the reversion is at the  
temperature of order of  $485^\circ\text{C}$  and is slow enough for considerable  
precipitation hardening to be achieved before the reversion reaction  
predominates. If on the other hand the alloy is heated above the  
 $A_s$  temperature the martensite transforms by a shear reaction back  
to an austenite of the same composition. In practice, it is quite  
often found, even with relatively fast heating rates, that some  
reversion occurs during heating, which influences the subsequent  
shear reaction.

(104)  
In Fe-Ni alloys, Allen and Barly have suggested that after  
heating austenite is formed by the following diffusion controlled  
decomposition reaction:



where

- $\alpha_2$  = martensite
- $\alpha'$  = low nickel bcc martensite
- $\gamma'$  = nickel enriched fcc phase or reverted austenite.

This is in contrast to the transformation which occurs on heating above A<sub>s</sub> temperature. Austenite of the same composition as the original martensite is formed by an instantaneous reaction which involves shear.

The effect of variation of Ni, Co, Mo and Ti alloying elements on the austenite reversion in Fe-Ni alloys has been studied (105) by Peters. His findings were as follows:-

- (a) increasing nickel content (11%→30%) and cobalt (8%→20%) accelerate the rate of austenite reversion.
- (b) increasing the titanium content reduces the amount of austenite present because titanium reacts with nickel in the matrix to form Ni<sub>3</sub>Ti thus reducing the overall nickel content of matrix.
- (c) Molybdenum increases the tendency for austenite formation. This suggests that much of the precipitate present during austenite formation is an Fe-Mo compound which enriches the matrix in nickel.

Austenite reversion is generally initiated at the martensite lath boundaries and continues until the whole lath is consumed. Austenite reversion during ageing improves the toughness of the alloy in contrast to the effect of precipitation on lath boundaries which would be expected to cause the embrittlement and decrease in strength. (106)

(105) (107)

Peters and Hall have studied the austenite reversion in nickel maraging steels. They have shown an increase in the total volume of austenite during the early stages of the austenite reversion reaction in the presence of retained austenite. This effect has been attributed to the ease of austenite nucleation because of micro-segregation effects in the martensitic matrix, and also the rapid growth of the retained austenite as there is no nucleation problem. (106)

The effect of molybdenum on the ageing kinetics of maraging steels (Fe-Ni-Co-Ni - small amount of Ti and Al) has been examined recently by Naum Dui and Dabosi. (108) They suggested that the increase of super saturation of the matrix in molybdenum is associated with an increase in the rate of precipitation and the tendency toward austenite reversion.

## 2.9 Brittleness in Manganese Steels

Manganese with the presence of carbon in high manganese steels improves the impact properties. On the contrary, in very low carbon manganese alloys, embrittlement is associated with manganese and this tends to be intergranular. (82)

(109)

Hadfield first reported intergranular brittleness in Fe-Mn alloys and found that the brittleness was due to the grain boundary carbide formation. Later the brittleness was attributed to the formation of  $\alpha$  phase from  $\epsilon$  phase. (110) It also has been suggested that the occurrence of embrittlement is due to the twinned martensite structure. (111) A recent investigation contradicts both of these suggestions. (85)

(85)

Bolton has found the mode of brittle fracture to be intergranular. He also pointed out that the embrittlement may be the result of the presence of silicon and concluded that alloys with lower Mn:Si ratio were more brittle than alloys with higher Mn:Si ratio i.e., increasing the silicon content increases the brittleness.

Although the phenomenon of embrittlement of maraging steels is related to that of temper brittleness which generally occurs in low carbon steels, the cause of embrittlement is not evident. Temper brittleness is usually associated with the segregation of As, Sb, P and Sn to austenite grain boundary sites in fcc lattice structure. (112) Embrittlement may also be due to manganese segregation to austenite grain boundaries. Such segregation may decrease the surface energy of iron to promote an intergranular crack.

There are many possibilities regarding embrittlement. It has been suggested recently that the removal of brittleness may be achieved by austenite reversion at high temperatures. (85)

(112)

Capus et al have suggested that molybdenum improves impact properties by its effect on the segregation of impurities at the prior austenite boundaries since its segregation tendency is much higher than chromium and manganese. They also suggest that molybdenum segregation at the prior austenite boundaries could take place during solidification and that molybdenum remains there during heat treatment. Molybdenum atoms at the grain boundaries attract impurity atoms resulting in the formation of molybdenum impurity complexes. This may prevent embrittlement by 'tying-up' the impurity atoms.

### 3. Experimental Procedure

#### 3.1. Alloy Preparation

Initial work concentrated on the examination of Fe-Mn-Co and Fe-Mn-Co-Mo alloys which had matrix structures of either  $\alpha' + \epsilon$  or  $\alpha + \epsilon + \delta$

The alloys used in the present investigation were vacuum melted and cast into 25lb ingots 2 inch square. The ingots were hot rolled to  $\frac{1}{2}$  inch diameter bar from a soaking temperature of 1100°C. The compositions of the alloys used in this investigation are given in Table 1. Niobium was added to the alloys as a grain refining element in an attempt to offset the brittleness found previously in some of the base alloys.

#### 3.2. Specimen Preparation

All the samples used for investigation were austenitized at 1000°C for half an hour in a vacuum furnace, quenched into water and liquid Nitrogen and subsequently aged in salt baths at the selected temperatures. The temperature of the salt bath was controlled to within  $\pm 5^\circ\text{C}$ . In view of the loss of manganese from the sample (although the vacuum furnace was carefully controlled), it was important that the structures examined during the investigation were representative of the bulk material, rather than the surface denuded zone. To ensure that this was the case, a certain layer was removed from the sample surface by polishing on a 300 grade wet silicon carbide paper. It was also important that the martensite observed was produced solely by the deformation process, and not by the

polishing process. In order to remove the effect which is due to the polishing, the specimens were polished on a range of wet silicon carbide papers to a 600 grade and then on a 1 micron diamond wheel. The samples were then etched and repolished on 6 and 1 micron diamond wheels to produce a deformation free surface. Although special care was taken during mechanical preparation, it was difficult to produce a deformation free surface for examination. Therefore an electrolytic polishing technique was used as the final stage before etching. The samples were electropolished for 3-5 seconds using a setting of 2 volt and 0.18 amp supply in an  $A_2$ -disapol solution.

The influence of plastic deformation on the austenite to martensite transformation was studied on samples which had been cold worked by rotary swaging. Twelve cm lengths of material from all the quenched alloys were deformed to diameter reductions of approximately 6%, 12%, 18% and 24% compared with the original starting bar reductions. The reductions were carried out at room temperature and also at  $-196^{\circ}C$  (liquid Nitrogen temperature). In order to reduce the effects of isothermal martensite formation, because cold deformation may increase the  $M_s$  of the alloy to some value  $M_d$ , the rods were cooled at frequent intervals in a bath of water held at room temperature. At the intervals during deformation at  $-196^{\circ}C$  the reduced samples were kept in liquid nitrogen approximately 20 minutes before further deformation.

A stain etching technique was found to be the most successful

method of examining the microstructure of all the alloys used in this investigation. The stain etching technique used in the present work was initially used by Schumann. (88) In this investigation a supersaturated solution of 70% Sodium Thiosulphate and 30% Sodium Metabisulphite was chosen after months of experimentation. This etch showed the  $\alpha$  martensite blue,  $\beta$  martensite a straw colour and the austenite brown. (Figures 86, 101, 102 and 103). Although this etchant was useful for alloys K5, K6 and K7, the best etching technique for alloys K2, K3 and K4 was found to be a double treatment in 70% Sodium Thiosulphate + 30% Sodium Metabisulphite after an initial etch in 6% Nital (Figures 84 and 89).

### 3.3 Thin Foil Preparation

Thin foils for electron microscopy were prepared by the electrojet technique using a Polaron unit. Discs of approximately 0.38 mm thickness were cut from 3mm diameter rods in a Polaron lathe using a fine carborundum cut off wheel. The discs were ground on fine emery paper to flat and parallel surfaces. Thin foils were made from the discs in two stages. They were first dished on either side in a jet of 25% Perchloric acid in Methanol at 18 volts. This dishing produced a double concave shaped disc of bright surface finish. The dishing time was about 9 seconds (one side 5 seconds, other 4 seconds) for a 0.12mm thick disc. The dished discs were electropolished in 5% Perchloric acid and 95% Methanol until perforation occurs. The perforated discs were removed from the electrolyte and washed thoroughly in water and Methanol. Thin foils were always examined in the electron

microscope immediately after perforation because of the rapid deterioration in the foil even when stored in methanol. Jan 6A5, Jan 100 B and Philips EM 300,100 KV electron microscopes were used for thin foil examination. Examination of all the thin foils was very tedious because every area of the specimen which was observed could only be photographed after the electron microscope had been realigned to compensate for the magnetic effects of the specimen.

#### 3.4 Dilatometry

Specimens 20mm in length 3mm in diameter were used to determine the transformation temperatures. Transformation studies were carried out on a Linseis dilatometer with water and argon quenching attachment. The martensite transformation temperatures ( $M_s$ ) were measured by the change in the length which is transmitted to a high speed chart recorder. Different cooling rates (varying from  $50^{\circ}$  -  $1400^{\circ}$ C/min) were used to measure the  $M_s$  temperature. Quenching was carried out after 20 minutes austenitizing at  $1000^{\circ}$ C. The dilatometer consists of a 4mm inside diameter silica tube into which the specimen is fed through a window ground into the bottom. (Figure 8). The specimen length change is transmitted with a silica push rod to a Philips type (FR6010/01) transducer mounted at the top of the silica tube, and its output is then fed into a Philips type (FR6300) phase bridge to record a millivolt output on the X-axis of a Philips type (FR2220/00) X-Y recorder. The specimen temperature is simultaneously recorded on the Y axis of the X-Y recorder from a platinum/platinum 10% rhodium thermocouple, which is fixed into a small hole drilled along the centre line of the

cylindrical specimen. Surrounding the dilatometer tube is an outer sealed silica tube which allows an argon atmosphere to be maintained around the specimen and the argon is fed in from the top of the dilatometer to pass down over the specimen. A range of cooling rates is possible:

- (a) by adjusting the position of the furnace
- (b) by altering the rate of argon flow through the dilatometer
- (c) by electronically programming the heat input into the furnace windings.

### 3.3 X-ray diffraction

Electropolished specimens were examined by a Philips diffractometer using  $\text{Co K}\alpha$ ,  $\text{Ni K}\alpha$  and  $\text{Cu K}\alpha$  as radiation sources. In those alloys showing no preferred orientation, the determination of the volume percentages of the  $\epsilon$ ,  $\gamma$  and  $\alpha$  phases was made by comparing the integrated intensities of the  $(10.1)_\epsilon$ ,  $(200)_\gamma$  and  $(200)_\alpha$  peaks. The integrated intensities of the above reflections obtained using  $\text{Co K}\alpha$  radiation, were compared with the random intensity value obtained from International Tables using the formula:

$$R = \left( \frac{1}{V^2} \right) |F|^2 P \left( \frac{1 + \cos^2 2\theta}{\sin^2 \theta \cos \theta} \right) \left( e^{-2M} \right) \dots (7)$$

where

$R_{hkl}$  = a Factor depends on  $\theta$ , the reflecting set of planes and crystal structure.

$V$  = Volume of unit cell

$F$  = Structure factor

$\theta$  = Bragg angle

$e^{-2m}$  = temperature factor

$p$  = multiplicity factor

For calculation of the volume fraction of two phases the equation then becomes:

$$I_{hkl\alpha} / I_{hkl\gamma} = R_{hkl\alpha} \cdot c_{\alpha} / R_{hkl\gamma} \cdot c_{\gamma} \dots\dots\dots (8)$$

where

$I_{hkl\alpha}$  = Measured integrated intensity of  $\alpha$

$I_{hkl\gamma}$  = Measured integrated intensity of  $\gamma$

$c_{\alpha}$  = Volume fraction of  $\alpha$

$c_{\gamma}$  = Volume fraction of  $\gamma$

$c_{\alpha}$  may be calculated as a percentage of the total phases.

$$c_{\alpha} = \frac{I_{hkl\alpha} / R_{hkl\alpha}}{I_{hkl\alpha} / R_{hkl\alpha} + I_{hkl\gamma} / R_{hkl\gamma}} \dots\dots\dots (9)$$

$c_{\alpha}$  and  $c_{\gamma}$  are valid for a random orientation. In alloys where preferred orientation was evident, as large a number of peaks was examined as possible to improve the accuracy of the phase determination.

$$C_{\alpha} = \frac{\frac{1}{n\alpha} \sum_0^{n\alpha} (I_{\alpha}/R_{\alpha})}{\frac{1}{n\alpha} \sum_0^{n\alpha} (I_{\alpha}/R_{\alpha}) + \frac{1}{n\gamma} \sum_0^{n\gamma} (I_{\gamma}/R_{\gamma})} \quad (10)$$

where  $n$  = no of reflections used.

This equation can be applied in the case of three phases such as  
 $\alpha$ ,  $\epsilon$  and  $\gamma$

$$C_{\alpha} = \frac{\frac{1}{n\alpha} \sum_0^{n\alpha} (I_{\alpha}/R_{\alpha})}{\frac{1}{n\alpha} \sum_0^{n\alpha} (I_{\alpha}/R_{\alpha}) + \frac{1}{n\gamma} \sum_0^{n\gamma} (I_{\gamma}/R_{\gamma}) + \frac{1}{n\epsilon} \sum_0^{n\epsilon} (I_{\epsilon}/R_{\epsilon})} \quad (11)$$

Values for  $I_{\alpha}$ ,  $I_{\gamma}$ ,  $I_{\epsilon}$  were determined by using a planimeter and also counting the squares under the area of the peaks used for determination. Measurements made by the planimeter agreed reasonably well with the measurements made by counting squares.

### 3.6 Tensile Testing

Tensile tests were carried out on a 5000 kg capacity Instron tensile testing machine, using standard 10 mm cross section Hounsfield tensile test pieces. (See Figure 142). It was not possible to measure a yield stress directly since no distinct yield point occurred. Determination of yield stress was made from the stress strain curve at the 0.2% strain level.

### 3.7 Impact Testing

A Hounsfield balanced impact testing machine was used to determine the impact properties. Subzero temperatures from 0°C,

-100°C and -196°C were achieved by using ice, solid CO<sub>2</sub>, isopentane + liquid nitrogen and liquid nitrogen. For temperature above room temperature a thermostatically controlled, electrically heated oil bath was used. The time delay in transferring the test piece from the heat treatment medium to the test machine was short enough to avoid any serious temperature variation.

### 3.8 Hardness Testing

Specimens used for X-ray diffraction and optical microscopy were subjected to a hardness test by averaging the results of four Vickers hardness impressions from a Vickers hardness machine with a load of 30 kg.

## 4. Experimental Results.

### 4.1 Dilatometric Analysis

The transformation temperatures ( $M_s$ ) produced on cooling to room temperature, are shown in Table 2. The temperature for the start of the  $\gamma \rightarrow \alpha'$  transformation was only slightly affected by a variation in cooling rate varying from 50° - 1400°C/min. The addition of molybdenum showed a considerable effect on the  $\gamma \rightarrow \alpha'$  transformation start temperature. It was found that an addition of 4.85% molybdenum increased the  $M_s$  temperature about 90° C over above alloy K2. The  $M_s$  temperature of the alloys is also decreased with increasing the amount of manganese.

(For examples: Alloy K4 with 4.85% Mo, 13% Mn- $M_s$  = 200°C )

( Alloy K7 with 4.85% Mo, 17% Mn- $M_s$  = 105°C )

In the present investigation it was not possible to observe a separate  $M_s$  temperature for the  $\gamma \rightarrow \epsilon$  and  $\epsilon \rightarrow \alpha'$  transformations. This

is due to the fact that the contraction resulting from  $\gamma \rightarrow \epsilon$  transformation is compensated by the expansion produced by  $\epsilon \rightarrow \alpha'$  transformation.

The martensitic structure formed by rapid cooling reverts, when heated, to austenite by a reverse shear or a nucleation and growth process (diffusional). The shear transformation begins at some critical temperature;  $A_s$ . This value was determined on specimens that had been previously water quenched to form martensite, by heating at varying rates. The results are shown in Table 2. Molybdenum rather surprisingly did not appear to affect the  $A_s$  temperature of the alloys (table 2). Table 2 also shows that  $A_s$  temperatures of the alloys are not also affected by a variation in heating rates.  $A_s$  temperature is also decreased with increasing the amount of manganese, i.e. alloy K4 with 4.85% Mo  $A_s$ -650°C

alloy K7 with 4.85% Mo  $A_s$ -600°C

Examination of the information presented in table 2 shows that  $T_0$  increases with the increase in molybdenum content.  $T_0$ , ( $T_0 = \frac{1}{2} (M_s + A_s)$ ) refers to the temperatures for thermodynamic equilibrium between austenite and martensite. It is suggested that alloying elements which increase the  $T_0$  retard the reversion to austenite. In the present investigation molybdenum in contrast to the findings of Yeo, enhances the reversion to austenite (see Figure 66). It was expected that the reverse transformation on heating would go through the bcc  $\rightarrow$  cph  $\rightarrow$  fcc sequence but no indication of this sequence was evident from the dilatation trace.

#### 4.2 Matrix Composition after Quenching

The  $\gamma$ ,  $\epsilon$  and  $\alpha'$  phases were easily distinguished during optical examination after stain etching with 70% Sodium Thiosulphate + 30% Sodium Metabisulphite. Figures 12, 13 and 14 shows  $\alpha'$  martensite (dark), in the  $\epsilon$  martensite bands (white) and austenite (grey) :-

Alloy K7 showed the largest austenite grain size although all the alloys were quenched from the same austenitizing temperature (1000°C) after solution treatment for half an hour. Comparing Figures 12, 13 and 14, it is evident that molybdenum is responsible for an increase in the prior austenite grain size. The influence of manganese on the grain size is also important. The austenite grain size decreases with an increase in the amount of manganese. (115)

However, it is not possible to compare the grain size of the alloys (K5→K7) with alloys (K2→K4) since no satisfactory microstructures of alloys (K2→K4) in the quenched condition were obtained by stain etching to present in the thesis. Further investigations are still being carried out and the results can be seen in the paper to be published. (115)

Table I summarises the relationship between alloy composition and the volume fraction of the  $\gamma$ ,  $\epsilon$  and  $\alpha'$  phases present in all the as quenched alloys. The amount of retained austenite in the water quenched alloys (K2→K4) is small when compared with alloys (K5→K7). It would appear that the amount of  $\gamma$  is directly related to the manganese content of these alloys.

It is known that manganese is an austenite stabilizing

element which lowers the  $M_s$  temperature of the alloys. Thus, increasing the Mn content suppresses to a great amount the transition from  $\gamma$  to  $\epsilon$  or  $\gamma$  to  $\alpha'$  and results in austenite remaining in the matrix on cooling from austenite phase field to room temperature. Molybdenum also appears to play a direct role in the transformations. In contrast to the effect of manganese on transformation, molybdenum promotes the  $\gamma \rightarrow \alpha'$  transformation in the  $\sim 13\%$  Mn alloys (K2  $\rightarrow$  K4) by raising the  $M_s$  temperature. Table 1 shows that the 17% Mn alloys (K5 and K7) in the water quenched condition contain approximately the same amount of  $\alpha$  martensite. The amount of  $\epsilon$  phase in alloy K7 is lower than in alloys K5 and K6. This effect appears to be contrary to the effect of molybdenum observed in the 13% Mn alloys (K2  $\rightarrow$  K4).

The  $\gamma \rightarrow \epsilon \rightarrow \alpha'$  transformations are effected by subzero quenching. The percentages of the phases after subzero cooling are shown in Table 1. Although subzero cooling did not significantly affect the volume fraction of the phases present in alloys K2  $\rightarrow$  K4, it was possible to partially transform austenite to martensite ( $\epsilon$  or  $\alpha'$ ) in alloys K5  $\rightarrow$  K7 (Table I).

#### 4.3 Martensite Transformations

The kinetics of the  $\gamma \rightarrow \epsilon$ ,  $\epsilon \rightarrow \alpha'$  and  $\gamma \rightarrow \alpha'$  martensite transformations were affected by composition and deformation. The addition of molybdenum was found to encourage the  $\gamma \rightarrow \alpha'$  transformation in the  $\sim 13\%$  Mn alloys while manganese tends to favour the  $\gamma \rightarrow \epsilon$  transformation. (Compare alloys K4 - K7, and K3 - K6 in Figures 87  $\rightarrow$  94). In alloys

K5 → K7 the  $\gamma \rightarrow \epsilon$  transformation was further promoted by small amounts of deformation (Figures 89 → 92). Further amounts of deformation favoured the  $\epsilon \rightarrow \alpha'$  transformation. (Figures 91 and 92). The  $\epsilon$  phase is formed intensively in the early stages of cold deformation (up to 6 per cent). (Figures 88 and 89). The maximum amount of  $\epsilon$  phase (78 per cent) is obtained in alloy K5 in the quenched and deformed (at room temperature) condition. (Figure 89). In the quenched (to  $-196^\circ\text{C}$ ) and deformed condition a maximum of 84 per cent  $\epsilon$  is reached after 12 per cent deformation. (Figure 90). It appears from Figures 89 and 90 that 100 per cent  $\epsilon$  phase cannot be formed in these alloys in any condition. In alloys K2 → K4 the  $\epsilon \rightarrow \alpha'$  transformation takes place in the early stages of deformation (Figures 87 and 88). The effect of deformation on the  $\epsilon \rightarrow \alpha'$  transformation is discussed in detail in the sections 4.4.1 and 4.4.2.

It can be seen from Figures 88 and 90 that increasing amounts of molybdenum in the 17% Mn alloys decrease the stability of austenite during cold deformation. The  $\gamma \rightarrow \alpha'$  transformation is favoured more than the  $\gamma \rightarrow \epsilon$  transformation. Consequently it is suggested that the increase in molybdenum content appears to reduce the critical stage of deformation at which an  $\alpha'$  phase begins to be formed. Cold deformation and phase transformation lead to considerable distortion of the crystal structure, which generally stabilizes the untransformed austenite.

The  $\epsilon$  phase can be described either as regularly faulted austenite or as a cph phase with an ideal c/a ratio. The occurrence of  $\epsilon$  reflections at all predicted ideal cph positions and no change

in austenite reflections suggest the idea that  $\epsilon$  occurs as a cph phase rather than as faulted austenite. (Figures 16 and 17).

Examination of dark field micrographs and selected area diffraction patterns confirmed that  $\epsilon$  phase is a hexagonal phase. (Figure 17). The indexed hexagonal pattern revealed the (00.1) double diffraction spot. This can only arise from a cph structure and this also confirms the existence of the hexagonal  $\epsilon$  phase. The  $(110)_{\alpha}$ ,  $(00.2)_{\epsilon}$  and  $(111)_{\gamma}$  spots overlap due to their very similar atomic interplanar spacing ( $d$ ) (Figure 17 and table 6).

$\epsilon$  plates appear as long - straight sided bands which intersect each other inside the austenite grains. (Figures 60, 71, 77, 82 and 106). In most regions where  $\epsilon$  martensite is observed in the austenite matrix between the  $\epsilon$  martensite it is tightly filled with stacking faults growing from one  $\epsilon$  plate to another (Figures 24, 57 and 77). The stacking faults are oriented at a definite angle to the plane and are parallel to one another. (Figure 57) The overlapping of stacking faults and/or  $\epsilon$  bands can also be seen in Figures 24, 57 and 106. The streaks in Figure 50 in the  $\langle 111 \rangle_{\gamma}$  direction indicate that  $\epsilon$  forms as thin sheets on  $(111)_{\gamma}$  planes. These sheets are perpendicular to the plane of the foil. The streaked pattern in Figure 50 is due to the faulted austenite and/or thin  $\epsilon$  plates. The faulted particles which were identified as a  $\chi$ -phase precipitate (Appendix 4) (115) (116) have been previously reported in Fe-Mn-Co alloys. The nucleation of this type of precipitate and its influence on the properties was examined and will be discussed in detail in the Section 4.5.1.

The  $\alpha$  martensite was observed to be associated with the  $\epsilon$  martensite at the intersection of  $\epsilon$  bands (Figure 106). In all the cases examined  $\alpha$  martensite laths were always associated with one or more  $\epsilon$  bands. The amounts of  $\epsilon$  phase also appeared to increase by small amounts of deformation (Figures 89 and 90).  $\alpha$  martensite was also observed in the  $\epsilon$  bands with no indication of intersection of  $\epsilon$ . In this case the  $\epsilon$  bands were lying parallel to each other from one  $\alpha'$  region to another  $\alpha'$  region (Figure 82). There is no continuation of the  $\epsilon$  bands into the  $\alpha'$  crystal which has grown across the austenite crystal. The existence of such  $\alpha'$  martensite crystals in a given  $\epsilon$  band suggests that  $\alpha$  martensite can nucleate independently of the  $\epsilon$  phase. This will be discussed in detail in the discussion section.

The lath martensite ( $\alpha'$  or  $\epsilon$ ) observed in the present investigation was straight sided laths and these laths have different morphologies from the laths seen in other alloys. Figure 105 shows typical lath structure formed by quenching and 16 per cent deformation at  $-190^{\circ}\text{C}$ . Each lath appears to be made up of blocks of  $\alpha$  martensite. This occurrence is due to a misorientation along the lath boundaries as suggested by Holden et al. (81) Figures 15, 16 and 19 also shows typical lath martensite structure. In figure 16  $\alpha'_1 \rightarrow \alpha'_7$  are twin related regions. Figure 19 shows typical twin related  $\alpha'$  martensite laths lying parallel in the  $\epsilon$  martensite.

In recent years there has been a great deal of interest as to whether the twins observed in Fe-Mn base alloys are transformation twins or deformation twins. The twin related regions observed in many

laths varied in width from 0.8  $\mu\text{m}$  to 1.4  $\mu\text{m}$ . The significance of these measurements will be discussed in detail in the section devoted to the formation of twins in lath martensite. (Section 5.)

#### 4.3.1 Habit Plane Determination

Trace directions of single laths of martensite were determined from electron micrographs and their corresponding electron diffraction patterns using the method described by Kelly. (31) Martensite was observed to occur with a  $(\bar{1}\bar{1}2)_\gamma$  habit plane for alloys K3 and K7 (Figures 149 and 150). The habit plane of  $\alpha$  martensite appears to be independent of the transformation sequence whether it is  $\gamma \rightarrow \alpha'$  or  $\gamma \rightarrow \epsilon \rightarrow \alpha'$ . Because statistically  $\alpha$  does form via the  $\epsilon$  phase, some of these regions must have been included in the trace analysis. Similar results for Fe-Mn-Co alloys have been reported previously by Stacey. (43) In low stacking fault energy alloys i.e. 18/8 stainless steels, the habit plane of twin related  $\alpha$  martensite laths is also reported to be  $(\bar{1}\bar{1}2)_\gamma$ .

#### 4.3.2 Orientation Relationship between $\gamma$ , $\epsilon$ and $\alpha'$

The Kurdjumov-Sachs (K/S) and Nishiyama-Wasserman (N/W) relationships are well known orientation relationships between the fcc, bcc and oph phases during the martensitic transformations.

The electron diffraction patterns from the  $\epsilon$  bands containing  $\alpha$  martensite were complicated, since the reflections from all three phases  $\gamma$ ,  $\epsilon$  and  $\alpha'$  were generally present. By using the simple dark field technique of selecting a diffracted beam as an imaging beam, it was possible to determine which phase gave rise to a particular

spot on the composite pattern. From these composite electron diffraction patterns the orientation relationship between  $\gamma$ ,  $\epsilon$  and  $\alpha'$  phases has been determined to within  $\pm 2$  deg. (Figure 17). The analysis has produced the orientation relationship close to:

$$\begin{aligned} (111)_\gamma & // (0001)_\epsilon // (011)_{\alpha'} \\ \langle \bar{1}\bar{1}0 \rangle_\gamma & // \langle \bar{1}\bar{2}10 \rangle_\epsilon // \langle \bar{1}\bar{1}1 \rangle_{\alpha'} \end{aligned}$$

which is the Kurdjumov-Sachs orientation relationship. The K/S orientation relationship between  $\gamma$  and  $\alpha'$  was chosen rather than the N/W relationship:

$$\begin{aligned} (111)_\gamma & // (011)_{\alpha'} \\ \langle \bar{2}11 \rangle_\gamma & // \langle 110 \rangle_{\alpha'} \end{aligned}$$

which can be obtained from the K/S relationship by a rotation of 5.2 degrees about the  $(111)_\gamma$  axis. However, the N/W orientation relationship between the  $\gamma$  and  $\alpha'$  was also found in some regions (Figure 138). This shows two bcc, one fcc matrix and precipitate zone. The bcc pattern has the zone axis  $\langle 100 \rangle_{\alpha_1}'$  showing the N/W relationship, while the other has the zone axis  $\langle 111 \rangle_{\alpha_2}'$ .

#### 4.4 The effect of deformation on the matrix structure.

##### 4.4.1 Deformation at room temperature

The influence of cold deformation at room temperature on the matrix structure is shown in Figures 87, 89, 91 and 93. In alloys K2 K4 the volume fraction of  $\alpha$  martensite considerably increases with small amounts of deformation (Figure 87). In alloy K4 100%  $\alpha$  martensite structure is achieved by 12% deformation whereas in alloys

K2 and K3 further deformation is required for a complete transformation to  $\alpha'$  martensite. In alloys K5, K6 and K7 the initial deformation product of austenite is mainly the  $\epsilon$  phase. Subsequent deformation leads to the formation of increasing the amounts of  $\alpha'$  at the expense of both  $\epsilon$  and  $\delta$  phases. (Figure 91) The increase in the volume fraction of the  $\alpha'$  martensite is also associated with increasing the amount of molybdenum. Figure 91 shows that alloy K7 containing approximately 5% Mo has a greater amount of  $\alpha'$  martensite present than alloys K6 and K5 with 2% and 0% Mo respectively.

#### 4.4.2 Deformation at $-196^{\circ}\text{C}$

The influence of cold deformation by swaging on the formation of  $\epsilon$  and  $\alpha'$  phases was studied in detail. Deformation at  $-196^{\circ}\text{C}$  was found to be more effective than deformation at room temperature. The complete  $\epsilon \rightarrow \alpha'$  transformation in alloys K2, K3 and K4 took place with much smaller amounts of deformation compared with the amount of deformation required at room temperature (Figure 98). In alloys K5  $\rightarrow$  K7 the initial stages of deformation up to 12% resulted in an increase in the amount of  $\epsilon$  martensite. With further deformation the amount of  $\alpha'$  martensite increases with increasing the amount of deformation. The amount of  $\alpha'$  martensite also increases with the addition of molybdenum, which tends to promote the  $\delta \rightarrow \alpha'$  transformation.

The matrix structure present after deformation at  $-196^{\circ}\text{C}$  was examined by stain etching. At the beginning it was found rather difficult to etch the specimen. A slight alteration both in electro-polishing condition and etchant composition made it possible to examine

the structures of the alloys (Figures 95, 96, 97, 98, 101, 102 and 103). Figure 101 shows the optical microstructure of alloy 77 quenched and 6% deformed at  $-196^{\circ}\text{C}$ . The transformed region of austenite (brown) to  $\epsilon$  martensite (yellow) and the growth of  $\alpha$  martensite (blue) inside  $\epsilon$  martensite can be seen in Figures 101 and 102. Figure 103 shows fine matrix structure which consists of martensite ( $\sim 58\%$ ),  $\alpha$  martensite ( $\sim 26\%$ ) and retained austenite (11%).

#### 4.5 Ageing Behaviour

##### 4.5.1 Ageing after water quenching

The influence of ageing upon the matrix structure is shown in figures 37  $\rightarrow$  42. Alloys K2  $\rightarrow$  K4 shows the most marked change in matrix structure with increasing ageing temperature. In alloys K2  $\rightarrow$  K4 the  $\epsilon \rightarrow \delta$  transformation takes place very early in the ageing sequence (Figures 37  $\rightarrow$  39). When the quenched alloys K2  $\rightarrow$  K4 are aged around  $700^{\circ}\text{C}$  a maximum occurs in the  $\delta \rightarrow \epsilon$  transformation. In alloys K2  $\rightarrow$  K4 the amount of austenite increases at temperatures in excess of  $350^{\circ}\text{C}$  and reaches a peak value between  $550$  and  $600^{\circ}\text{C}$  depending upon the alloy composition (See Figures 37  $\rightarrow$  39).

An increase in the amount of  $\delta$  is associated with an increase in hardness (Figures 20  $\rightarrow$  29). This  $\delta$  is thought to be the finely divided  $\delta$ -phase precipitate. It was possible to identify  $\delta$ -phase precipitate which appeared to be faulted particles as shown in Figures 49, 52, 60 and 68. In the temperature range between  $550^{\circ}\text{C}$  -  $700^{\circ}\text{C}$  the amount of  $\epsilon$  increases while the volume fraction of  $\delta$  decreases (Figures 37  $\rightarrow$  39). This occurs as a result of  $\delta \rightarrow \epsilon$  transformation which takes

place after ageing above 550°C. This will be discussed in the discussion section. The  $\epsilon \rightarrow \alpha'$  transformation was observed after ageing at 350°C in alloys K2  $\rightarrow$  K4. The amount of  $\alpha'$  martensite transformed from  $\epsilon$  martensite was found to be dependent on the alloy composition. The addition of 4.85% Ni to the 13% Mn alloys (K2  $\rightarrow$  K4) resulted in a 30% increase in the amount of  $\alpha'$  martensite after ageing for two hours at 450°C. (Compare Figures 37 and 39). Alloy K5 showed very little change in matrix structure with increasing ageing temperature except that  $\alpha'$  showed a tendency to revert back to austenite (Figure 40). In alloys K6 and K7 at the higher ageing temperatures, considerable  $\gamma \rightarrow \epsilon$  transformation took place. Further ageing resulted in a decrease in the amount of  $\epsilon$  at the expense of  $\gamma$  (Figures 41 and 42).

Ageing of the alloys resulted in the formation of finely distributed precipitate. After ageing at 550°C for a short time (2 hours), in the region where peak hardness occurred (in the quenched and aged condition) precipitates were observed at the lath boundaries and within the laths (Figure 43). Figure 43 also shows precipitates both within the lath and on the lath boundaries.

#### 4.5.2 Deformation and Ageing

The sequence of phase changes occurring during ageing after deformation was similar to those observed in the quenched alloys. (115)  
Although ageing after deformation resulted in superior mechanical properties, especially in alloys K5  $\rightarrow$  K7 (compare Figures 26  $\rightarrow$  38 with 123  $\rightarrow$  128 and 141 with 143), the microstructure was not signif-

icantly different. The only obvious difference was that the quenched deformed and aged samples showed a much finer substructure (Figure 129).

#### 4.6 Formation of Precipitate

Electron diffraction analysis was used to identify the precipitate. The main studies for identification were concentrated on the faulted particles which were observed in the 15% Mn alloys (K2 → K4) and also fine precipitates, both in 13% Mn alloys and 17% Mn alloys. Faulted particles can be seen clearly in Figures 49 and 60. These faulted particles tend to grow quite rapidly on further ageing (Figure 68).

Examination of the dark field image showed that faulted particles were responsible for the streaked pattern shown in Figure 50. Due to the same atomic interplanar spacing between both precipitates and matrix, it was rather difficult to identify the precipitate. Further examination was carried out by X-ray diffraction on the grossly over-aged sample. The diffraction trace did not show any extra peaks which would appear due to the precipitate. It was decided to carry out further electron diffraction experiments on over-aged specimens. In this case it was possible to obtain a diffraction pattern from the fine precipitate itself (Figure 130). The indexed diffraction pattern for precipitate did not seem to fit exactly any of the known standard precipitate patterns. It seems more likely that this is a  $A_3B$  type precipitate with hexagonal structure and c/a ratio slightly different from the known  $(\text{Ni}_3\text{Ti})$  type precipitate (Table 5).

The identification of faulted precipitate which occurred predominantly in the 13% Mn alloys proved to be far more difficult than the identification of the fine precipitates. Extensive selected area electron diffraction and dark field analysis showed that the precipitate was a faulted  $\gamma$ -phase particle (See Figures 49 and 60). The existence of  $\gamma$ -phase precipitate has also been reported in Fe-Mn-Co alloys by Suzuki. (116)

#### 4.7 Austenite Reversion

Overaging in these alloys is mainly due to the reversion of the martensite matrix to austenite. Austenite reversion can be markedly affected by alloying addition. In nickel maraging steels molybdenum has been reported to enhance the austenite reversion. (91) In the present alloys molybdenum shows the same effect as that observed in nickel maraging steels. Figure 66 shows the increase in the amount of reverted austenite with increasing the amount of molybdenum.

The influence of ageing time on the austenite reversion was investigated in detail. It was found that the rate of austenite nucleation at very short ageing time was higher than at longer ageing periods. (Figure 66). The ageing time did not significantly affect the austenite reversion in alloys K5  $\rightarrow$  K7. (Figure 67). The effect of ageing temperature (525<sup>o</sup>C and 600<sup>o</sup>C) and ageing time (0,1-1000 hrs) was also studied in alloy K4 (Figures 64 and 65). As expected it was found that the amount of reverted austenite increases with increasing temperature from 525<sup>o</sup>C to 600<sup>o</sup>C. Austenite formation was observed

at the lath boundaries. Figures 48, 51 and 55 shows the micro-structure of aged alloy showing elongated austenite ribbons strung out at the lath boundaries.

#### 4.8 Mechanical Properties of Quenched and Aged Alloys

##### 4.8.1 Toughness Data

All the alloys examined in the as quenched condition showed good impact properties at room temperature (Figure 145). It was observed that the alloys K4 and K7 which contain 4.85% Mo showed a steady impact toughness transition with changing test temperature, in contrast to the rapid transition of the alloys K2, K3, K5 and K6.

Ageing of the alloys K2 K4 at temperatures between 350°C and 500°C resulted in severe embrittlement (Figure 146). A rapid decrease in impact toughness occurred after a short ageing time (2 hrs). The alloy K4 containing 4.85% Mo showed different behaviour from the alloys K2 and K3. Ageing at 550°C produced rapid embrittlement in alloy K4 whereas the alloys K2 and K3 showed an improvement (Figure 146). The broken Charpy specimens were examined by X-ray diffraction. It was found that a large amount of reverted austenite, approximately 50% after ageing for 2 hours at 550°C, was present in alloy K4 (Figure 39). Although the alloys K2 → K7 show a ductile brittle transition when subjected to impact tests over the temperature range -196°C to 100°C, molybdenum improves the impact properties of alloys in subzero temperatures (Figure 145). The influence of ageing after deformation on

the impact properties of alloys K5 → K7 is shown in Figure 148. Examination of results shows that the alloys K5 → K7, in the quenched, deformed and aged condition showed much better impact properties than alloys K2 → K4 in the quenched and aged condition after ageing for 2 hours over 500°C. (Compare Figures 146 with 148).

#### 4.8.2 Hardness Data

Hardness measurements showed that significant age hardening occurred in alloys K2 → K4 by ageing after quenching. Figures 26 → 33 show the effect of ageing temperature and ageing time on the hardness of all the alloys. Ageing after deformation did not significantly affect the hardness of alloys K2 → K4 at various temperatures (Figures 117 → 122). Figures 26 → 33 show that ageing after quenching did not produce considerable hardening in alloys K5 → K7. However, deformation and ageing both at room temperature and -196°C resulted in a considerable increase in hardness of these alloys (Figures for hardness 85 and 86, for ageing 123 → 128). Although there is a small amount of  $\alpha'$  formed during deformation in alloy K5 at -196°C compared with alloys K6 and K7, the hardness increases quite substantially (Compare Figure 86 with 82). It seems probable that increase in hardness as a result of deformation is partly due to strain hardening of the austenite.

Examination of the hardness results indicates that alloys containing considerable amounts of retained austenite are generally softer and do not harden appreciably. Alloy K7 containing 6.8% Co and 4.85% Ni in the quenched and deformed condition showed the most

useful hardening effect suggesting a similarity to the synergistic effect well known in nickel maraging steels.

#### 4.8.8 Tensile Test

The Tensile properties of all alloys in the quenched conditions are shown in Figures 139 and 140. The alloy K4 containing 4.85% Mo shows the highest tensile stress of 120 kg/cm<sup>2</sup> (approx. 11700 N/m<sup>2</sup>). Examination of yield stress showed that ageing did not significantly affect the yield stress of the alloys (Figures 139 and 140). The influence of ageing temperature after quenching on the tensile stress of the alloys K5 K7 was also ineffective (Figure 140).

For evaluation of mechanical properties in the quenched and deformed condition, tensile test pieces of alloys K5 K7 were pre-strained up to 10 per cent in an Instron testing machine prior to ageing. Considerable improvement in the ultimate tensile strength was observed after ageing (Figure 140). Alloys K8 K4 in the deformed and aged condition were not examined because the test pieces started to neck after only 6% elongation. This amount of deformation was not sufficient to examine thoroughly the effect of deformation on the mechanical properties of these alloys.

### 5. Discussion

In the present investigation, it was not possible to observe a separate Ms temperature for the  $\gamma \rightarrow \epsilon$  and  $\epsilon \rightarrow \alpha'$  transformations.

This may arise due to:

- (i) the similar atomic volume of the  $\epsilon$  and  $\delta$  phases.
- (ii) simultaneous occurrence of the  $\gamma \rightarrow \epsilon$  and  $\epsilon \rightarrow \alpha'$  transformations.

The first explanation is unlikely because X-ray diffraction results did not show any similarity between the atomic volume of the  $\epsilon$  and  $\delta$  phases (see Table 4). However, it is possible that the true unit cell of the cph  $\epsilon$  phase differs slightly from the calculated value and this could explain the absence of a separate Ms temperature for the  $\gamma \rightarrow \epsilon$  and  $\epsilon \rightarrow \alpha'$ .

In the second case it is possible that the contraction resulting from the  $\gamma \rightarrow \epsilon$  transformation is compensated by the expansion produced by the  $\epsilon \rightarrow \alpha'$  transformation. Furthermore, the  $\gamma \rightarrow \alpha'$  expansion cannot be neglected, and it is possible that the Ms first observed is not necessarily the true Ms for the  $\gamma \rightarrow \alpha'$  transformation. On balance it would appear that separate Ms temperatures are not observed due to the simultaneous occurrence of the  $\gamma \rightarrow \epsilon$  and  $\epsilon \rightarrow \alpha'$  transformations rather than  $\delta$  and  $\epsilon$  phases having similar atomic volumes.

In order to produce a martensitic transformation an alloy has to be undercooled from  $T_0$  to Ms because energy has to be available to supply the non-chemical energies, such as interfacial energy and strain energy. The available energy at any temperature T is the difference between the free-energy of austenite,  $F^\gamma$  and the martensite  $F^{\alpha'}$  at that temperature. This difference, usually called the driving force is:

$$\Delta F^{\alpha' \rightarrow \gamma} = F^\gamma - F^{\alpha'} \dots \dots \dots (12)$$

and is positive at temperatures at which martensite is the more stable phase. The effect of alloying elements on the driving force for the

martensitic transformation is important. In the present investigation an increase in the manganese content from (approx.) 13% to 17% lowers the  $M_s$  temperature. Manganese in this case appears to be acting in a similar manner to nickel which also lowers the  $M_s$  temperature in ferrous alloys. In contrast to the effect of manganese, altering the molybdenum content from 0% to 4.85% results in an increase in  $M_s$  temperature for both the 13% Mn and also the 17% Mn alloys. This effect on the  $M_s$  is in contrast to the known effect of molybdenum which generally lowers the  $M_s$  temperature. This unusual behaviour of molybdenum has also been reported in other Fe-Mn alloys containing molybdenum. (79)

It is suggested that this anomalous behaviour of molybdenum in Fe-Mn alloys is related to its effect on the stacking fault energy of the austenite. In alloys containing more than 10%Mn, it has been suggested that the transformation sequence is influenced by the stacking fault energy of austenite. (81) For the  $\gamma \rightarrow \epsilon$  transformation a small driving force is required because the appearance of  $\epsilon$  martensite, which is essentially composed of stacking faults on every alternate  $\{111\}_\gamma$  austenite plane occurs when the austenite stacking fault energy approaches zero i.e. 10%Mn. (81) In contrast to this for the  $\gamma \rightarrow \alpha'$  transformation a high driving force is required. We can consider the driving force as that energy which is required to dissociate the partial dislocations or provide the re-combination of partials. Therefore, it is possible to make a correlation between the driving force, stacking fault energy and  $M_s$  temperature. In the

present alloys addition of molybdenum increases the Ms temperature in contrast to manganese which lowers the Ms temperature. This is related to the effect of molybdenum on the partial dislocation separation. An increase in the molybdenum content is thought to increase the driving force for partial dislocation to combine with each other to produce  $\alpha'$  from austenite. As a consequence of this the Ms temperature of alloy is increased and this may be related to an increase in stacking fault energy. Manganese in contrast to molybdenum lowers the Ms temperature and also increases the driving force for the dissociation of partials which produce  $\epsilon$  martensite from austenite rather than the direct sequence of  $\alpha$  martensite from austenite.

The occurrence of internally twinned lath martensite in which the twins are blocky twins rather than fine internal twins observed in these alloys, has provoked much discussion. The theories which are most closely related to experimental observations are based on the multiple shearing mechanism suggested by Acton and Bevis (121) and Ross and Crocker (122). In both theories a shear on  $\{112\}_{\alpha'}$  is chosen as one of the shear components, because of the observations of twins on  $\{112\}_{\alpha'}$  in some high carbon martensites exhibiting a  $\{225\}_{\gamma}$  habit. It has been suggested that the twin thickness is related to the magnitudes of the shape strain and lattice invariant shear. The maximum twin widths in ferrous alloys are reported of the order 0.1  $\mu$ m. The lattice invariant shear system  $(111)_{\gamma} \langle \bar{1}2\bar{1} \rangle_{\gamma}$  was chosen in the present investigation because the  $\alpha$  martensite was associated with faulting

(31)

of the austenite to give hexagonal . The relation between low stacking fault energy and lath martensite can be clarified in the effect of prior deformation on the martensite transformation. In some alloys, transformation is stimulated by small amounts of deformation whereas large amounts results in retardation. Alloys in this class have low stacking fault energy. In high stacking fault alloys the transformation is retarded regardless of the amount of prior deformation. Lath martensite is known to occur in alloy systems exhibiting stimulation. The connection between lath martensite and low stacking fault energy may be used to give a further explanation of this stimulation by prior deformation. If the prior deformation leads to the formation of  $\epsilon$  which in the present investigation increases with deformation then these could act as nuclei for subsequent  $\alpha'$  formation (Figures 89 and 90). This would only occur in low stacking fault energy austenites. However, this

nucleation mechanism is not sufficient to explain whether the lath martensite is formed by inhomogenous shear on system II  $\left[ \begin{matrix} (111) \\ \delta \end{matrix} \left\langle \begin{matrix} 121 \\ \delta \end{matrix} \right\rangle \right]$  i.e.  $\begin{matrix} (101) \\ \alpha \end{matrix} \left\langle \begin{matrix} 101 \\ \alpha \end{matrix} \right\rangle$  low stacking energy alloys] or it follows system I  $\left[ \begin{matrix} (110) \\ \delta \end{matrix} \left\langle \begin{matrix} 110 \\ \delta \end{matrix} \right\rangle \right]$  i.e.  $\begin{matrix} (112) \\ \alpha \end{matrix} \left\langle \begin{matrix} 111 \\ \alpha \end{matrix} \right\rangle$  high stacking fault energy alloys] accommodate the inhomogenous shear by slip instead of twinning.

(14)

Kelly and Nutting have suggested by comparison of the known features of low carbon martensite that the first view is possible.

The formation of twin related laths parallel to  $\langle \bar{1}\bar{1}0 \rangle_{\delta}$  and lying in sheets in  $\left\{ \begin{matrix} 111 \\ \delta(14) \end{matrix} \right\}$  may also be explained by a mechanism suggested by Kelly and Nutting. According to this a first shear

occurs which is in fact half of the stacking fault shear. The atoms in the fault need only be shifted by a small amount  $\frac{a}{12} \langle 112 \rangle$  and produces three close-packed planes in which the atomic arrangement is the same as that of austenite.

The morphology and distribution of the twins observed in these alloys is different from those seen in other alloy systems. Figure 15, 16 and 105 show the twin related regions which in some cases do not extend the full width of the lath. The maximum width of twin related regions observed in these alloys was in the order of 1.4  $\mu$ m. Furthermore, deformation did not produce any significant increase in the number of internally twinned regions nor was there any appreciable reduction in twin widths after deformation (Figure 105). In view of the twin widths it seems therefore reasonable to assume that the twin related regions are transformation twins rather than deformation twins. The fine twinned martensite produced by deformation, as previous workers reported, was not observed in these alloys. (48) (81) It is proposed that twin related substructure is due to a transformation sequence of  $\gamma \rightarrow (\epsilon \text{ or faulted } \gamma) \rightarrow \alpha'$  rather than a deformation process. (123)

Fine striations in the structure were often observed throughout the investigations (Figures 42, 49, 60, 74, 77 and 82). It was attempted to identify these striations by using simple dark field and selected area diffraction pattern techniques. There was, in some cases, no distinction between the  $\gamma$  and  $\epsilon$  phases since both appeared to be the same (compare Figures 77 with 82). As it can be

seen from the diffraction pattern in Figure 50, the streaks due to the faulted particles, are parallel to  $\langle 0001 \rangle_{\epsilon}$  or  $\langle 111 \rangle_{\delta}$  directions. The existence of such streaks suggest that both  $\delta$  and  $\epsilon$  phases are heavily faulted on the  $(111)_{\delta}$  and  $(0001)_{\epsilon}$  planes respectively. (54)

It has been suggested that the twin substructure is produced as a result of a transformation process involving overlapping regions in the matrix. (123) The overlapping structure can be either stacking faults or thin  $\epsilon$  bands. Regardless of whether the initial overlapping structure in the austenite is stacking faults or thin  $\epsilon$  bands, the orientation relationship between adjacent regions in the martensite laths produced in this manner will be similar because the close-packed direction  $\langle 110 \rangle$  in the  $\delta$  is parallel to the close-packed direction  $\langle 11\bar{2}0 \rangle$  in the  $\epsilon$  phase. In other words the overlapping sheets of faulted  $\delta$  or  $\epsilon$  transform individually by different variants of the Kurdjumov-Sachs relationship. In the present investigation a number of overlapping structures were observed in these alloys which support the idea that the twin substructure is due to a transformation sequence of  $\delta \rightarrow (\epsilon \text{ or faulted } \delta) \rightarrow \alpha'$ . The overlapping structure is shown in Figures 24, 57, 71 and 106.

There have been many arguments as to whether  $\epsilon$  is an intermediate phase in the  $\delta \rightarrow \alpha'$  transformation. Dash and Otte (28) take the view that  $\epsilon$  is a consequence of the large shear strain produced by the  $\delta \rightarrow \alpha'$  transformation, while Venables, Reed and Kelly (50) support the idea that  $\epsilon$  forms before  $\alpha'$  and  $\alpha$  martensite then forms (58) (31)

within the  $\epsilon$  bands. The association between  $\alpha$  martensite and  $\epsilon$  phase determines the shape of the martensite. The reason for lath appearance is that the growth of the  $\alpha$  martensite is to a large extent restricted by the width of the  $\epsilon$  band. The habit plane of the martensite is perpendicular to the  $\epsilon$  band and would require further faulting to increase the width of the  $\epsilon$  band. This restriction does not apply to the growth in the direction  $\langle 1\bar{1}0 \rangle_{\delta}$  which lies in the plane of the  $\epsilon$  band and as a consequence of this the  $\alpha$  martensite forms as a lath with  $\langle 1\bar{1}0 \rangle_{\delta}$  long direction and a  $(\bar{1}\bar{1}2)_{\delta}$  habit plane. The schematic representation shown in figure 9 indicates the growth of  $\alpha'$  martensite crystals with a  $(225)_{\gamma}$  habit plane from austenite. Manganon et al have suggested that the growth of the  $\epsilon$  phase in the  $\delta$  matrix occurs by the movement of  $a/6 \langle 211 \rangle$  partial dislocation. The pile-up of such dislocations against twin boundaries or grain boundaries produces a compressed region. The nucleation of  $\alpha'$  crystals is characterised by the presence of a stressed region which is in the  $\langle 211 \rangle_{\delta}$  direction. Since the  $\epsilon$  phase is more dense than  $\alpha'$  it is more stable than  $\alpha'$ . The excess pressure brought about in the stressed region can be relieved if an expansion to the bcc lattice takes place. This is in fact favourable since  $\alpha'$  has a larger atomic volume than  $\epsilon$ . As a result of the stress-relieving effect the  $\alpha'$  crystals begin to form and continue growing inside the  $\epsilon$  phase plates. It is not possible to distinguish between these possibilities as far as the crystallography of the formation of  $\alpha'$  is concerned and both these

possibilities lead to the same consequences, provided that the formation or faulting is inhomogeneous. If the first view is correct  $\alpha'$  can nucleate  $\epsilon$ . If an  $\alpha$  martensite lath is formed it would produce an  $\epsilon$  band. In fact in the present investigation a large number of  $\alpha'$  martensite laths were observed in a given  $\epsilon$  band (Figure 16). Even though the first bands of  $\epsilon$  form as a consequence of  $\alpha'$  formation at a later stage in the transformation the second possibility would be obeyed. In other words,  $\alpha$  martensite would form in these pre-existing  $\epsilon$  bands. However, the above explanation may not be sufficient to clarify the mechanism of  $\alpha$  martensite formation as a consequence of the intersection of bands. It has been previously reported in the present investigation that the  $\alpha$  martensite crystals were observed in an  $\epsilon$  band with no indication of intersection of  $\epsilon$  bands which may support the first idea (Figure 82). However, this would not necessarily mean that the  $\alpha$  martensite is produced by direct  $\gamma \rightarrow \alpha'$  transformation and then  $\alpha'$  transforms to  $\epsilon$  as a consequence of large shear strain. In order to clarify this suggestion let us assume that the  $\alpha'$  is produced by direct  $\gamma \rightarrow \alpha'$  transformation. The stressed region around the  $\alpha'$  crystals, according to the mechanism described by Dash and (28) Otte, would act as a nucleation site for  $\epsilon$  crystals. The nucleation would start from both  $\alpha'$  crystals due to the stressed region around them. The growing of  $\epsilon$  platelets from  $\alpha'$  crystals would intersect in a region where they meet each other. The intersecting region itself would be another stressed region which would destroy the long

straight sided appearance of  $\epsilon$  crystals lying between two  $\alpha'$  crystals. In the present investigation there was no stressed region observed in the  $\epsilon$  crystals lying between  $\alpha'$  crystals (Figure 82). It would then be reasonable to assume that the  $\epsilon$  martensite cannot nucleate from the stressed region around the  $\alpha$  martensite. This mechanism is also unable to explain the occurrence of internally twinned lath martensite which occurs as a result of transformation sequence ( $\gamma \rightarrow \epsilon$  or faulted  $\gamma \rightarrow \alpha'$ ) in low stacking fault (14) energy alloys.

Further evidence that the  $\alpha$  martensite forms from the martensite and that the  $\alpha'$  does not nucleate the  $\epsilon$  phase can be obtained from the results of the deformation studies on as quenched samples (Figures 89  $\rightarrow$  92).

X-ray and optical metallographic examination of the deformed samples (K5  $\rightarrow$  K7) show that the amount of  $\epsilon$  martensite increases quite substantially in the early stages of deformation whereas little change occurs in the volume fraction of the  $\alpha'$  phase (Figures 89  $\rightarrow$  92). The occurrence of  $\epsilon$  phase before  $\alpha'$  as a result of  $\gamma \rightarrow \epsilon$  transformation also confirms the idea that  $\epsilon$  is an intermediate phase in some  $\gamma \rightarrow \alpha'$  transformations in low stacking fault energy alloys. Figures 89  $\rightarrow$  92 also show that further deformation increases the amount of phase at the expense of  $\epsilon$  phase. This observation is in good agreement with the arguments of those workers who conclude that (43) (81) is an intermediate phase in the  $\gamma \rightarrow \alpha'$  transformations.

A model to explain the fcc  $\rightarrow$  cph  $\rightarrow$  bcc transformation was (43) developed by Stacey, which necessitates the deformation of the cph

structure along the principal directions. The atomic arrangement shown in Figure 151 is considered to correspond to the minimum atom shift to obtain the bcc unit cell from the cph lattice. The change in lattice parameter shown in Figure 152 indicates that an atom movement is involved in the three principal directions of the cph lattice. Thus for the transformation, a situation of invariant plane strain is required where there is a 9% contraction in the  $\langle 10\bar{1}0 \rangle_{\text{cph}}$  direction, 11% expansion in the  $\langle \bar{1}2\bar{1}0 \rangle_{\text{cph}}$  direction and no change in the  $\langle 0001 \rangle_{\text{cph}}$  direction (Figure 152). This gives a position where one vector is undistorted (0001)cph and another undistorted but rotated. The plane which contains both of these vectors is therefore an invariant plane which is approximately  $(10\bar{1}0)_{\epsilon} // (\bar{1}\bar{1}2)_{\gamma}$ . This proposed mechanism is similar to Bain's correspondence (See Figure 4) which predicts two principal strains i.e. 12% expansion and approximately 20% contraction for fcc to bcc transformation. This model also indicates that the formation of cph  $\epsilon$  as an intermediate phase between fcc and bcc would involve negligible further atom shifts. Consequently fcc  $\rightarrow$  cph  $\rightarrow$  bcc sequence is described as a combination of a partial dislocation shear which produces the intermediate cph  $\epsilon$  phase (in this case lattice invariant shear) along with a Bain type martensite shear to produce a bcc lattice from cph structure.

The habit plane determined for lath martensite was close to  $(\bar{1}\bar{1}2)_{\gamma}$  (See Figures 149 and 150). The transformation sequence whether  $\gamma \rightarrow \alpha'$  or  $\gamma \rightarrow \epsilon \rightarrow \alpha'$  did not affect the  $\alpha$  martensite habit plane. These observations are in agreement with those of previous workers for low stacking fault energy steels. (31) (43) (81)

The diffraction pattern  $\langle 111 \rangle_{\alpha'} // \langle 100 \rangle_{\alpha}$  shown in Figure 138 is reported to occur as a result of twinning in austenite prior to deformation. (S1) In the present investigation this type of orientation relationship was explained as two adjacent laths adopting different variants of the Kurdjumov-Sach orientation relationship,  $\langle 111 \rangle_{\alpha'} // \langle 100 \rangle_{\alpha'}$  orientation relationship would also explain the blocky appearance of the martensite laths frequently observed in the alloys.

It is suggested that manganese increases the number of partial dislocations by lowering the stacking fault energy. This results in a number of  $\alpha'$  martensite nucleation sites. In other words in the same length of  $\{111\}_{\gamma}$  plane the number of growing martensite laths is increased. Therefore, these martensite laths cease growth when they impinge on one another and produce a strain (in this case the orientation relationship which leads to the smallest strain is  $\langle 111 \rangle_{\alpha'} // \langle 100 \rangle_{\alpha'}$ ). As a consequence of this argument the blocky lath martensite take the form of blocks and should consist of impinging laths where the interface between the blocks should be  $\{112\}_{\gamma}$  which is in agreement with experimental results obtained by trace analysis.

There have been many arguments as to whether  $\alpha' \rightarrow \epsilon$  transformation occurs on ageing. In the present investigation X-ray results showed no conclusive evidence in support of the  $\alpha' \rightarrow \epsilon$  transformation. It has been suggested that a rapid heating rate may suppress the  $\alpha' \rightarrow \epsilon$  transformation and that when the heating rate

is slow the reverse shear transformation is suppressed. In the present investigation experiments carried out with various heating rates and showed that the heating rate had no effect on the transformation. The second explanation can also be dismissed because martensitic transformations would not be suppressed by rapid heating since transformations are generally athermal. Since the maximum heating rate employed in this investigation was  $1000^{\circ}\text{C}/\text{min}$ , it is still possible that the heating rate was not sufficient to suppress a diffusional transformation which occurred at a lower temperature than the martensitic reversion temperature. This would require the  $\alpha' \rightarrow \epsilon$  transformation temperature to be above  $700^{\circ}\text{C}$ , which is unlikely as the  $\epsilon' \rightarrow \gamma$  transformation start temperature was about  $300^{\circ}\text{C}$ .

In alloys K2  $\rightarrow$  K4  $\epsilon \rightarrow \gamma$  transformation takes place on ageing above  $300^{\circ}\text{C}$  (Figures 37-39). The increasing amount of  $\gamma$  in the temperature range between  $300 - 550^{\circ}\text{C}$  could be due to  $\epsilon \rightarrow \gamma$  transformation and an increase in the amount of  $\gamma$ -phase particles which nucleate in the early stages of ageing. In alloy K4, electron microscopic investigations indicated the existence of such a precipitate (Figures 49 and 60). Figures 37-39 also show that the amount of  $\gamma$  reached a maximum and then decreases. This occurs as a result of  $\epsilon \rightarrow \gamma$  and also  $\alpha' \rightarrow \gamma$  transformations which take place after ageing above  $425^{\circ}\text{C}$ . In the temperature range between  $550^{\circ}\text{C} - 700^{\circ}\text{C}$  the amount of  $\epsilon$  phase increases while the volume fraction of  $\gamma$  decreases (Figures 38 and 39). This occurs as a result of  $\gamma \rightarrow \epsilon$

transformation on cooling from the ageing temperature and may be associated with compositional change in the solute. When the austenite solid solution becomes richer with solute atoms, this tends to lower the  $M_s$  temperature. The occurrence of a large amount of austenite which transforms from  $\alpha'$  by reverse shear process and also from  $\epsilon$  above  $650^\circ\text{C}$  is associated with a lower  $M_s$  temperature of the alloy. The reversion of the matrix to austenite occurs either by a nucleation and growth process and if the temperature is high enough (above the  $A_s$ ) by a reverse shear process. It has been recently suggested that the growing of austenite by nucleation may take place at the particle-matrix interface and results in the consumption of the precipitate particles. (106) This nucleation mechanism may be similar to the mechanism considered in these alloys. It is shown in Figure 64 that the amount of reverted austenite increases rapidly at the initial stages of ageing. This considerable increase in reversion is probably due to the solution of the precipitate particles and growth of austenite both at lath boundaries and within the laths. Increase in reversion may also be related to the influence of molybdenum on the kinetics of precipitation. This may be explained as follows.

Nickel is a well known austenite forming element which lowers the  $M_s$  temperature of alloys. In maraging steels, the formation of  $\text{Fe}_2\text{Mo}$  compound or dissolution of  $\text{Ni}_3\text{Mo}$  precipitate enriches the matrix in nickel. This is in favour of austenite reversion. (105) Manganese also lowers the  $M_s$  temperature of the alloys. The addition of moly-

molybdenum to manganese maraging steels may result in the formation of complex  $Fe_x-Mo$  compound which enriches the matrix in manganese. This may tend to increase the driving force for austenite reversion since the enrichment of matrix in manganese lowers the  $A_s$  temperature of alloys. The  $A_s$  temperature of alloys shown in Table 2 indicates that increasing the amount of manganese decreases the  $A_s$  temperatures of alloys while the effect of molybdenum is negligible.

The influence of reverted austenite on the mechanical properties and toughness of maraging steels has recently received a great deal of attention. Reverted austenite is reported to have no detrimental effect on mechanical properties and toughness and even improves these properties when precipitate along martensite lath boundaries. Detrimental effect on toughness is found when reverted austenite precipitates at the prior austenite grain boundaries. (124) In the present investigation in contrast to the suggestion of Pombillo et al (124) the reverted austenite which nucleated at the lath boundaries reduced the toughness of the alloys (Figures 51 and 55). However it is possible to assume that the brittleness found in the present alloys K2→K4 is due to the reverted austenite nucleated at prior austenite grain boundaries. In contrast to the detrimental effect of reverted austenite on the toughness of alloys, the yield stress increases with the introduction of reverted austenite nucleated at the martensite lath boundaries (Compare Figure 37-39 with 139). The contribution of reverted austenite to the yield stress may be interpreted by possible effects on the ability of the martensite lath boundaries to act as slip barriers. The observed adjacent laths are

not supposed to be effective as obstacles to slip since they lead to low angle type boundaries. (33) (Figure 113). When austenite forms at the martensite lath boundaries it would contribute to increasing the difficulty of transmitting slip across these boundaries. (124) This could be due to a relaxation of stress concentration at the head of dislocation piled up against the boundaries caused by the austenite. Finally it is concluded that yield stress increases with ageing time along with the increase in the volume fraction of reverted austenite and is thought to be due to the precipitation of austenite at the martensite lath boundaries.

Figures 85 and 86 show that the hardness of the alloys K5 → K7 increases drastically with increasing amounts of deformation compared with the alloys K2 → K4. This may be due to:

- (i) an increase in the volume fraction of  $\alpha'$
- (ii) fine matrix structure resulting from deformation
- (iii) work hardening behaviour of austenite.

The first case seems to be a minor effect for strengthening since no substantial increase in hardness occurs in alloys K2 → K4 after 6% deformation when compared to the alloys K5 → K7 containing large amounts of retained austenite in the as-quenched condition. In alloy K5 an increase of max 20%  $\epsilon$  is produced by 6% deformation at  $-196^{\circ}\text{C}$ . The same amount of deformation produces approximately 20%  $\alpha'$  in alloy K2. The increase in hardness in alloy K5 is higher than alloy K2 although it is considered that <sup>the</sup> contribution of 20%  $\alpha$  to the hardness would be much greater than the contribution of 20%  $\epsilon$  .

The reason for this is that alloy K5 contains an appreciable amount of austenite and work hardening behaviour of austenite plays a direct role in contributing to the hardness. It is also suggested that increasing the amount of deformation produces a much finer structure in alloys K5 → K7 as a result of  $\gamma \rightarrow \epsilon \rightarrow \alpha'$  transformation which considerably affects the hardness of the alloys.

A hardness of approximately 525 VPH<sub>30</sub> was achieved in alloy K7 after deformation prior to ageing. This is similar to the (103) hardness found in nickel maraging steels. In addition to this, good impact properties were also achieved in alloys K6 and K7 after deformation and ageing. Considerable increase in the UTS in alloys K5, K6 and K7 resulted from greater work hardening of the austenite and also the transformation of the  $\epsilon$  to  $\alpha'$  during deformation. A further increase in strength is achieved by precipitation hardening on ageing. The best combination of strength and toughness found in these alloys was attributed to the much finer structure of the matrix (Figure 103). The alloys K5, K6 and K7 deformed and aged tend to embrittle in the temperature between 350°C and 525°C. This is associated with temper brittleness as it has been previously suggested (48) (85) (125) by many workers. Although the brittle behaviour of these alloys, considering the requirements for the replacement of nickel by manganese, these alloys would seem to be suitable if the ageing temperature is between 525-550°C. (Compare Figure 143 and 140).

It was possible to obtain 100%  $\alpha$  martensite after a small amount of deformation in alloys K2, K3 and K4. This was associated with an increase in hardness. As it can be seen (Figures 117-128)

subsequent ageing did not considerably affect the hardness with increasing the amount of deformation. This was probably because the matrix was completely  $\alpha$  martensite and subsequent ageing resulted in a reduction in the amount of  $\alpha$  martensite.

Although reversion of  $\alpha$  martensite to austenite is expected to decrease the hardness, this was not observed in these alloys.

This may be due to the increase in hardening resulting from precipitation being sufficient to compensate the loss of hardness brought about by the reversion of  $\alpha$  martensite to austenite.

The occurrence of high strength in alloy K7 in the quenched and deformed condition may be attributed to the dislocation density within the lath martensite, the width of laths and also precipitation hardening effect. The first is that dislocations produced by deformation may serve as nucleation sites or as channels for more rapid diffusion of the elements participating in the ageing reaction. The high strength may also be attributed to the width of the  $\alpha$  martensite. The relation between the size of individual laths and strength has been previously reported that the strength increases with decreasing the width of martensite lath. (72) It is also suggested that the width of laths play a minor role in the strengthening after ageing and this even would be considered as an ineffective factor. (126) This may be explained by the interaction of the dislocations with the precipitate particles. The view is that the dislocation pile-up which results in strengthening is achieved by the precipitate itself not the lath boundary.

The laths containing no boundary precipitate is expected to contribute to the transmitting of the dislocations as they are orientated by low angle boundaries (See Figure 118). Therefore the precipitation at the lath boundaries is suggested to act as barriers to the movement of dislocation and results in strengthening. In <sup>some</sup> cases, the precipitates occur within the laths, the dislocations cut through these precipitate particles and contribute to the strength. This strengthening is due to the stressed field left around the precipitates. Considering this explanation it seems therefore reasonable to assume that the effect of precipitation is much stronger than the influence of the lath size on the strengthening of these alloys.

Ageing after quenching in alloy K4 containing 4.85% Mo produced considerable hardening. This was probably because the matrix contained a large amount of  $\alpha$  martensite with sufficient molybdenum in solution to promote precipitation of a molybdenum rich intermetallic phase. These findings are similar to the influence of molybdenum observed in Fe-Ni-Mo alloys. (108) Although there was evidence of precipitation during ageing in alloys K5, K6 and K7 the precipitate did not produce any appreciable hardening because of the large amounts of austenite present. Examination by electron microscopy showed that the precipitate observed in the present investigation nucleated at the lath boundaries and also within the laths. (Figures 49 and 63). This type of nucleation (127) (128) (129) has also been reported in Fe-Ni-Cr alloys by previous workers.

It was not possible to identify the precipitate by X-ray analysis in the early stages of precipitation because it was too small to be extracted electrolytically. Identification of the precipitate by electron diffraction analysis also proved rather difficult because of the large number of precipitation reflections observed. Although the dark field micrographs showed the precipitate quite clearly (Figures 48, 55 and 138), it was difficult to index the extra diffraction spots which occur due to the reflection from precipitate. This is because of the close similarity of atomic planar spacing ( $d$ ) between matrix and precipitate. An attempt was made to fit the precipitation pattern to either simple cubic, bcc, fcc or cph structures. However, the diffraction pattern did not fit any of the standard bcc, fcc and cph ratios of  $hkl$  values.

Age hardening in Fe-Co-Mn alloys is reported to take place in two stages as in the case of Fe-Co-Ni alloys. The lower temperature stage is related to the formation of an Fe-Co ordered lattice. The second occurs at higher temperatures by the formation of solute rich austenite ( $\gamma$ -phase). This has various similarities to the age hardening of the Fe-Ni-Mn alloy as reported by Suzuki and Squires. In the present investigation the occurrence of a similar precipitate ( $\gamma$ -phase) after long ageing times, further confirmed these observations (See Figures 49 and 51). In the light of previous investigations it is possible to suggest that hardening in alloys K2 K4 at lower temperatures is due to the zone formation prior to precipitation of  $\gamma$ -phase since this has been reported in

(125)

Fe-Mn-Ni. In view of the effect of manganese on the kinetics of precipitation, it is suggested that manganese tends to replace the iron in ternary ordered lattice as shown by the formula  $(\text{Fe.Mn})\text{Co}$ .<sup>(116)</sup> However, the effect of molybdenum on the nature of precipitate is still unknown. This effect may be interpreted by comparing with the influence of molybdenum on the Fe-Ni-Co and Fe-Mn-Co alloys.<sup>(105)</sup>

The effect of impact testing temperature on the impact properties of the alloys in relation to matrix structure can be explained by comparison of Figure 145 and Table 1. Although the alloys K2→K4 do not show any change in matrix structure after quenching to  $-196^{\circ}\text{C}$ , the impact values of the alloys varies depending upon the alloy composition. Increasing amount of molybdenum improves the toughness at subzero temperatures. Molybdenum also lowers the impact transition temperatures of the alloys K2→K4 (Figure 145). Figure 145 also shows that increasing the amount of manganese also improves toughness at subzero temperatures i.e. K7 with 16.3% Mn shows much better impact properties than alloy K4 with 13% Mn. This increase in impact properties is related to the amount of  $\gamma$  present on quenching to  $-196^{\circ}\text{C}$ . Examination of matrix structures by X-ray diffraction also further confirmed that alloy K7 has a greater amount of  $\gamma$  than alloys K6 and K5.

In view of the effect of molybdenum on the impact properties of alloys, it is suggested that molybdenum plays a direct part in the removal of the embrittlement. The mechanism by which it effects the segregation is not known but there is experimental evidence to

show that the element increases the activation energy for phosphorus diffusion in Cr-Ni Steels. (130) Such an effect would then retard the diffusion of phosphorus to prior austenite grain boundaries eliminating the grain boundary weakness, and this effect may also apply to the other embrittlers. However, it is well known that the segregational tendencies of molybdenum are much higher than the highly segregating alloying elements chromium and manganese. Molybdenum would be expected to segregate to the prior austenite grain boundaries during solidification and remain there during heat treatment. It is therefore possible that the actual presence of molybdenum atoms at the boundaries attracts impurity atoms to form molybdenum-impurity complexes. Such a process may prevent embrittlement by "tying-up" the impurity atoms.

## 6. CONCLUSIONS

1. The addition of molybdenum promoted the  $\gamma \rightarrow \alpha'$  transformation by raising the  $M_s$  temperature of the alloys. This is related to an increase in the stacking fault energy of austenite by the addition of molybdenum.
2. The addition of molybdenum had no effect on the  $A_2$  temperature of alloys.  $A_2$  temperature is decreased with increasing the amount of manganese.
3.  $\alpha$  martensite was observed to nucleate at the intersection of  $\epsilon$  martensite bands, having the Kurdjumov-Sachs orientation relationship. The habit plane was found to be  $(\bar{1}\bar{1}2)_\gamma$

4. Twins observed in lath martensite were transformation twins and twin substructure is due to a transformation sequence of  $\gamma \rightarrow (\epsilon \text{ or faulted } \gamma) \rightarrow \alpha'$  rather than a deformation process.

5. The  $\gamma \rightarrow \epsilon \rightarrow \alpha'$  transformations were accelerated by deformation. Initial stages of deformation promoted the  $\gamma \rightarrow \epsilon$  transformation whereas further deformation favoured the  $\gamma \rightarrow \alpha'$  transformation.

6. Considerable hardening occurred in alloys K2→K4 when the alloys are aged in the temperature range  $525^{\circ}\text{C} - 550^{\circ}\text{C}$ . Molybdenum improved the hardening of the alloys.

7. The addition of molybdenum resulted in a finely dispersed precipitate. The precipitates were determined as fcc  $\gamma$ - phase and a hexagonal phase ( $A_2B$  type). The latter nucleated on the lath boundaries and also within the laths.

8. Overaging the alloys resulted in the growth of austenite nucleated both at the lath boundaries and within the laths.

9. All the alloys could be hardened by a combination of deformation and ageing. Ageing after deformation produced the best combination of strength and toughness in alloys K6 and K7. This was because the  $\alpha'$  matrix structure formed by deformation was much finer in these alloys, compared with alloys K2 and K4 which contained large amounts of  $\alpha$  martensite before deformation, and also due to precipitation.

7. Acknowledgements

The author would like to thank the Cobalt Information Centre for financial assistance during the period of this investigation. He wishes to express his gratitude to Dr. A. Wirth for helpful advice and guidance. Thanks are also to technicians in the Department of Metallurgy at Sheffield Polytechnic for their assistance-

Table 1. Alloy Composition and Structure

						Matrix structure					
						Water quenched			Quenched to $-196^{\circ}\text{C}$		
Alloy	wt %C	wt%Mn	wt%Co	wt%Nb	wt%Mo	$\gamma\%$	$\epsilon\%$	$\alpha\%$	$\gamma\%$	$\epsilon\%$	$\alpha\%$
K2	0.029	12.5	4.8	0.056	-	3	50	47	2	51	47
K3	0.013	13.0	4.8	0.073	1.9	3	48	49	3	48	49
K4	0.013	12.5	4.9	0.094	4.85	3	42	55	2	42	56
K5	0.009	17.2	6.55	0.058	-	28	63	9	20	71	9
K6	0.014	16.8	6.70	6.075	2.05	33	54	13	19	65	16
K7	0.016	16.3	6.80	0.095	4.85	42	51	7	25	63	12

Table 2. Transformation Temperature

Alloy	$M_s^{\circ}\text{C}$	Cooling rate $^{\circ}\text{C}/\text{min}$	$A_s^{\circ}\text{C}$	Heating rate $^{\circ}\text{C}/\text{min}$
K2	110-115-115	50-700-1400	650	50-1000
K3	155-160-164	50-600-1400	650	50-1000
K4	188-200-210	50-800-1400	650	50-1000
K5	45-45-45	50-400-1400	600	50-1000
K6	87-90-95	50-500-1400	600	50-1000
K7	100-105-110	50-800-1400	600	50-1000



Table 3 Thin Foil Preparation

	Polishing	Penetration
Electrolyte	25% Perchloric acid + 75% Methanol	5% Perchloric acid + 95% Methanol
Voltage (V)	18	9
Temperature ( $^{\circ}$ C)	20	-60
Time (sec)	9	variable

Table 4 X-ray Diffraction Results

Phase	Plane	hkl	V	a $\text{A}^{\circ}$	c/a
$\epsilon$	10.1	1.941	11.370	a=2.571 c=4.06	1.57
$\gamma$	200	1.793	11.528	3.586	-
$\alpha$	200	1.432	11.695	2.86	-

$d_{hkl}$  - atomic interplanar spacing

V - atomic volume of unit cell

a - lattice parameter

Table 5  $A_3B$  type precipitate  $c/a = 1.33$

Plane	$d_{hkl}$
00.1	4.06
10.0	3.04
00.2	2.04
10.1	2.20
10.2	1.607
11.0	1.519
20.0	1.315
11.2	1.216

Table 6  $d_{hkl}$  values for  $\delta$ ,  $\epsilon$  and  $\alpha'$  phases

a=2.86 $\alpha'$		a=3.586 $\delta$		a=2.571 c=4.06 $\epsilon$	
planes	$d_{hkl}$	Planes	$d_{hkl}$	Planes	$d_{hkl}$
110	2.027	111	2.070	10.0	2.195
200	1.432	200	1.797	00.2	2.045
211	1.170	220	1.268	10.1	1.941
220	1.013	311	1.081	10.2	1.496
310	0.906	222	1.035	11.0	1.280
222	0.828	400	0.896	10.3	1.159
123	0.766	331	0.823	20.0	1.110
400	0.717	420	0.802	11.2	1.080
411)	0.676	333)	0.690	20.1	1.070
330)		511)		00.4	1.010

REFERENCES

	<u>Year</u>	<u>Volume</u>	<u>Page</u>
1. R.B. YEO Trans AIME	1962	224	1222
2. R.B. YEO Trans AIME	1964	57	48
3. J.W. CHRISTIAN "The decomposition of austenite by diffusional process" New-York and London (interscience publishers)	1962		387
4. M.S. WISCHSLER, D.S. LIBBERMAN and T.A. READ.... Trans AIME	1955	26	473
5. H.C. BAIN Trans AIME.	1924	70	25
6. G.V. KURDJUMOV and G. SACHS Z.Phys.	1930		
7. Z. NISHIYAMA Sci,Rept. Tohoku Uni.	1934	34	327
8. A.B. GREENINGER and A.R. TROIANA Trans AIME	1949	145	291
9. M.S. WISCHSLER, D.S. LIBBERMAN and T.A. READ Trans AIME	1953	197	1503
10. J.S. BOWLES and J.K. MACKENZIE Acta Met.	1954	2	129
11. T.B. MASSALSKI "Phase transformation" American Society for Metals from session Oct 12/13th.	1968		433
12. B.A. WILSON Phd.thesis Univ.Liverpool	1965		
13. R.H. GOODENOW, S.J. MATOS and R.F. LIBBERMAN Trans. Met.Soc. AIME	1963	227	651
14. P.H. KELLY and J.NUTTING J.I.S.I	1961	197	199
15. T.HOMMA J.Japan Inst.of Metals.	1957	21	126
16. J.W. CHRISTIAN "The mechanism of phase transformation in crystalline solids" "Inst.of metal monograph.	1969	33	129
17. G.KRAUSS and A.R.MARDER Met.trans-action.	1971	2	2343
18. G. SWANSON and J.G.PARR JISI	1964	202	45
19. J.P.PASCOVER and G.V. RADCLIFFE Trans AIME	1968	242	623

		<u>Year</u>	<u>Volume</u>	<u>Page</u>
20.	E.A. WILSON JISI	1968	206	164
21.	T.A. BELL and W.S. OWEN Trans AIME	1967	239	1940
22.	T.A. BELL and W.S. OWEN J.I.S.I.	1967	205	223
23.	H.G. BRYANS, K.BELL and V.M.THOMAS The mechanism of phase transformation in crystalline solids. Inst.of Metals Monograph.	1969	33	181
24.	G.R. SPEICH and D. ROBERTSON Acta.Met.	1965	13	381
25.	B.R. BANNERJEE, J.J. HAUSER and J.M. CAPENOS Met.Sci. J.	1968	2	76
26.	W.S.OWEN, E.A. WILSON "The Physical properties of Martensite and Bainite. I.S.I. Spec.Rept.	1965	93	53
27.	C.M. WAYMAN and G.J. ALTSTETTER Acta Met.	1962	10	992
28.	J.DASH and H.M. OTTE Acta Met.	1963	11	1169
29.	R. LAGREBORG Acta Met	1964	12	823
30.	P.M. KELLY "High alloy Steels"J.I.S.I. Spec.Rept.	1964	86	146
31.	P.M.KELLY Acta Met.	1965	13	239
32.	P.M. KELLY and J. NUTTING Proc.Royal Soc.	1960	259	45
33.	J.M. CHILTON, G.J. BANTON and G.R.SPEICH JISI	1970	18	184
34.	R. DULLOUCH and B.A. BILBY Proc.Phs.Soc.	1966	1369	1279
35.	W.S. OWEN, E.A. WILSON and T.A. BELL "High Strength Material" Ed.V.F.ZACKAY	1965		295
36.	C.M. WAYMAN "Physical Properties of Martensite and Bainite" ISI Spec.Rept.	1965	93	153
37.	T. SAMBONGI, J.Phys.Soc.Japan.	1965	20	1370
38.	P.R. SWANN Corrosion	1963	119	102
39.	A.J. GOLDMAS and C.N.J.WAGNER Acta Met.	1963	11	405
40.	C.M. ZENER Trans. AIME	1946	167	550
41.	H.G. BOWDEN and P.M. KELLY Acta Met.	1967	15	1439
42.	A.H. COTTRELL and B.A. BILBY Phil.Mag.	1951	42	573

		<u>Year</u>	<u>Volume</u>	<u>Page</u>
43.	A. STACEY Ph.D.Thesis. Sheffield Poly-technic.	1972		
44.	F.C. FRANK Phil.Mag.	1951	42	1041
45.	L.S. TOTH, T.R. CASS, S.P. RAVITZ and J. WASHBURN Phil Mag.	1964	9	607
46.	A. HOWIE and U. VALDRE Phil.Mag.	1964	8	1981
47.	P. GAUNT and J.W. CHRISTIAN Acta Met.	1959	7	529
48.	B.A. BILBY Phil.Mag.	1953	44	782
49.	W. BOLLMAN Phil Mag	1961	9	972
50.	J.A. VENABLES Phil Mag	1962	7	35
51.	C.H. WHITE and R.W.K. HONEYCOMBE JISI June	1962		457
52.	Z. NISHIYAMA and K. SHIMIZU "Journ.of Electron microscopy.	1963	12	28
53.	L.L. MARCH Tech.Rept.AFML. TR.	1965	65	161
54.	H. FUJITA and S. UEA Acta Met.	1972	20	759
55.	A.Z. SEEGER Z.Metall.	1956	47	653
56.	J.F. BREDDIS and W.D. ROBERTSON Acta Met.	1962	10	1071
57.	B. GINA Acta Met.	1958	6	748
58.	R.P. REED Acta Met.	1962	10	865
59.	J.F. BREDDIS Trans AIME	1964	230	1583
60.	A.J. GOLDMAN, W.A. ROBERTSON and DAROSS Trans AIME.	1964	230	240
61.	H. SCHUMANN Arch Eisenhütten	1967	38	347
62.	P.L. MANGONON and G. THOMAS Met Trans.	1970	1	1577
63.	P.L. MANGONON and G. THOMAS Met Trans.	1970	1	1587
64.	R.L. GRUNES, G. DANTONIO and K. MUKHERJEE. Met. Sci. Eng.	1972	9	1
65.	M.J. WHELAN Proc. Roy. Soc.	1959	249	114
66.	W. CHARNOCK and J. NUTTING Met. Sci. J.	1967	1	78
67.	W. CHARNOCK and J. NUTTING Met. Sci. J.	1967	1	123

		<u>Year</u>	<u>Volume</u>	<u>Page</u>
68.	E.R. PLETY (Ed) Martensite	1970		
69.	P.G. WINCHELL and M. COHEN Trans ASM	1962	55	347
70.	N. PETCH Phil Mag.	1957	2	649
71	R.L. FLEISCHER Acta Met.	1963	11	203
72.	G.R. SP. IGH and H. WARLIMONT	1963	206	385
73.	S.V. RADCLIFFE and M. SCHATZ - Nature	1963	200	161
74	R.S. SHKLAR Fiz. Met. Metalloved	1966	21	285
75.	L. KAUFMAN, M. COHEN Progress in Metal Physic.	1958	7	175
76.	R.D. JONES and S. KAPOOR J.I.S.I. March	1973		276
77.	L.S. YERSHOVA, J.N. BOGACHEV and R.S. SHKLYAR Fiz. Met. Metalloved.	1962	200	457
78.	J.G. PARR J.I.S.I.	1952	171	137
79.	V.F. YEGOLNY, I.N. BOGACHEV and R.S. SHKLYAR Fiz. Met. Metalloved.	1964	19/3	423
80.	R.T. HITCHCOKS and R.H. FORBES JONES Met. Transaction.	1974	5	847
81.	A. HOLDEN, J.P. BOLTON and H.R. PLETY JISI Sept.	1971		721
82.	W.P. REES, B.E. HOPKINS and H.R. TIPLER JISI.	1954	177	98
83.	F.M. WALTERS, J.R. KROEMER and B.M. LORING Trans AIME.	1942	150	401
84.	W. JOLLEY JISI Feb.	1968		170
85.	J. BOLTON Ph.D. thesis Sheffield Polytechnic	1968		
86.	A. HOLDEN M. Sc. Thesis Sheffield Polytechnic.	1970		
87.	M.J. ROBERTS and W.S. OWEN Trans AIME	1967	60	687
88.	H. SCHUMANN Neue Hutte Jan.	1970		12
89.	T. SUZUKI Bulletin of the Tokyo Inst. of Tech.	1967	82	91

	<u>Year</u>	<u>Volume</u>	<u>Page</u>
90. M.TANAKA, T. SUZUKI and M. YODOGAWA Bulletin of the Tokyo Inst.of Tech.	1967	82	79
91. S. FLOREN Met. Rev.No. 126	1968	13	115
92. K. DETERT Trans. A.S.M.	1966	59	262
93. S. FLOREN Trans A.S.M.	1964	57	38
94. S. FLOREN and G.R.SPEICH Trans A.S.M.	1964	57	714
95. B.R. BANERJEE and J.J.HAUSER Climax. Molybdenum "Transformation and Harden- ability in steels".	1967		133
96. B.R. BANERJEE ET AL. Metal Science Journal	1968	2	76
97. S. FLOREN Trans AIME.	1964	230	842
98. H. CONRAD Trans ASM	1966	59	262
99. W.R. PATTERSON and L.S. RICHARDSON Trans A.S.M.	1966	59	71
100. A.J. GOLDMAN and JI MANEC. Trans A.S.M.	1965	58	645
101. D.T. PETERS and R. CUPP Trans AIME	1966	236	1420
102. A. HARDY and E. HEAL Prog.Metal.Phys.	1954	5	143
103. S. FLOREN Met. Rev.No.119	1965		115
104. N.P. ALLEN and C.C.BARLEY J.I.S.I.Dec.	1950		281
105. D.T. PETERS Trans A.S.M.	1968	61	62
106. C.A. STUBBINGTON and A. WIRTH J.I.S.I. July.	1972		506
107. R.C. HALL J.I.S.I.	1969	207	1310
108. NAMBU and F. DABOSI Cobalt Sept.	1972	57	192
109. R. HADFIELD JISI	1927	115	297
110. A.S. NICOCHENKO Physics of Metals and Metall.	1963	16	122
111. T. BONISZEWSKI ISI Spec.Rept.No.33	1965		69
112. J.M. CAPUS and G. MAYER Metallurgia.	1960	62	133
113. M.J.DICKSON J.Appl.Cryst.	1969	2	176

		<u>Year</u>	<u>Volume</u>	<u>Page</u>
114.	R.B. YAO Trans AIME August	1963	227	384
115.	A. TEKIN and A. WIRTH Unpublished research.	1975		
116.	T. SUZUKI Transactions I.S.I.Japan	1974	14	69
117.	M.HASSEN and K.ANDERKO Binary alloy systems Mc.Graw Hill NY.	1958		
118.	E.A.OWEN and Y.H.LIU J.I.S.I. Oct.	1949	163	132
119.	B.A. BILBY and J.W. CHRISTIAN Inst. of metals. Monograph and Report Series.	1955	18	121
120.	L. KAUFMAN and M.COHN Trans AIME - Journ.of Metal.Oct.	1950		1393
121.	A.F. ACTON and M.R.MEVIS Mater.Sci.Eng.	1970	5	19
122.	N.H.D. ROSS and A.G. CROCKER Acta,Met.	1970	18	405
123.	A. WIRTH and J. BICKERSTAFFE Met. Transactions.	1974	5	799
124.	C.A. DAMBILLO and H.W. PAXTON Met. Transactions. Nov.	1972	3	2895
125.	D.R. SQUIRES PhD thesis Sheffield Polytechnic.	1972		
126.	F.B. PICKERING Personnel Communication			
127.	A.J. BAKER and P.R. SWANN Trans ASM	1964	57	1008
128.	G.P.MILLER and W.I. MITCHELL J.I.S.I.	1965	205	899
129.	E. HONBOGEN and W.A. MAYER Z.METALKUNDE	1967	58	297
130.	P.L.GRUZIN and V.V.MURAL Phys.Metals and Met.	1967	3	384
131.	J.M. CAUC A.S.T.M. STP No.	1968	407	127

Fig. 1 Equilibrium phase diagram for Fe-Mn.

Fig. 2. Transformation character-  
(61)  
istics of Fe-Mn alloys.

Fig.3. Transformation cha  
aracteristics of Fe-Ni  
(118)  
alloys.

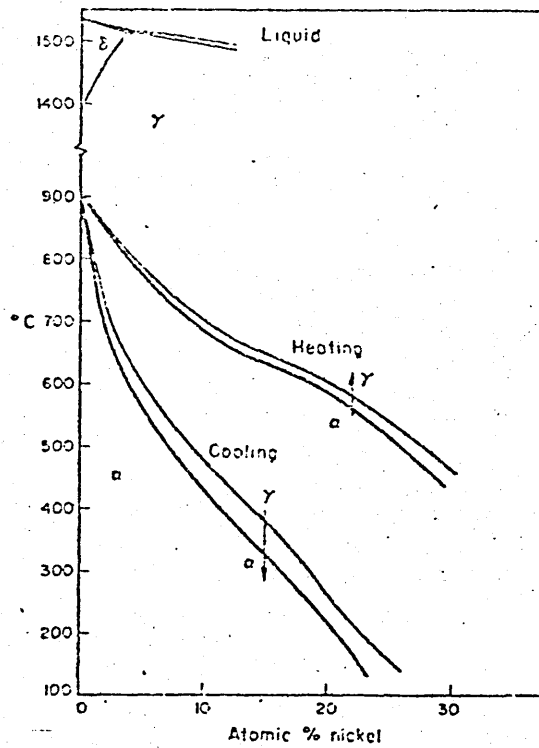
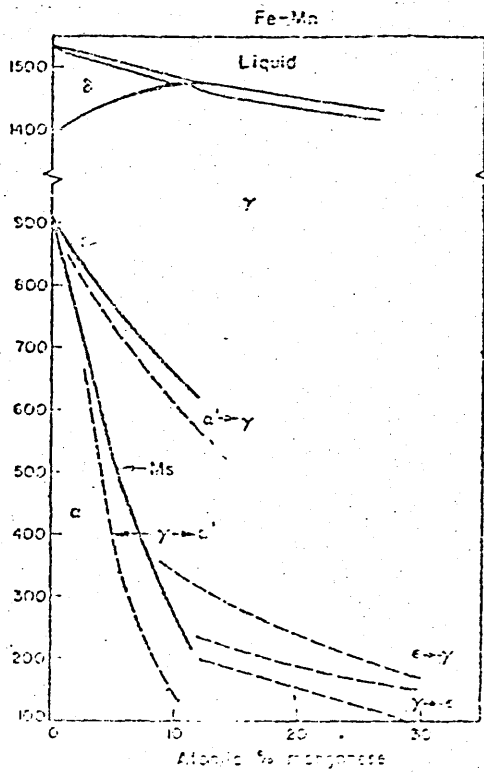
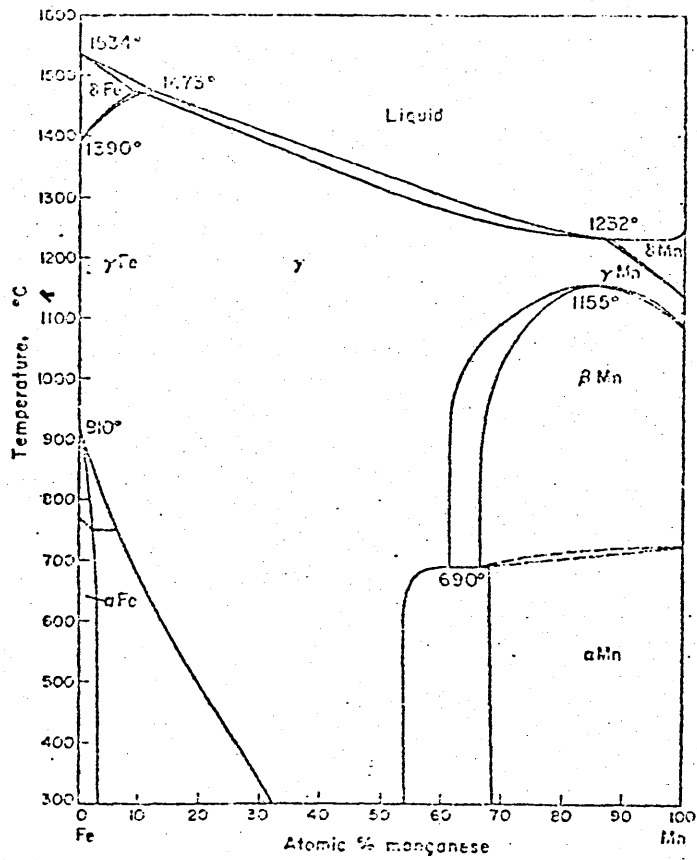


Fig.4 The crystallographic features of a martensitic reaction:  
(a) the original lattice, (b) the lattice after a homogenous shear, (c) slip plus zero lattice deformation giving the same shape change as in (b), (d) lattice deformation plus slip giving zero shape change, (e) lattice deformation plus uniform twinning giving zero shape change, (f) lattice deformation plus non-uniform twinning giving a finite shape change. (After Bilby and Christian.)

(119)

Fig. 5. The shape deformation produced by a martensite plate.

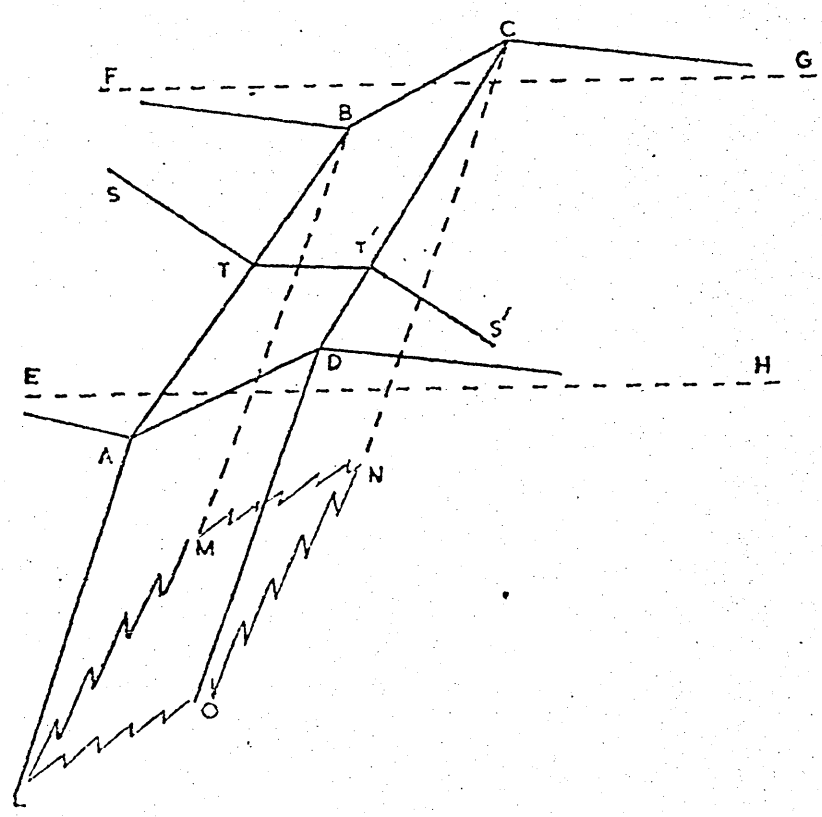
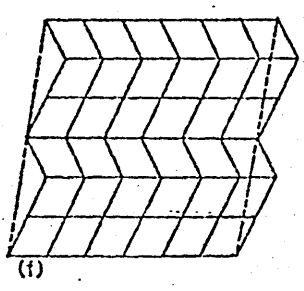
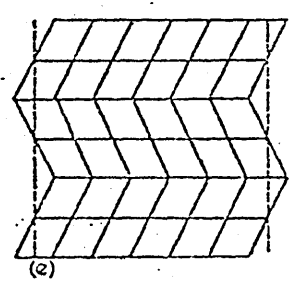
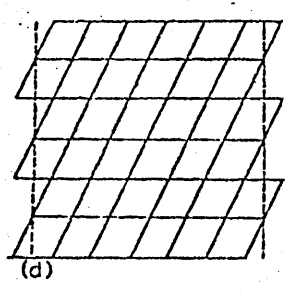
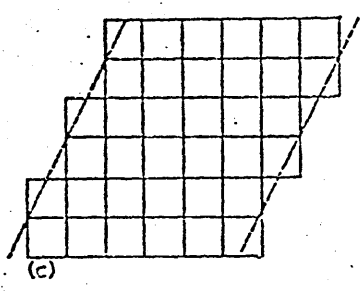
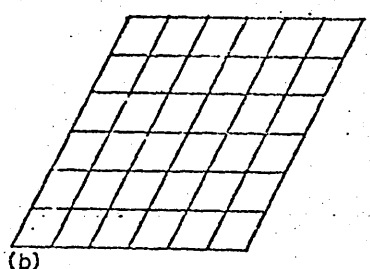
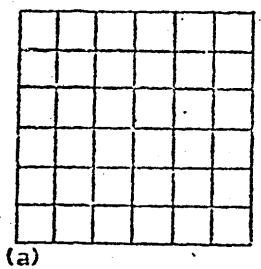


Fig.6 The lattice correspondence for martensite formation in steels ( $a_0$  is the austenite lattice parameter and the martensite parameters are 'a' and 'c'). (5)

Fig.7 Extended partial dislocation node where R is the radius of curvature of the node and W is the node width.

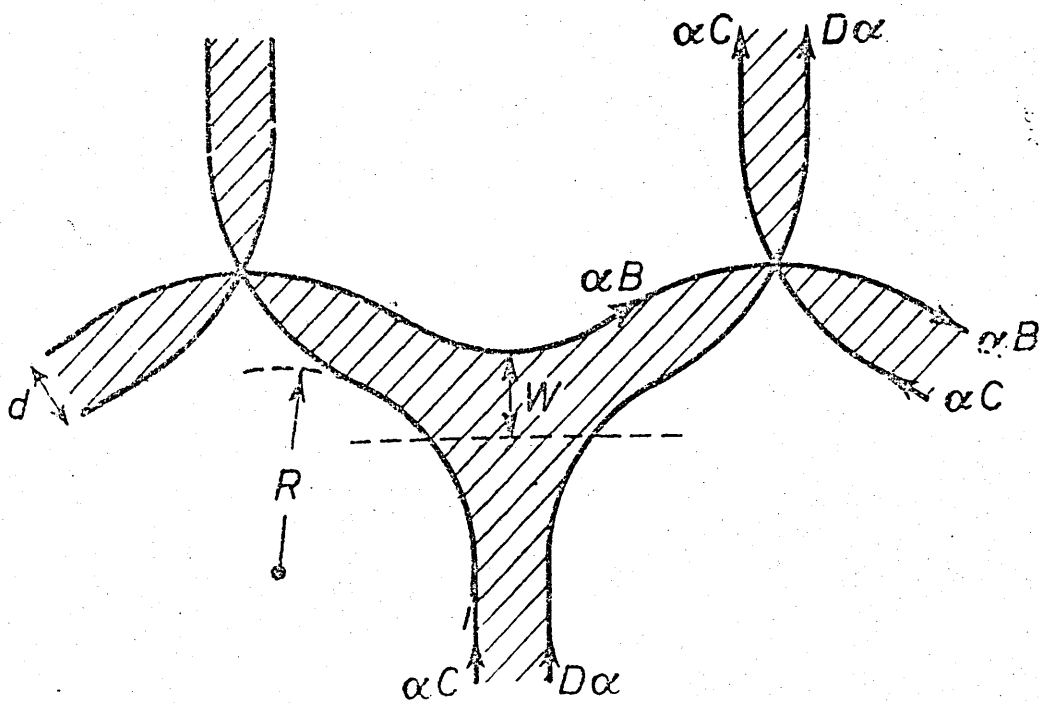
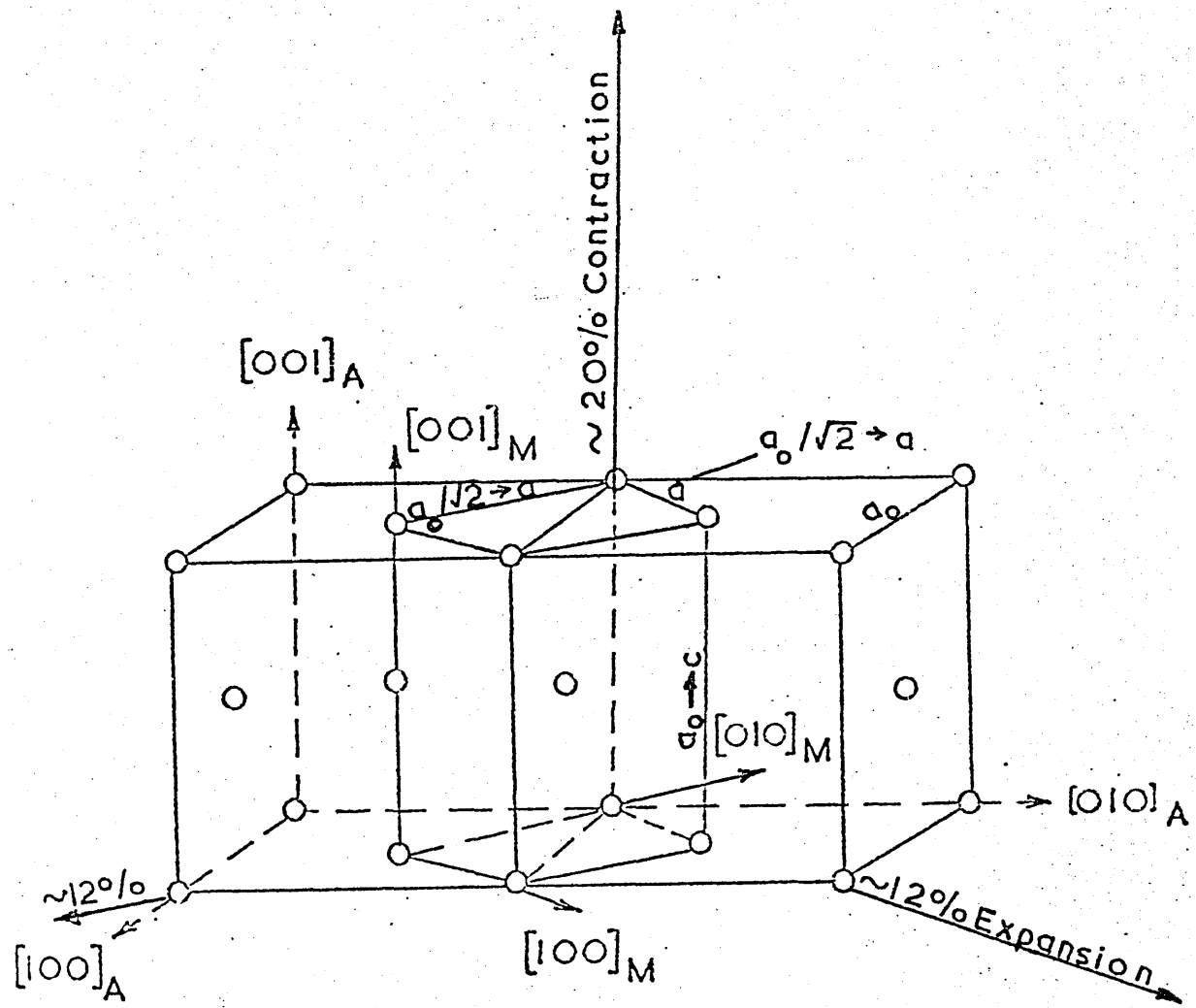


Fig. 6 Lincoln Dilatometer

1. Transducer ferrite core
2. Transducer casing
3. Cooling flange
4. Support
5. Piston fine adjustment
6. Piston coarse adjustment
7. Gage fixing screw
8. Piston support
9. Inert gas inlet
10. Gas flow tube
11. Quartz pistons
12. Quartz sample holder tube
13. Sample
14. Thermocouple
15. Quartz protection tube
16. Vacuum flange and gas outlet
17. Furnace

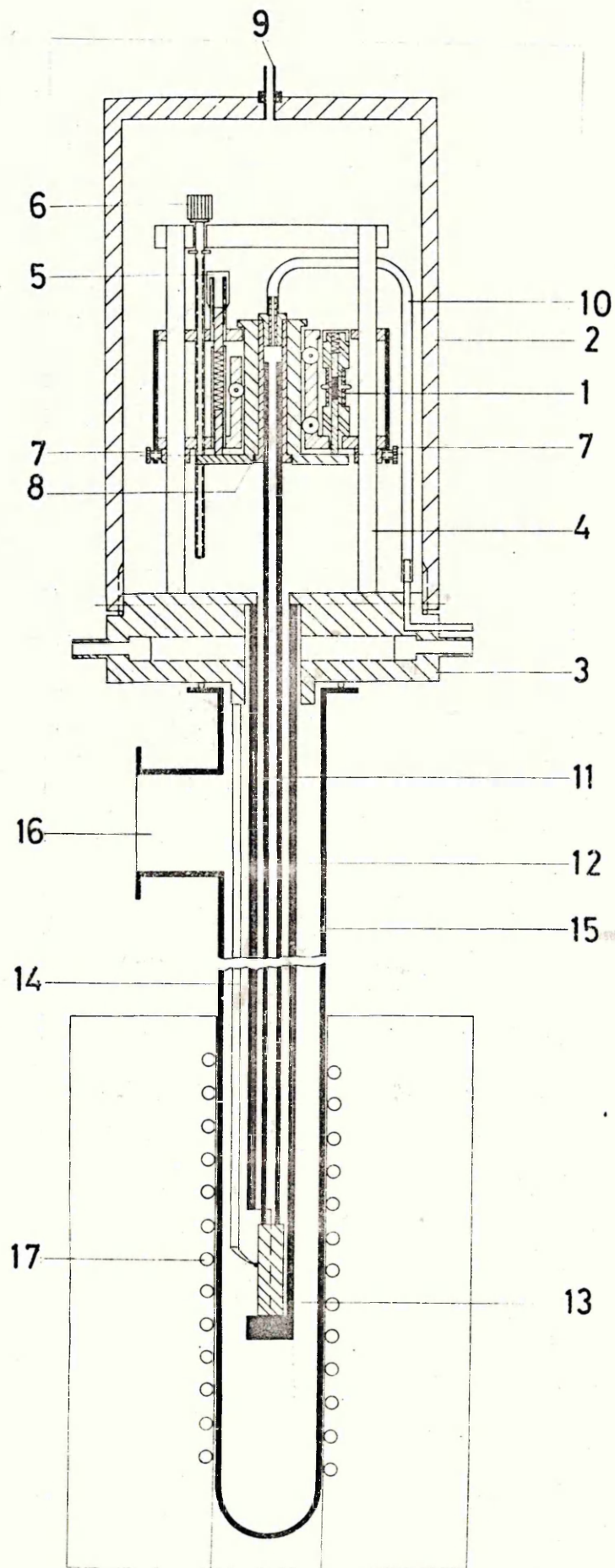


Fig.9 A schematic representation of the growth of martensite  
(58)  
from austenite on a  $(225)_\gamma$  habit plane by Reed.

Fig.10. Phase diagram for Fe-Mn-Co at room temperature  
(from Cobalt Monograph)

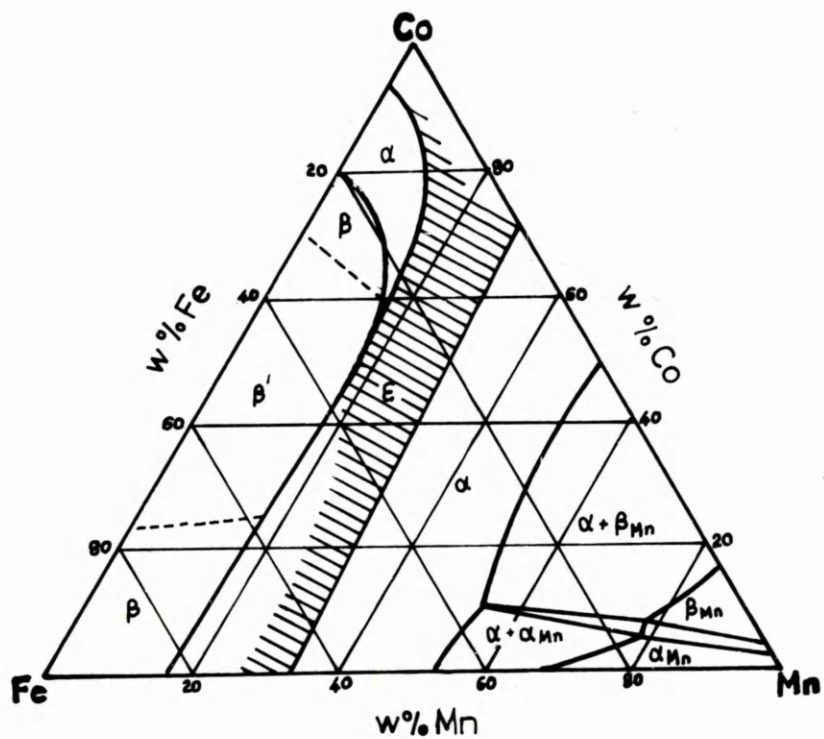
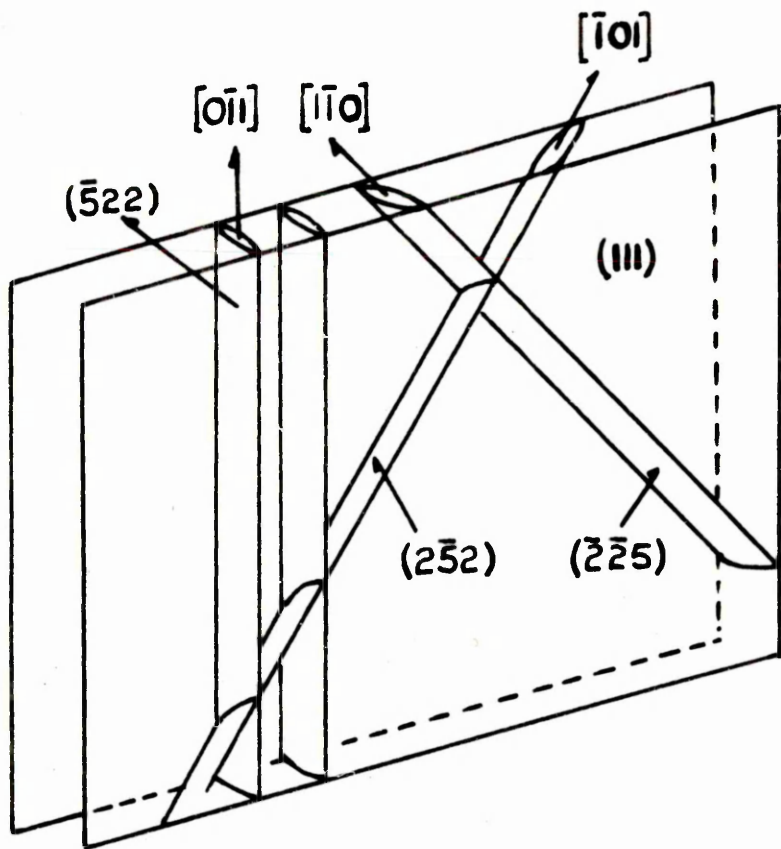


Fig. 11 Optical microstructure of alloy K<sub>7</sub> water quenched, showing  
 $\alpha$  martensite (dark),  $\epsilon$  martensite (white) and austenite  
(grey). Mag X800

Fig. 12 As above Magx800

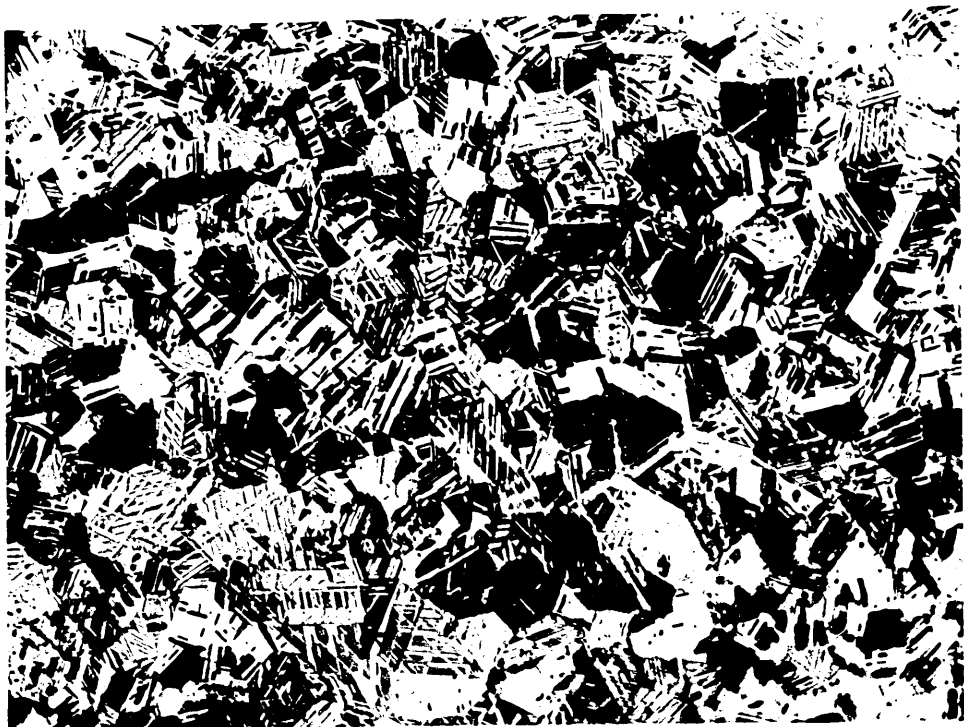


Fig. 13 Optical microstructure of alloy K<sub>6</sub> water quenched, showing  
α martensite (dark) ε martensite (white) and austenite  
(grey). Mag 1800.

Fig. 14 Optical microstructure of alloy K<sub>5</sub> water quenched, showing  
α martensite (dark), ε martensite (white and austenite (gr  
Mag 2100.

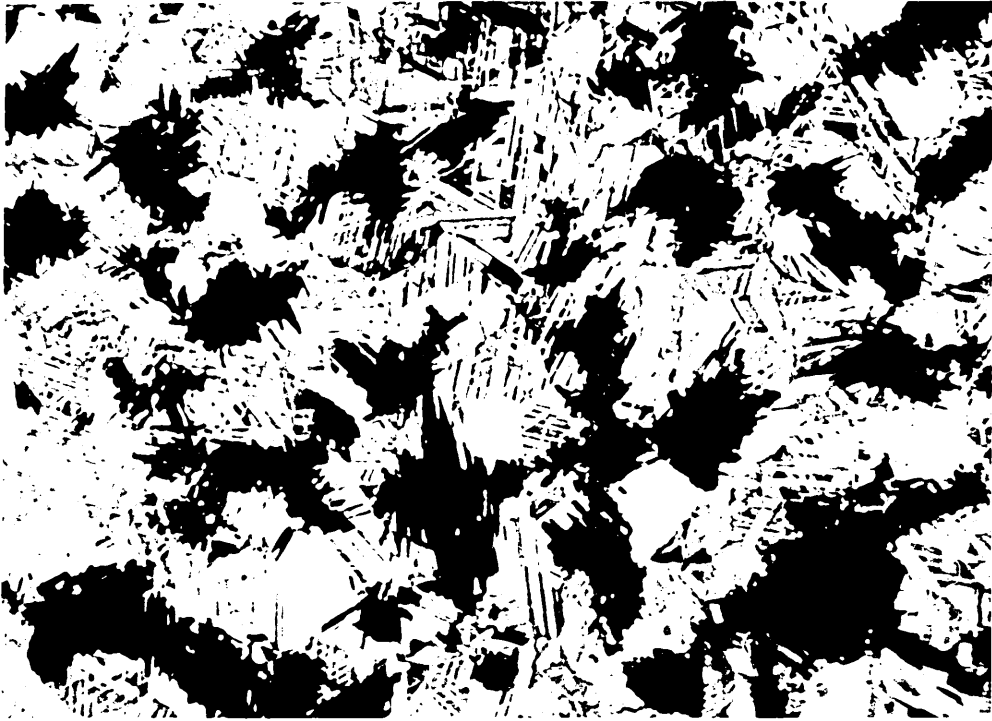


Fig.15 Electron micrograph of alloy K8 water quenched, showing  
dislocated  $\epsilon$  martensite bands containing  $\alpha$  martensite.  
Mag  $\times$  60,000.



Fig.16 Electron micrograph of alloy K9 water quenched, showing twin related  $\alpha'$ (bcc) martensite laths (dark) ( $\alpha'_1 \rightarrow \alpha'_7$ ) lying inside  $\epsilon$  martensite (grey). Mag X100,000

Fig.17 Electron diffraction pattern showing Kurdjumov-Sachs orientation relationship between fcc, cph and bcc phases.

Fig.18 Diffraction pattern of (011)  $\epsilon$  and Dark field of Fig.16 using  $(200)_{\alpha'}$  reflection, showing twin related  $\alpha'$  martensite laths. Mag X100,000

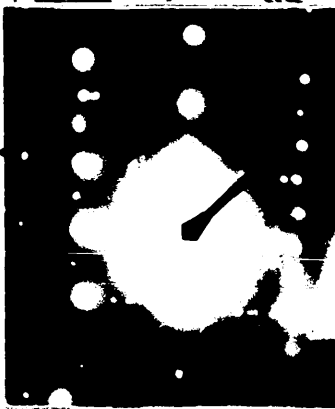
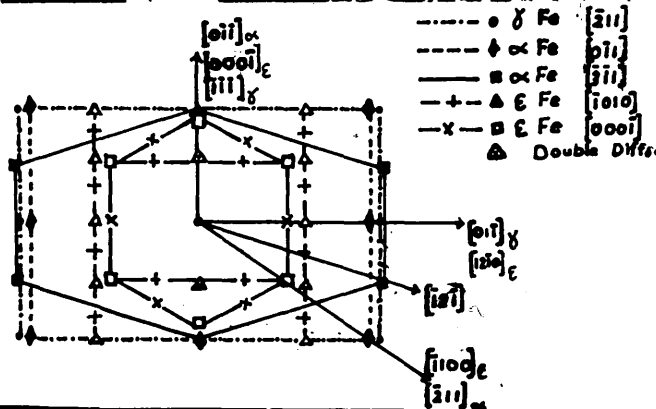


Fig.19 Electron micrograph of alloy #7 water quenched showing parallel  $\alpha'$  martensite laths in the  $\epsilon$  martensite. Mag X1000

Fig.20 Electron diffraction pattern of  $(110)_{\alpha'}$ .

Fig.21 Electron diffraction pattern of  $(120)_{\epsilon}$ .

Fig.22 Dark field of Fig.19 using  $(112)_{\alpha'}$  reflection.

Fig.23 Dark field of Fig.19 using  $(10\cdot1)_{\epsilon}$  reflection.

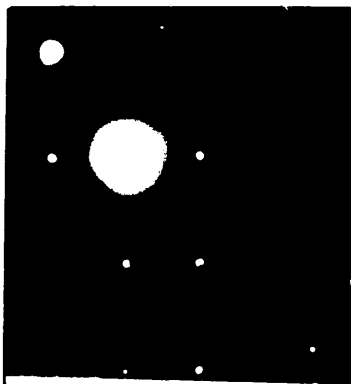
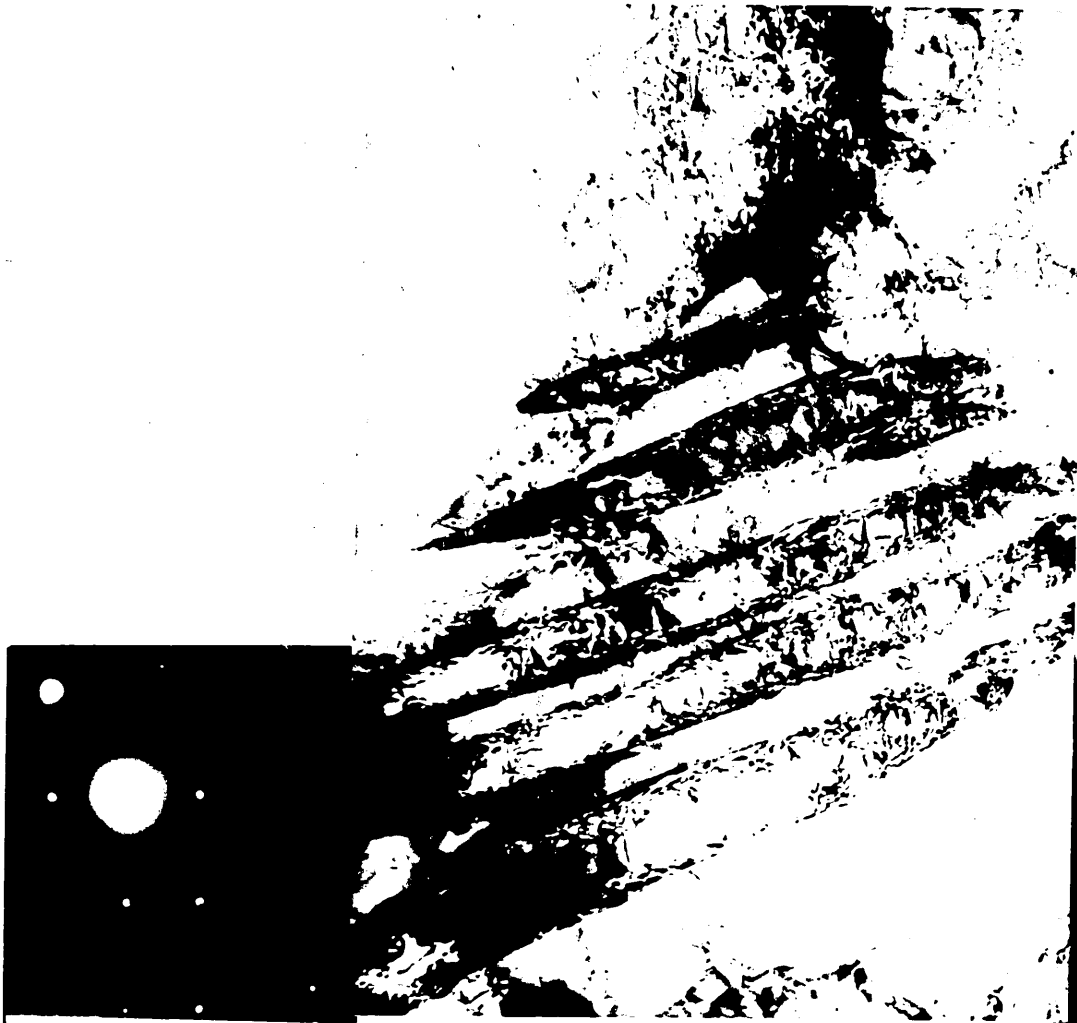


Fig. 24 Electron micrograph of alloy K<sub>7</sub> water quenched showing overlapping stacking faults and/or thin  $\epsilon$  bands. Mag X50.00

Fig. 25 Dark field image from same area as above.

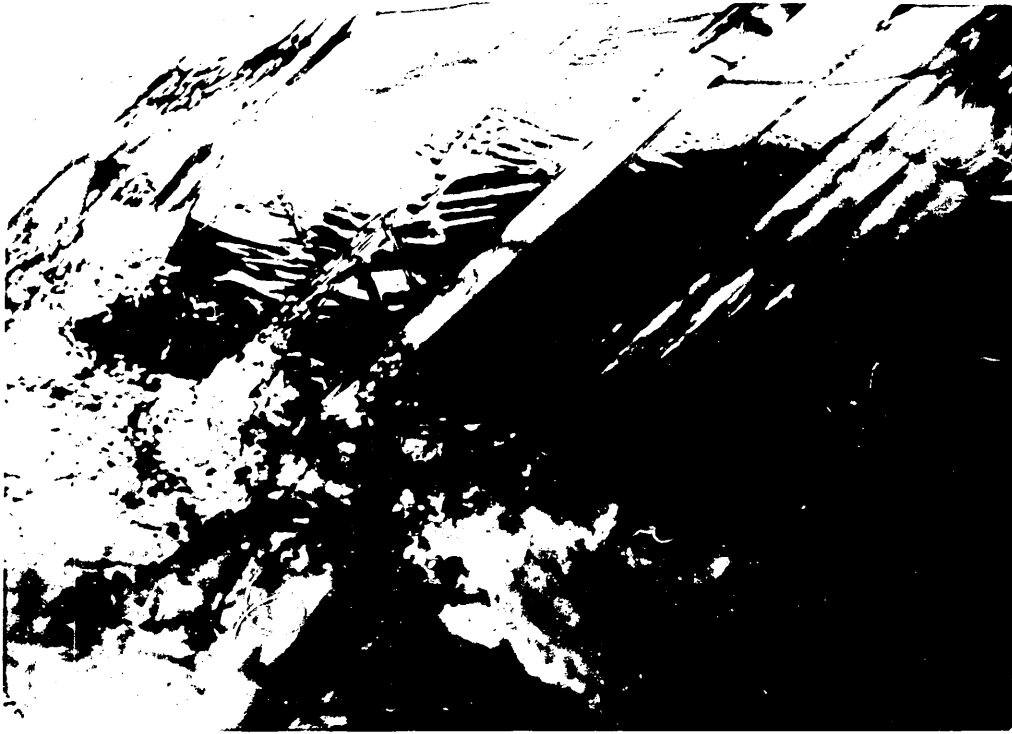


Fig. 26 Effect of ageing time on the hardness of alloys K2 → K7  
at 225°C.

Fig. 27 Effect of ageing time on the hardness of alloys K2 → K7  
at 375°C.

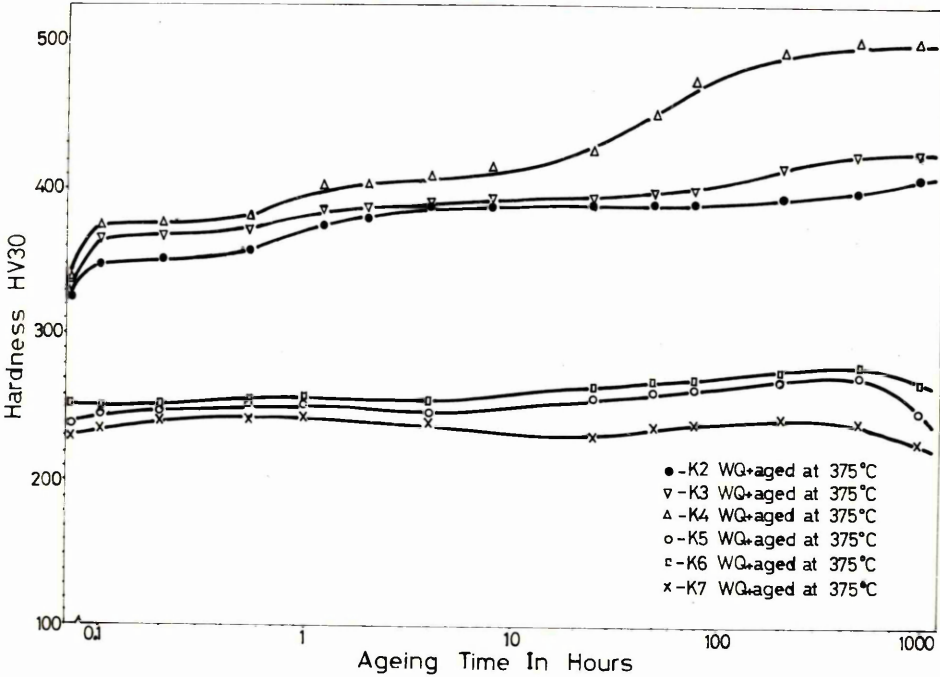
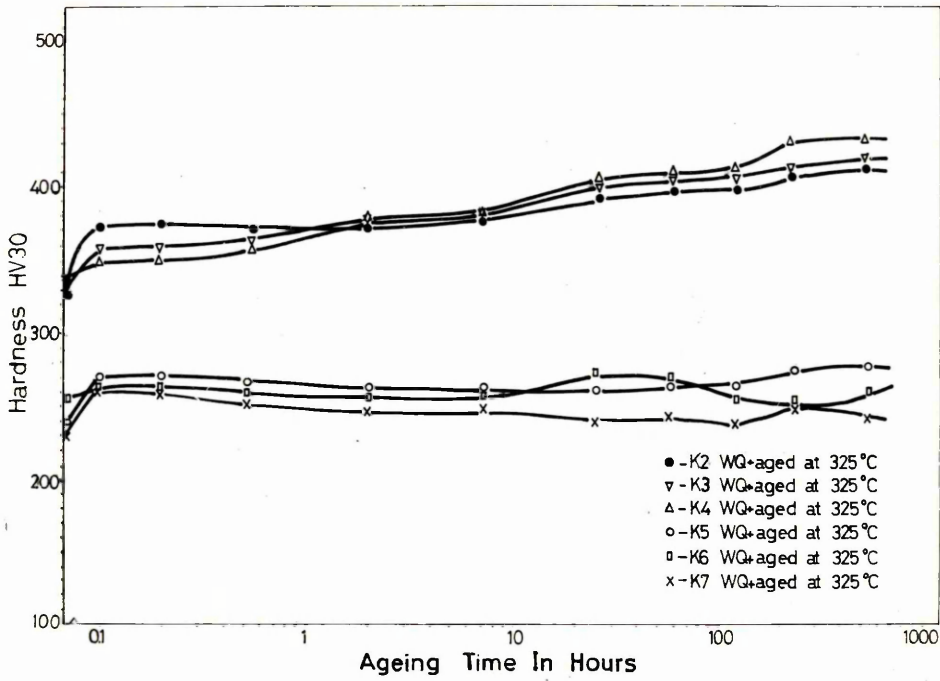


Fig.28 Effect of ageing time on the hardness of alloys K2 → K7  
at 425°C.

Fig.29 Effect of ageing time on the hardness of alloys K2 → K7  
at 450°C.

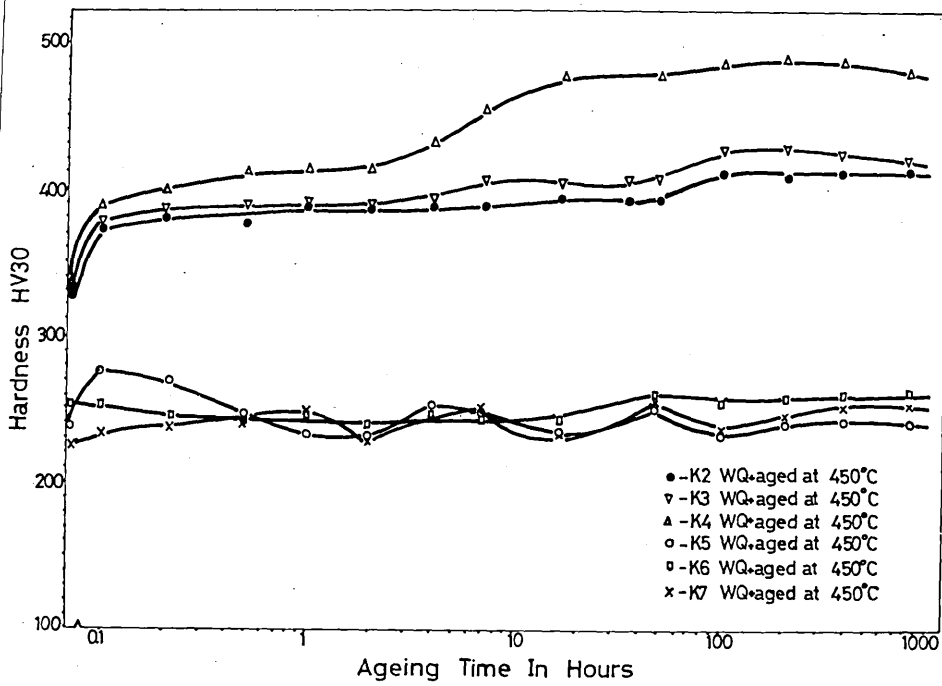
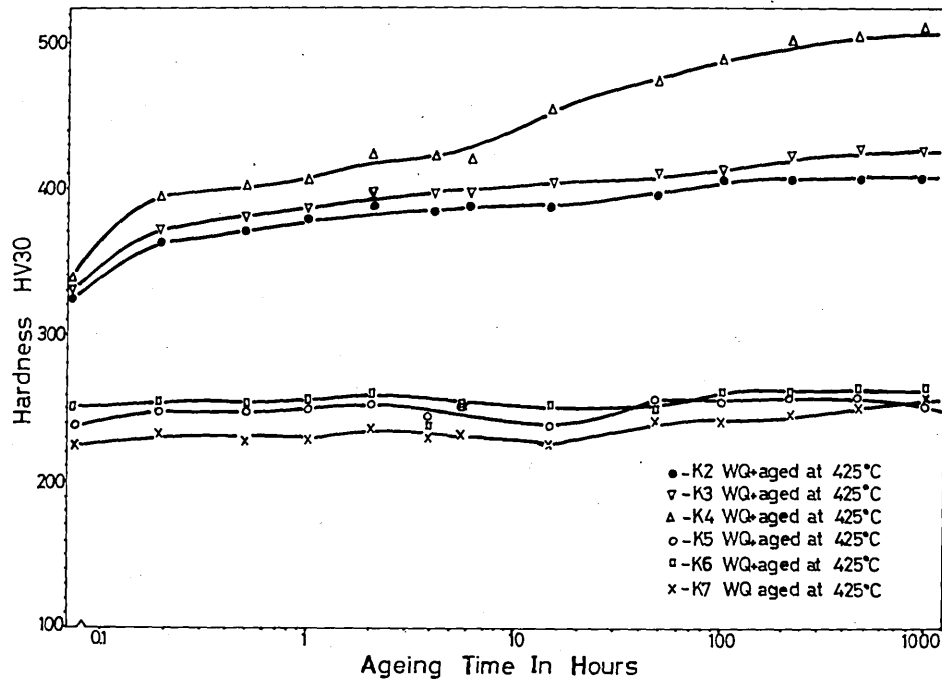


Fig. 30 Effect of ageing time on the hardness of alloys K2 → K7  
at 475°C.

Fig. 31 Effect of ageing time on the hardness of alloys K2 → K7  
at 525°C.

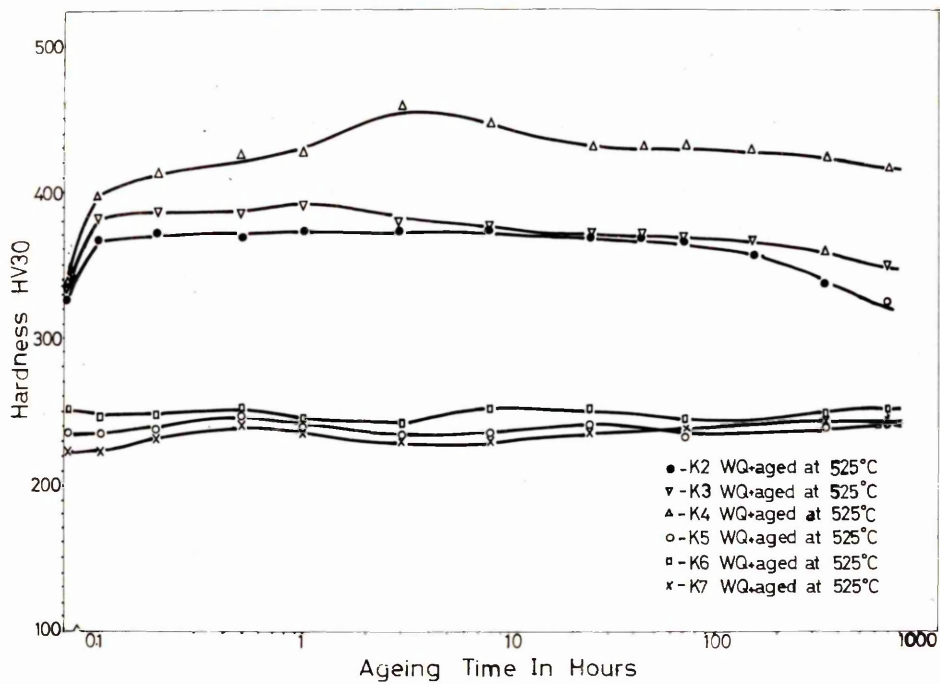
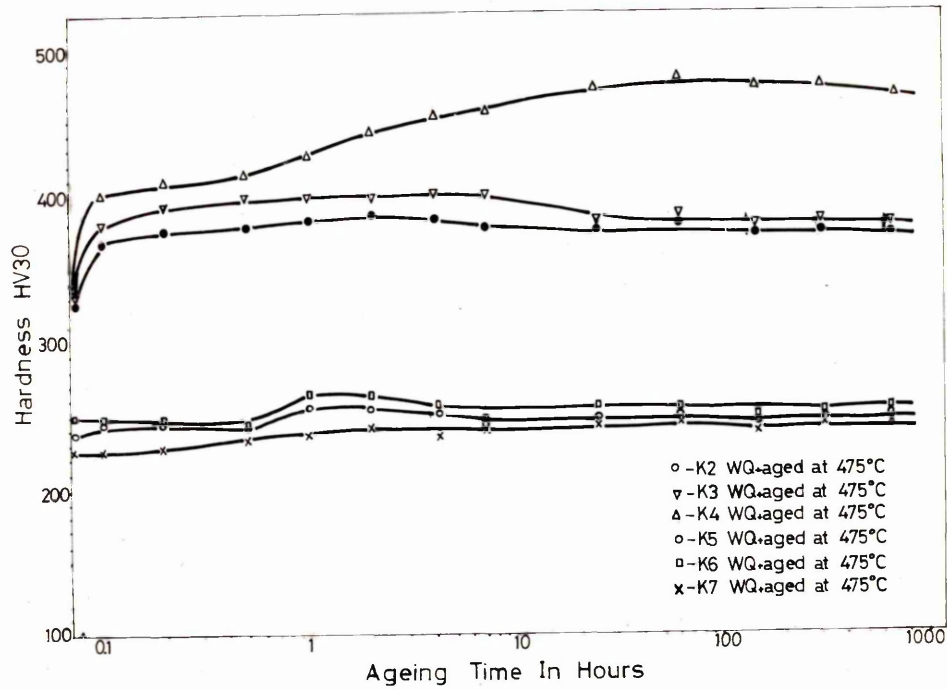


Fig. 32 Effect of ageing time on the hardness of alloys K2 → K7  
at 550°C.

Fig. 33 Effect of ageing time on the hardness of alloys K2 → K7  
at 600°C.

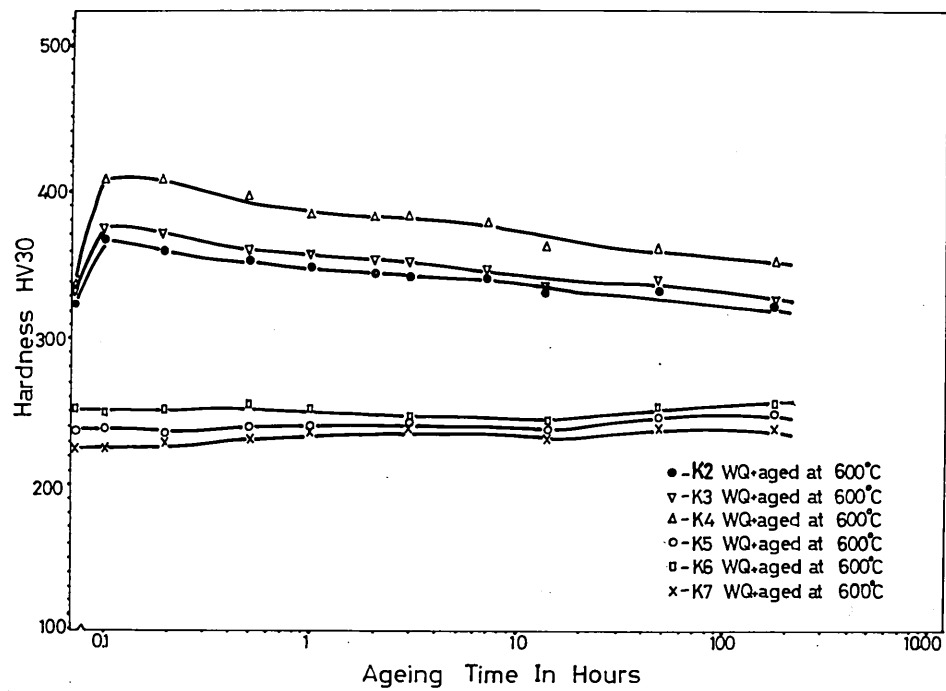
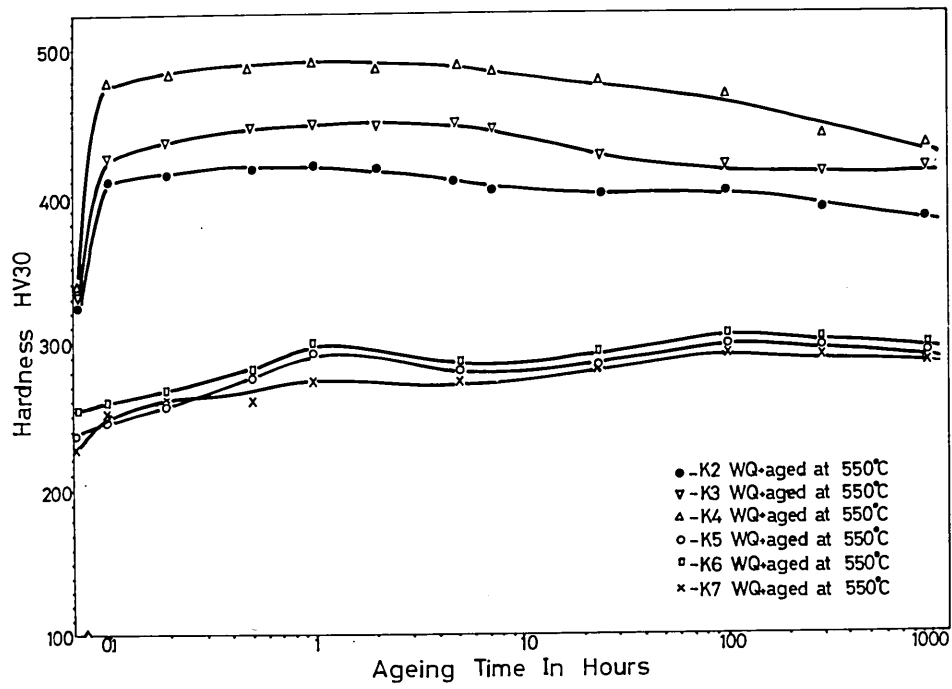


Fig. 34 Optical microstructure of alloy K3 water quenched and aged for 2 hours at 550°C showing  $\alpha$  martensite (dark)  $\beta$  martensite (white) and austenite (grey). Mag X1300

Fig. 35 Optical microstructure of alloy K7 water quenched and aged for 960 hours at 425°C, showing equiaxed austenite grains. Mag X800.

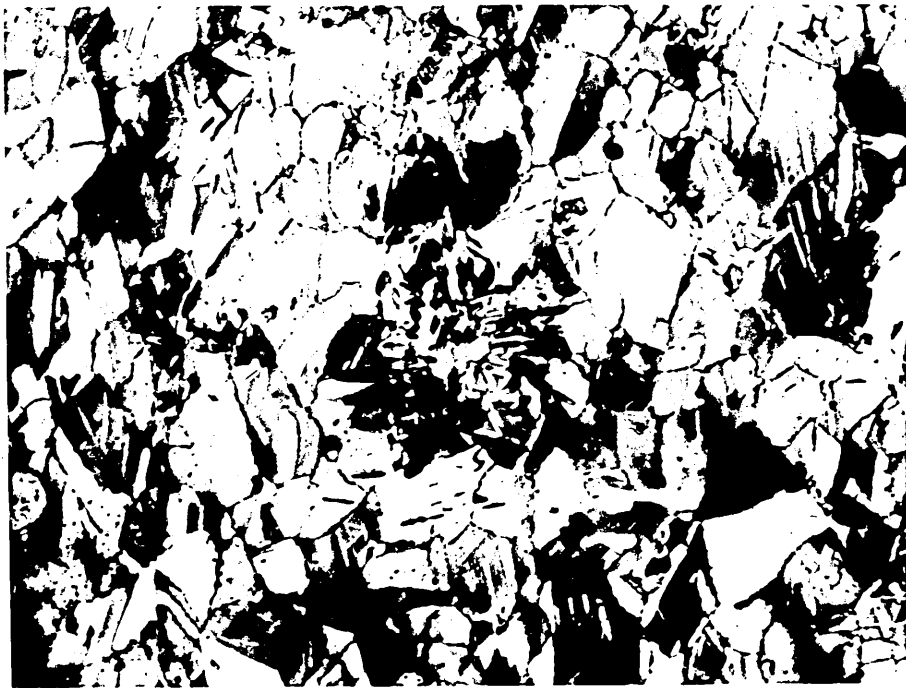


Fig. 26 Optical microstructure of alloy K7 water quenched and aged for 2 hours at 425°C, showing  $\alpha$  martensite (blue),  $\epsilon$  martensite (pale yellow) and austenite (brown).  
Mag X 2,800.

Fig. 37 Effect of ageing temperature on the matrix structure of alloy #2 water quenched. (ageing time 2 hours).

Fig. 38 Effect of ageing temperature on the matrix structure of alloy #3 water quenched. (ageing time 2 hours).

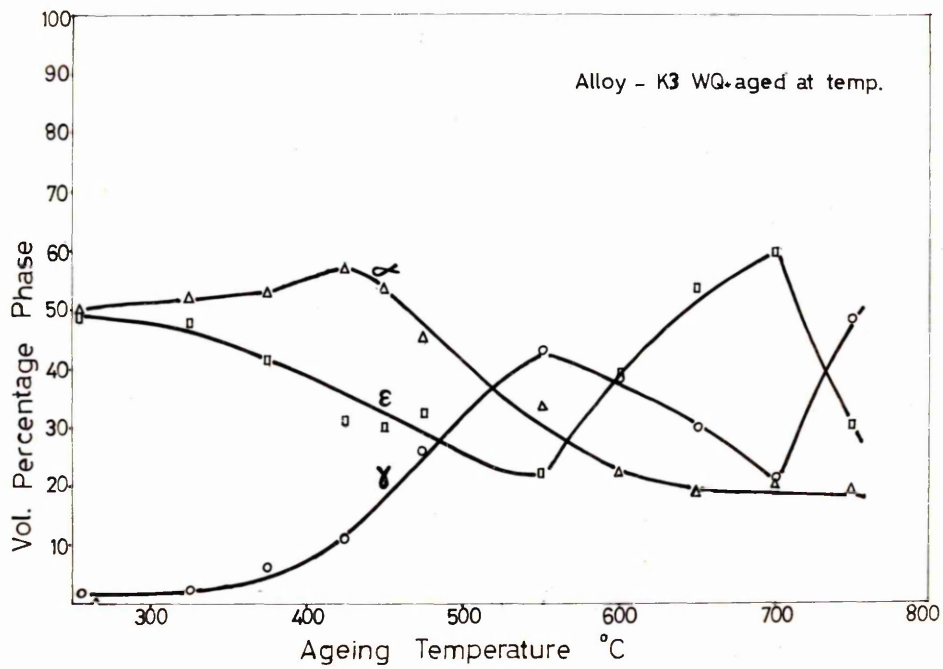
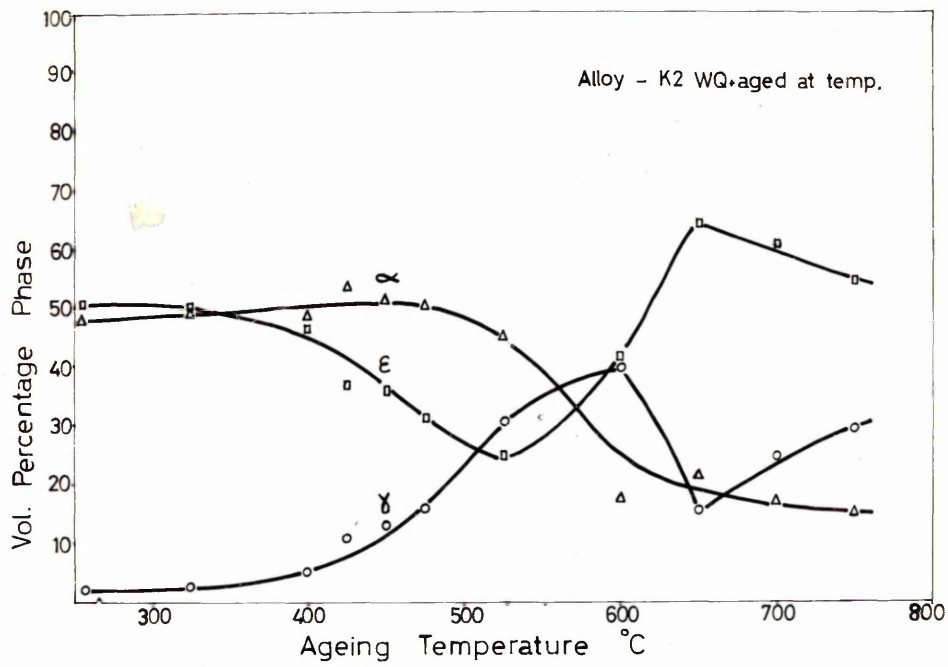


Fig.39 Effect of ageing temperature on the matrix structure of alloy E4 water quenched (ageing time 2 hours).

Fig.40 Effect of ageing temperature on the matrix structure of alloy E5 water quenched (ageing time 2 hours).

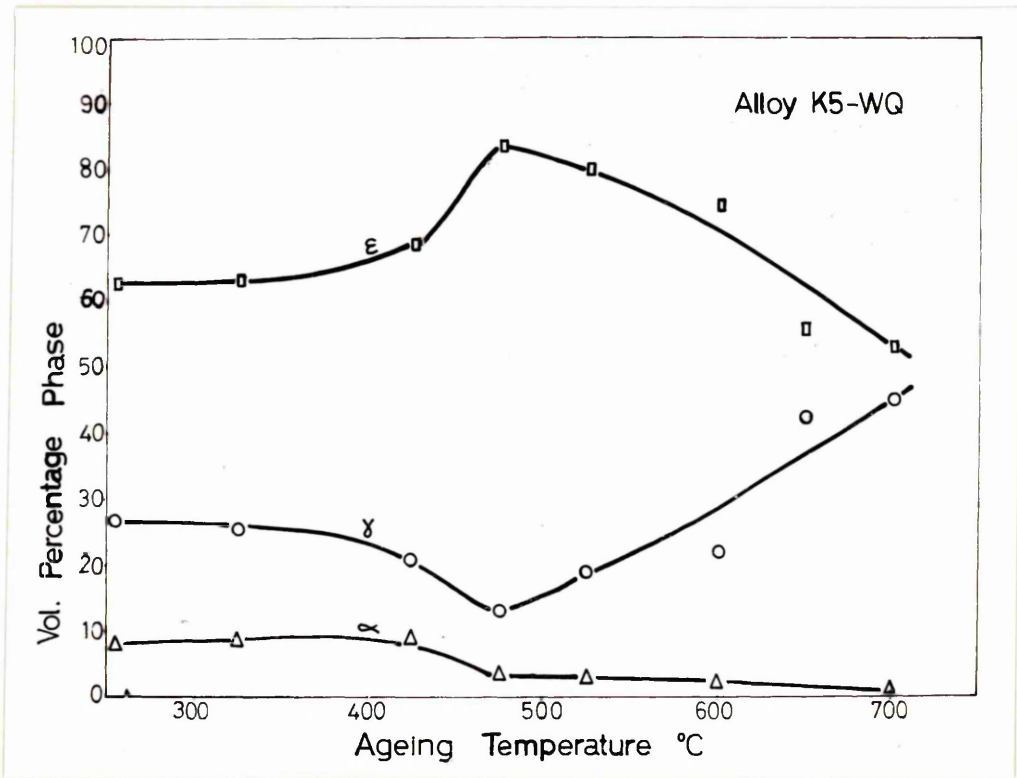
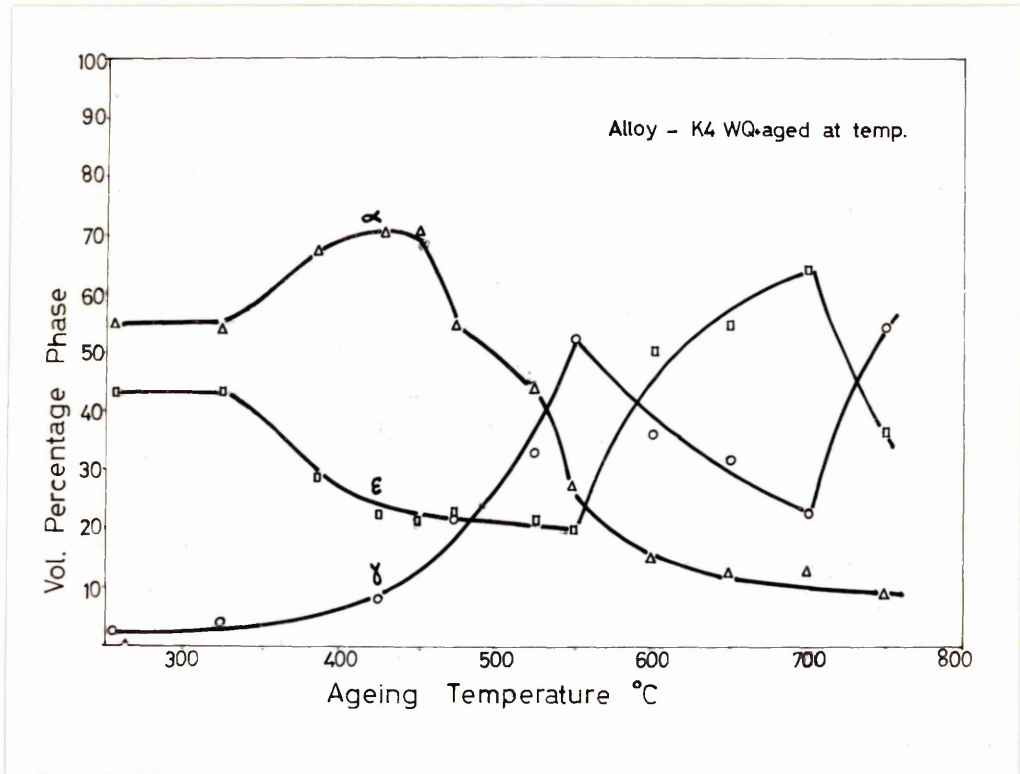
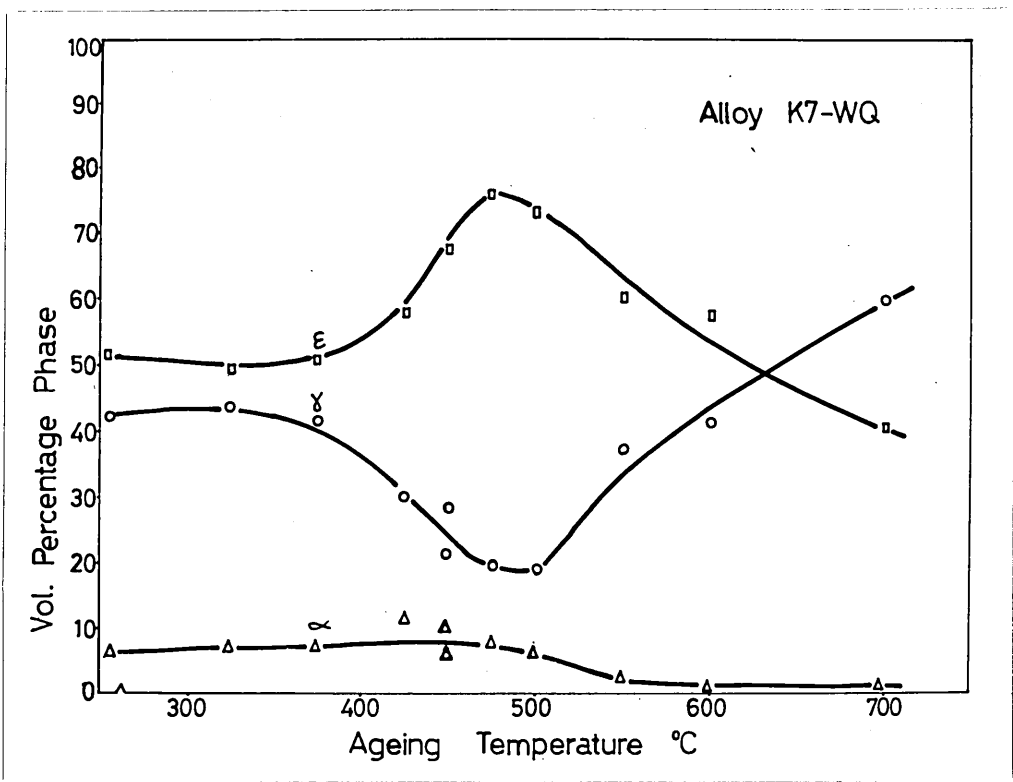
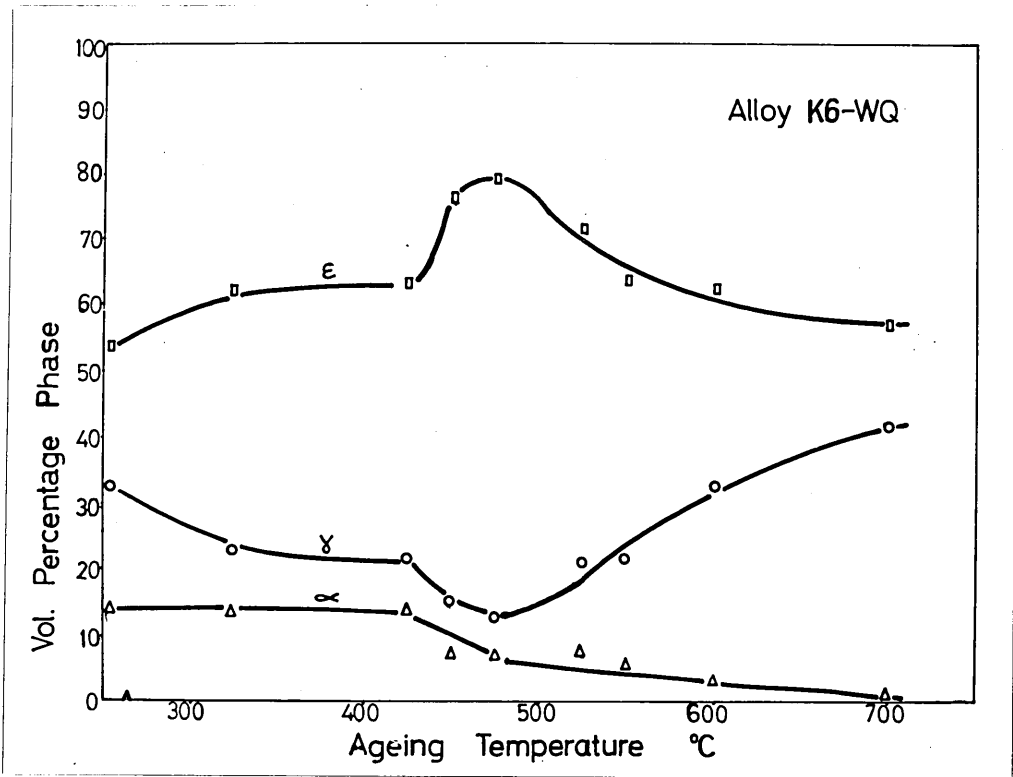


Figure 41 Effect of ageing time on the matrix structure of alloy #6 water quenched (ageing time 2 hours).

Fig.42 Effect of ageing time on the matrix structure of alloy #7 water quenched (ageing time 2 hours).



Volume per (200) data?

Fig.43 Electron micrograph of alloy K4 water quenched and aged for 2 hours at 550<sup>o</sup>C, showing fine precipitates, martensite laths ( $\alpha'$  and  $\epsilon$ ) and reverted austenite. Mag X100,000.

Fig.44 Electron micrograph of alloy K4 water quenched and aged 2 hours at 425<sup>o</sup>C showing fine precipitates. Mag X100,000

Fig.45 Electron micrograph of alloy K4 water quenched and aged for 2 hours at 425<sup>o</sup>C showing lath structure. Mag X100,000

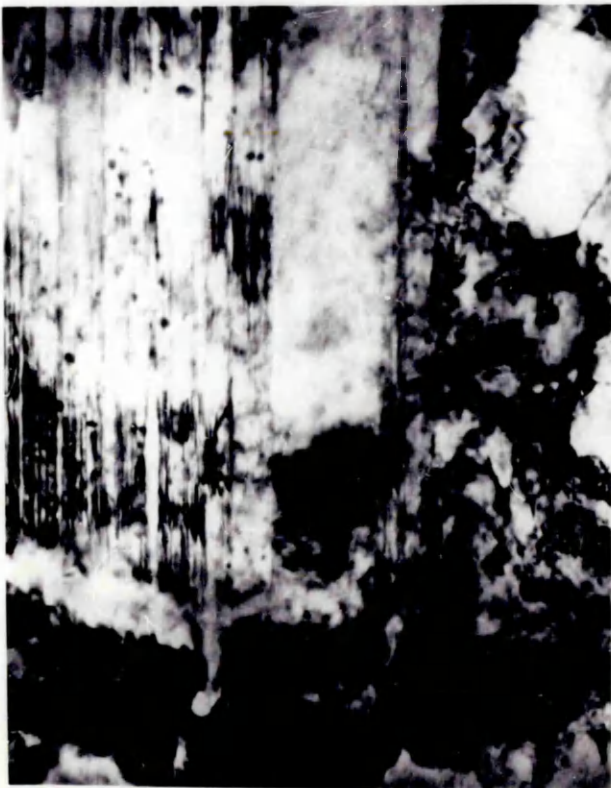
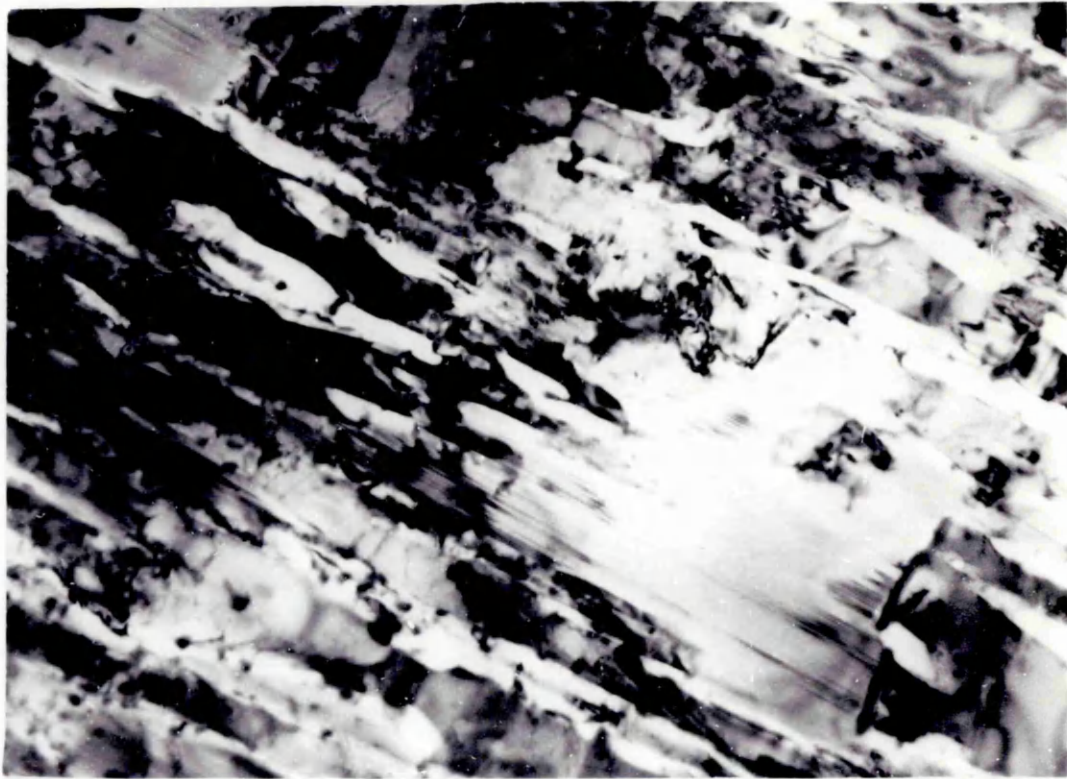


Fig.46 Electron micrograph of alloy K4 water quenched and aged  
for 2 hours at 425<sup>o</sup>C, showing finely dispersed precipitate  
Mag. 1100.000

Fig.47 Electron diffraction pattern showing both precipitate and  
matrix zones.

Fig.48 Dark field image from same area as above.

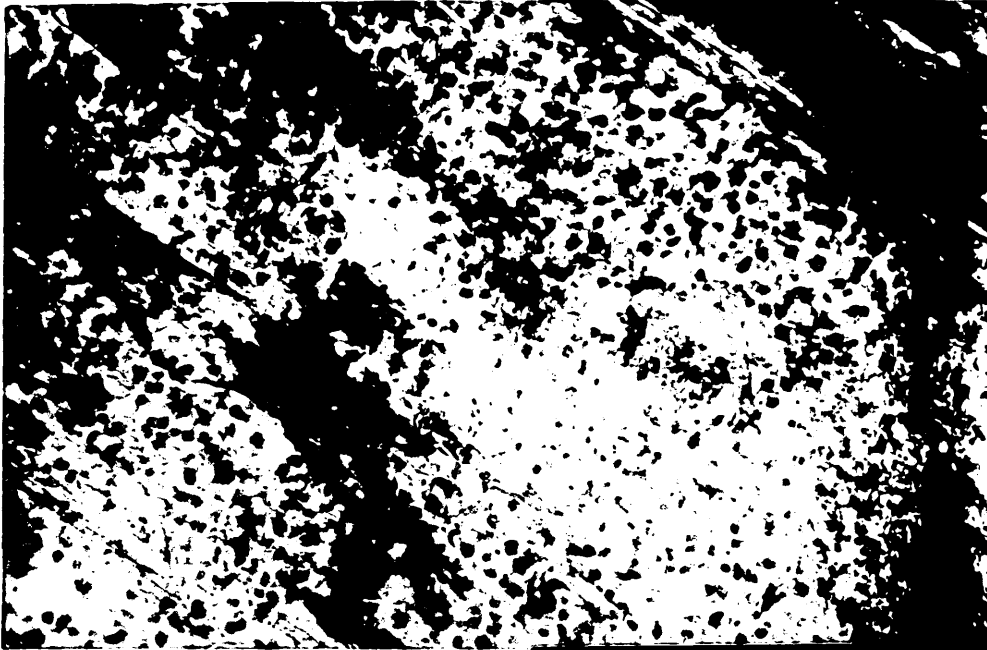
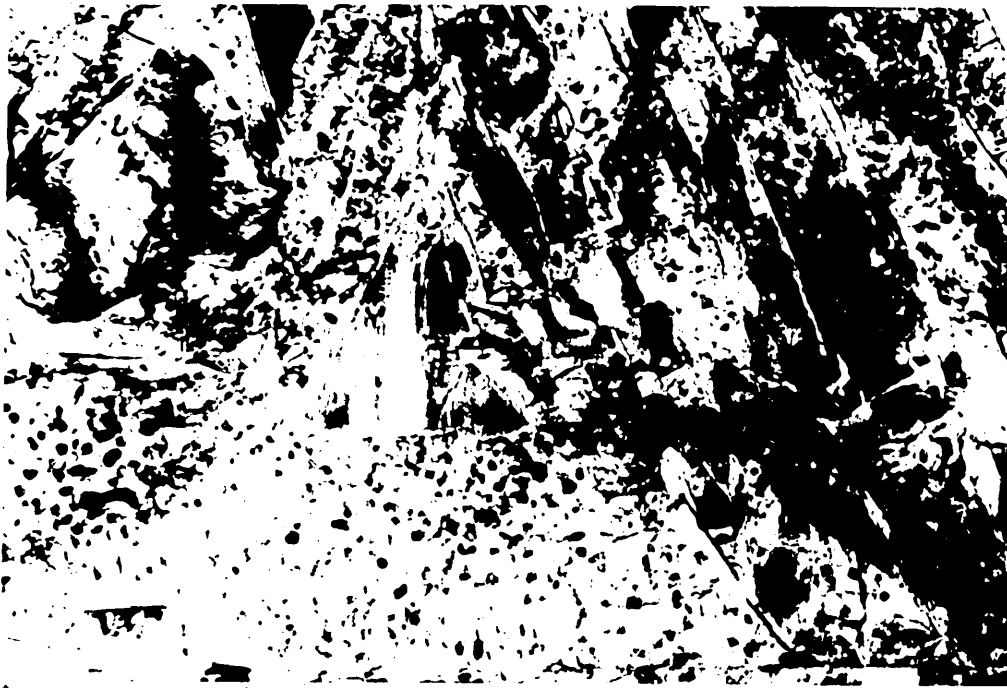


Fig.49 Electron micrograph of alloy E4 water quenched and aged 7 hours at 475°C showing  $\delta$ -phase precipitate ( $\delta_A$ ), finely dispersed precipitate and reverted austenite ( $\Lambda$ ).  
Mag x 100000

Fig.50 Electron diffraction pattern showing  $\langle 110 \rangle_{\delta}$  ,  $\langle 21\bar{1}0 \rangle_E$  and  $\langle 100 \rangle_A$  zones.

Fig.51 Dark field image of Fig.49 using (111) reflection and also precipitate reflection, showing  $\delta$ -phase precipitate and fine precipitates within the laths.  
Mag x 100000



- × -  $\langle 110 \rangle_{\delta}$
- -  $\langle 21\bar{1}0 \rangle_{\epsilon}$
- - DOUBLE DIFFRACTION
- + -  $\langle 100 \rangle_{\alpha}$

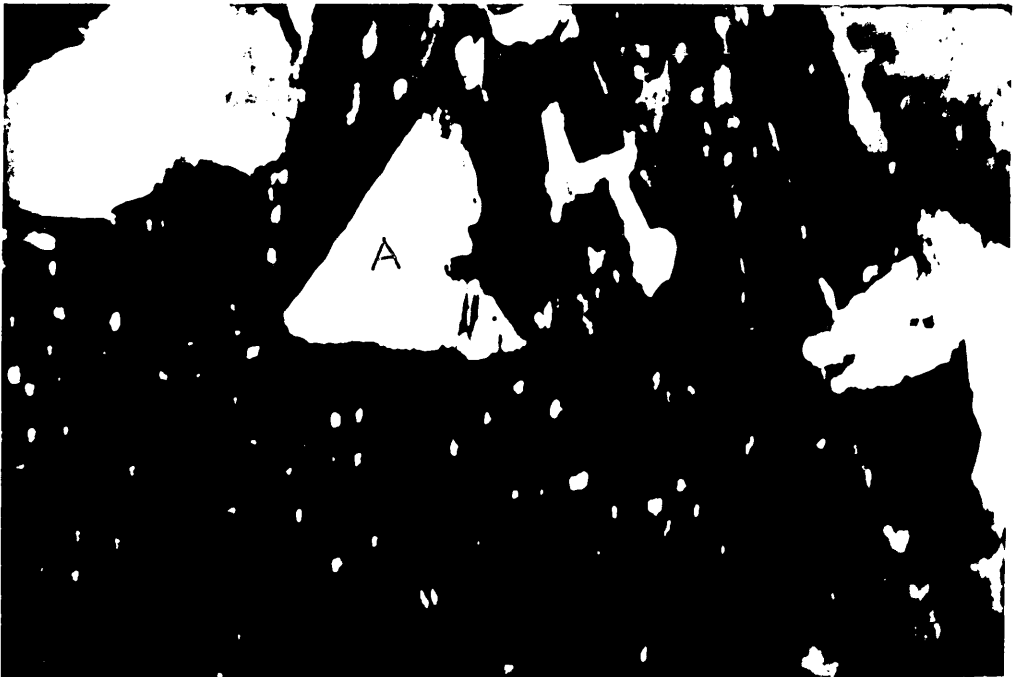
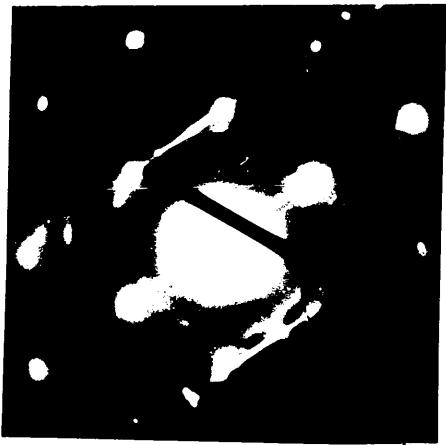
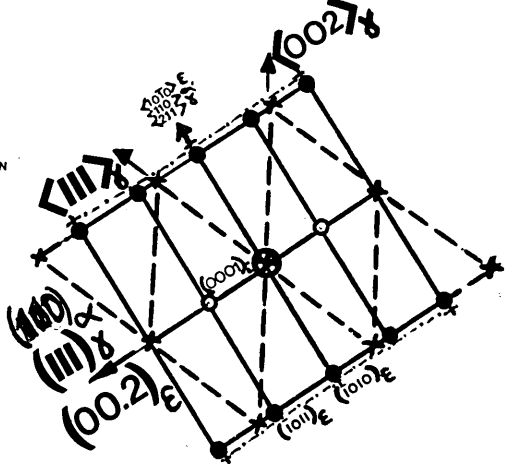


Fig.52 Electron micrograph of alloy K4 water quenched and aged for 7 hours at 475°C, showing finely dispersed precipitates within the laths and also  $\delta$ -phase precipitates ( $\delta_A$ ).  
Mag 2100.000

Fig.53 Electron diffraction pattern of  $(110)_\gamma$ ,  $(111)_{\alpha'}$  and precipitate.

Fig.54 Electron diffraction pattern of  $(110)_\gamma$ ,  $(111)_{\alpha'}$  and precipitate.

Fig.55 Dark field image of Fig.52 using  $(200)_\gamma$  and precipitate reflections.

Fig.56. Dark field image of Fig.52 using  $(111)_\gamma$  precipitate reflections.

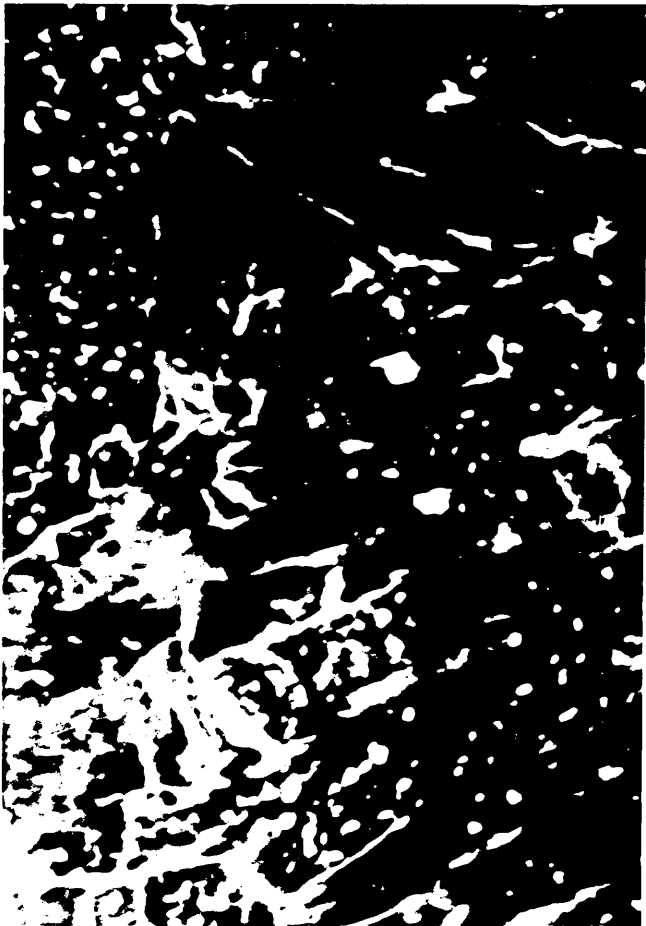


Fig.57 Electron micrograph of alloy 14 water quenched and aged  
for 2 hours at 425<sup>o</sup>C showing stacking faults. Mag 1.100.00

Fig.58 Electron diffraction pattern of  $(110)_{\gamma}$  Twin and  $(031)_{\epsilon}$  .

Fig.59 Dark field image of Fig.57 using  $(111)_{\gamma}$  reflection.

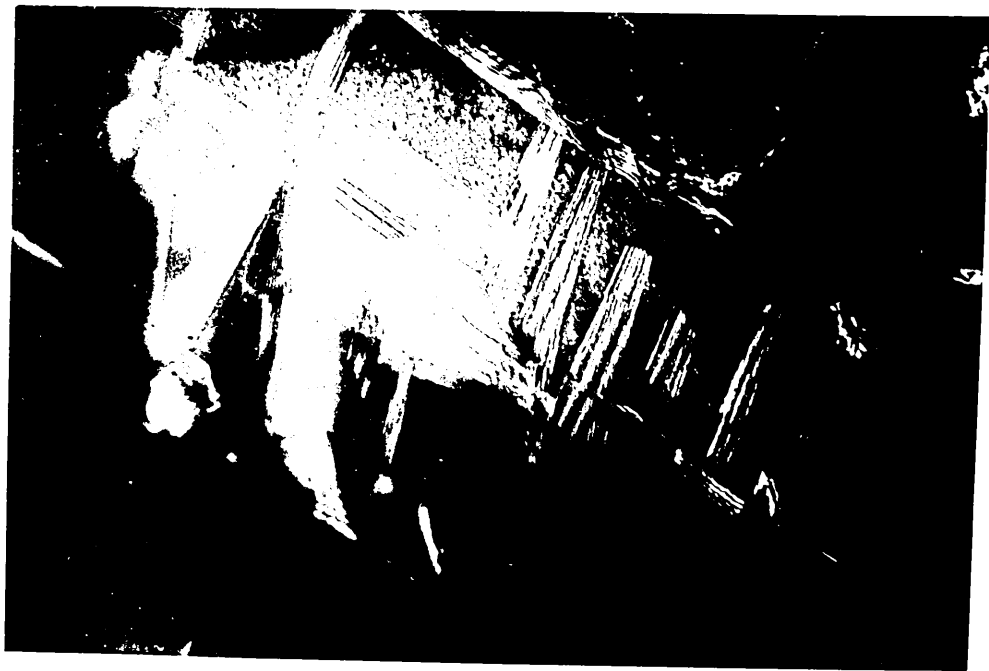
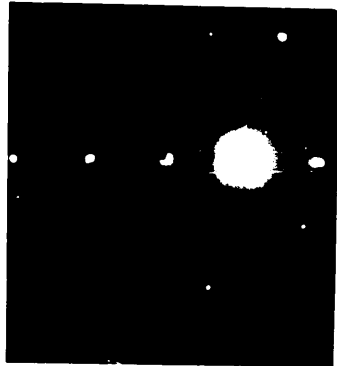
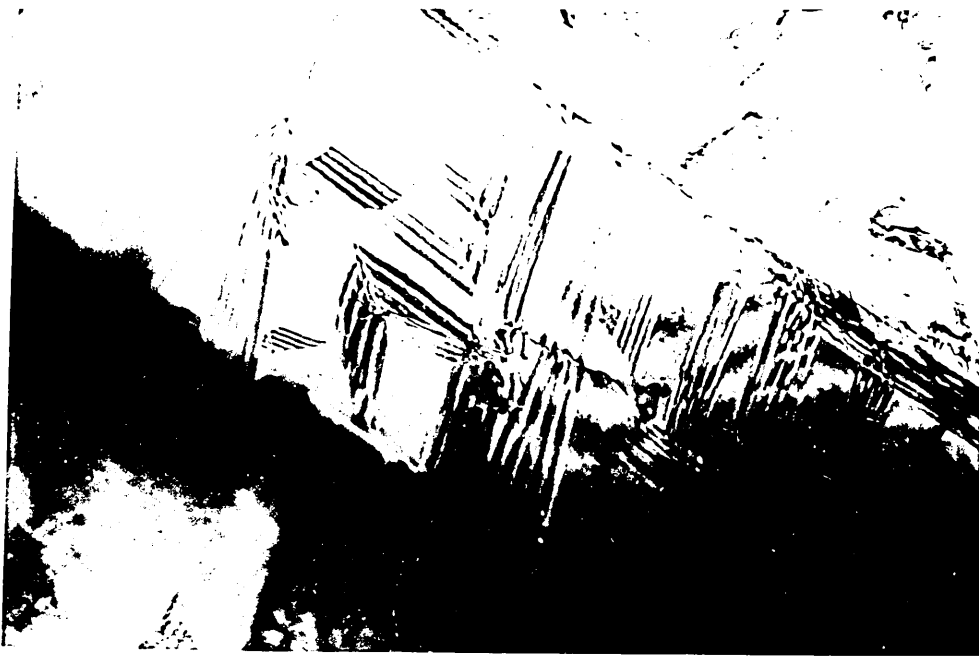


Fig. 60 Electron micrograph of alloy K4 water quenched and aged for 2 hours at 425°C showing  $\epsilon$  band,  $\alpha$  martensite inside  $\epsilon$  band, and  $\gamma$ - phase precipitate (A). Mag X100,000

Fig. 61 Electron diffraction pattern showing fcc, cph and bcc zones.

Fig. 62 Darkfield of a cph reflection.

Fig. 63 Electron micrograph of alloy K3 water quenched and aged 1000 hours at 550°C showing precipitate both within the lath and on the lath boundaries. Mag X200,000

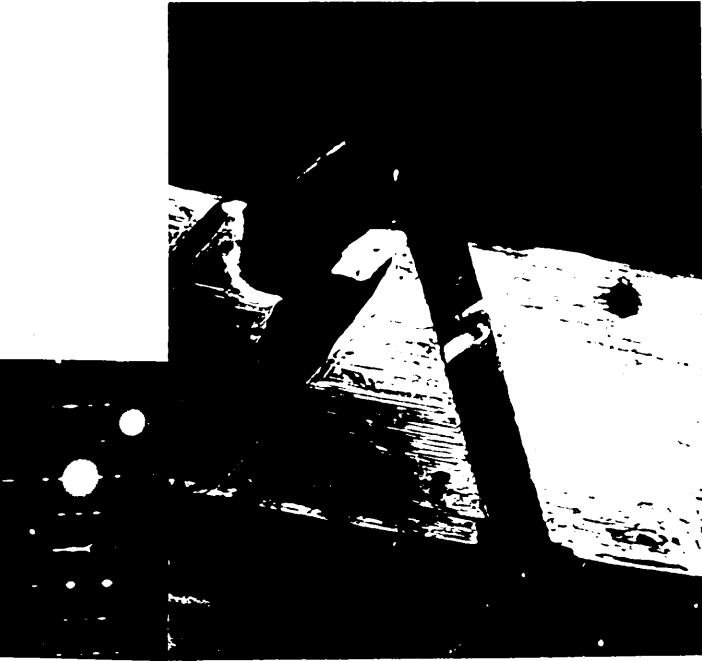


Fig.64 Effect of ageing time at 525<sup>o</sup>C on the matrix structure of alloy K4.

Fig.65 Effect of ageing at 600<sup>o</sup>C on the matrix structure of alloy K4.

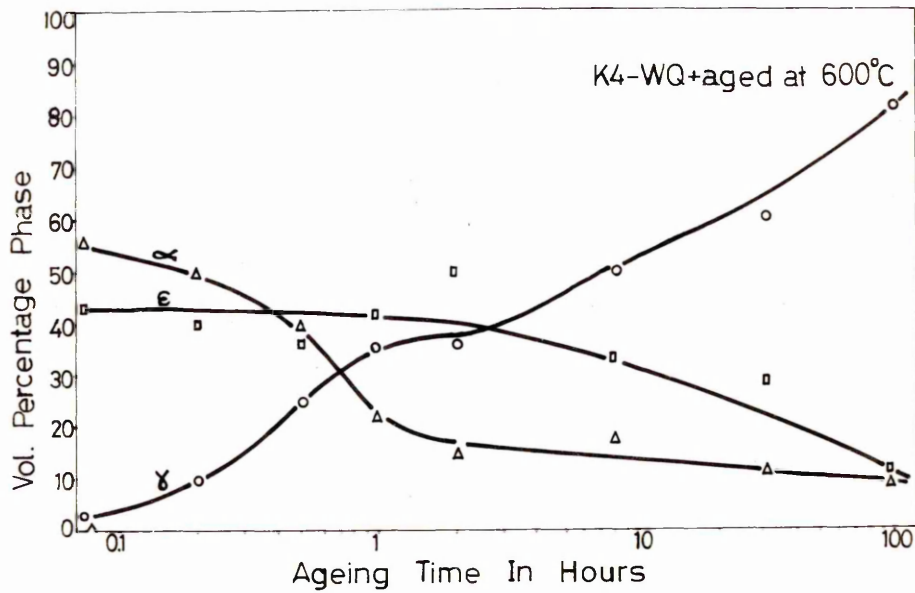
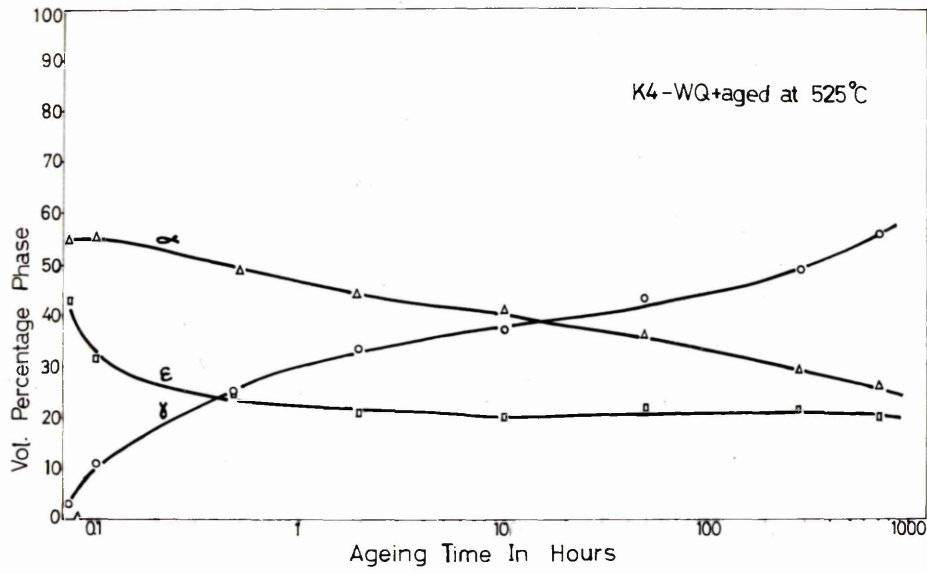


Fig. 66 Effect of ageing time at 525°C on the austenite reversion  
in alloys K2 → K4.

Fig. 67 Effect of ageing time at 525°C on the austenite reversion  
in alloys K5 → K7.

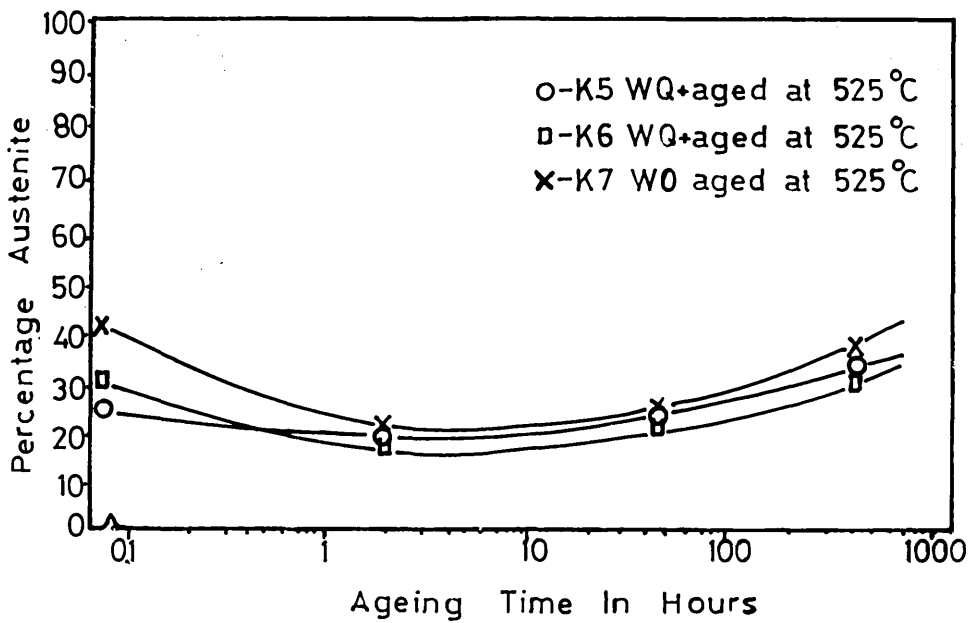
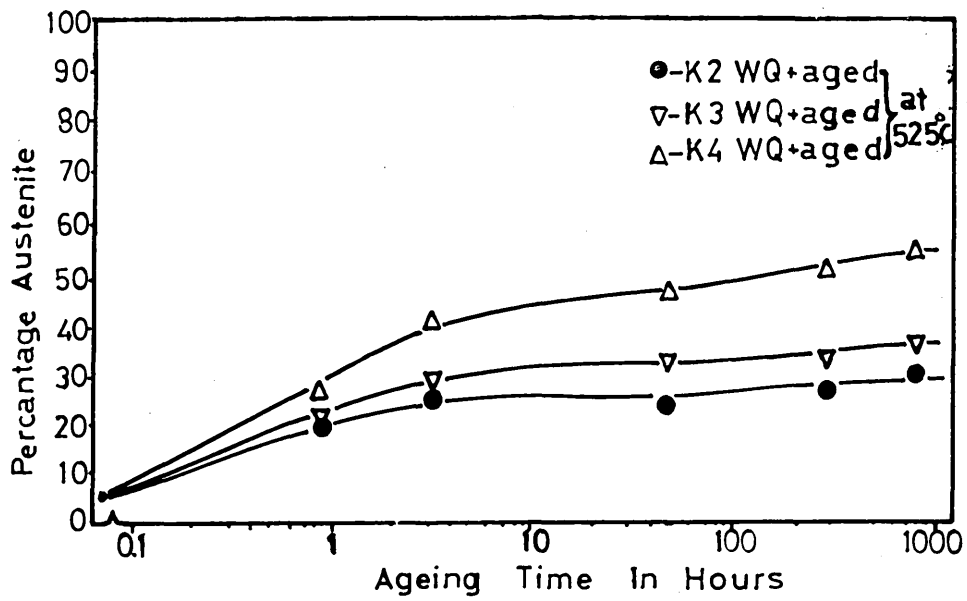


Fig.68 Electron micrograph of alloy water quenched and aged 1000 hours at 550° C showing reverted austenite (A). Mag 1100,000

Fig.69 Electron diffraction pattern of  $(01.1)_E$

Fig.70 Dark field of Fig.68.



Fig.71 Electron micrograph of alloy E6 water quenched and aged for  
1000 hours at 350°C showing overlapping  $\epsilon$  martensite laths.  
Mag: 1100,000

Fig.72 Electron diffraction pattern of  $(01.1)_\epsilon$

Fig.73 Dark field of Fig.71 using  $(01.1)$  reflection.

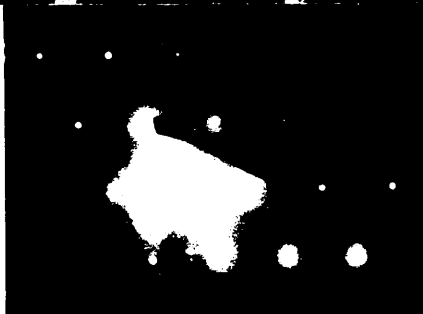
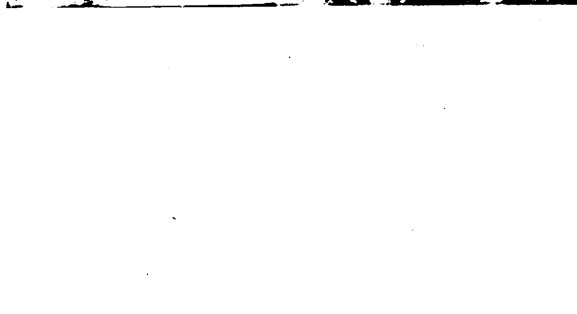


Fig. 74 Composite electron micrograph of alloy K2 water quenched and aged for 1000 hours at 550°C showing lath structure (  $\alpha'$  and  $\epsilon$  ) and austenite between laths. Neg N100.000



Fig.75 Dark field image of Fig.74 using  $(02.2)_E$  reflection.

Fig.76 Electron diffraction pattern of  $(10.0)_E$ . Streaks through  
in  $\langle 00.2 \rangle_E$  direction.



Fig.77 Electron micrograph of alloy K3 water quenched and aged for 1000 hours at 550°C, showing martensite, faulted austenite ( $\gamma$ ) and between them  $\epsilon$  martensite bands ( $\epsilon$ ).  
Mag X 100,000

Fig.78 Electron diffraction pattern of  $(\bar{1}23)_\gamma$  and  $(\bar{1}23)_\alpha$

Fig.79 Electron diffraction pattern of  $(\bar{1}23)_\gamma$  Tw and  $(\bar{1}23)_\alpha$

Fig.80 Dark field of Fig.77 using  $(111)_\gamma$  reflection.

Fig.81 Dark field image of Fig.77 using  $(\bar{1}\bar{1}\bar{1})_\gamma$  and  $(011)_\alpha'$  reflections.

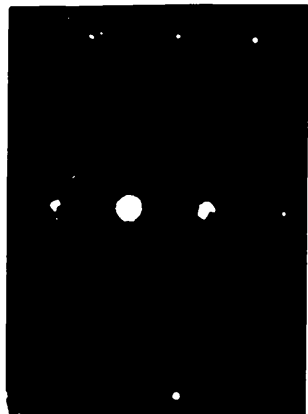
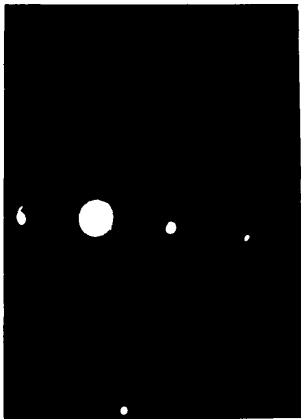


Fig.82 Electron micrograph of alloy #3 water quenched and aged  
1000 hours at 350°C showing  $\alpha'$  martensite crystals ( $\alpha'_1, \alpha'_2$ ) and  
and thin  $\epsilon$  crystals ( $\epsilon$ ). Mag X. 100,000

Fig.83 Electron diffraction pattern of  $(01\bar{1})_\epsilon$

Fig.84 Dark field image of Fig.82 using  $(1\bar{1}1)_\epsilon$  reflection.

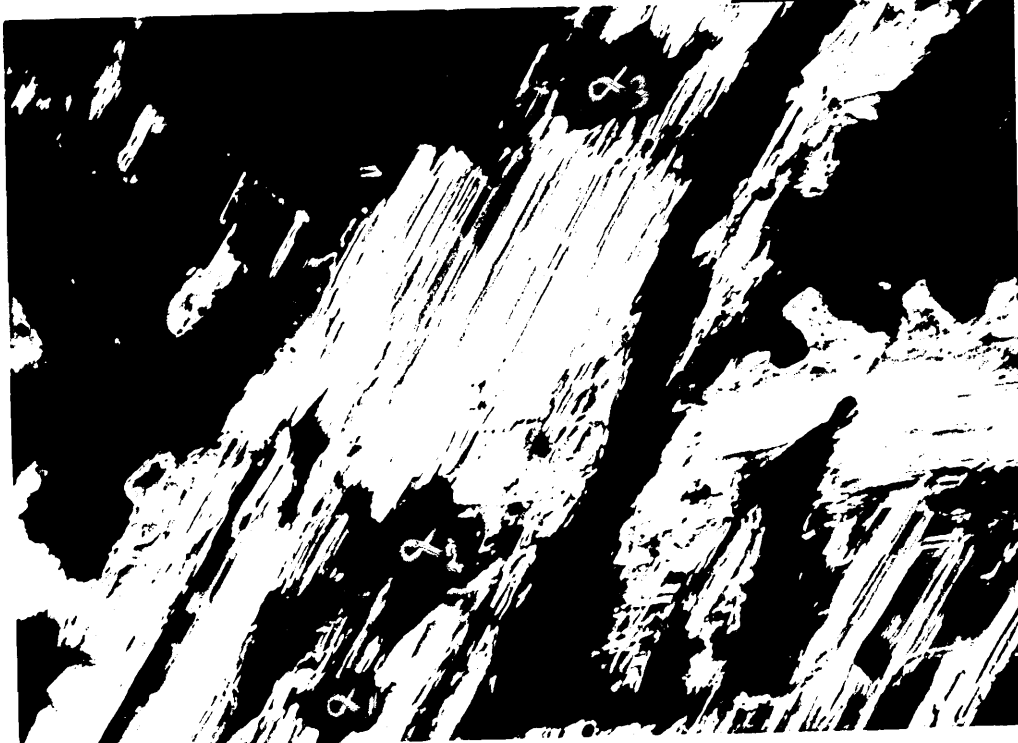
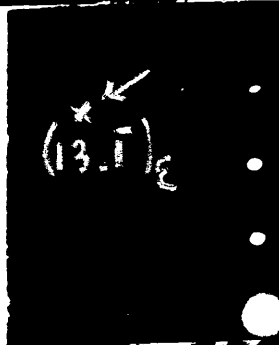
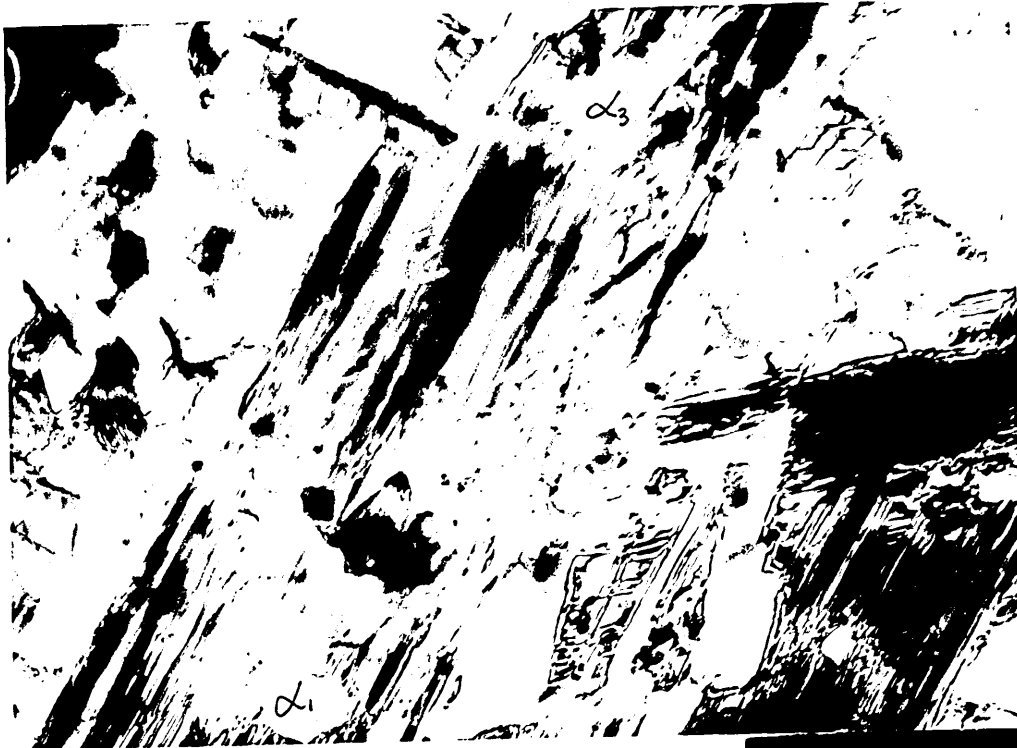


Fig.85 Effect of deformation at room temperature on the hardness of alloys K2 → K7 water quenched.

Fig.86 Effect of deformation at  $-196^{\circ}\text{C}$  on the hardness of alloys K2 → K7 water quenched.

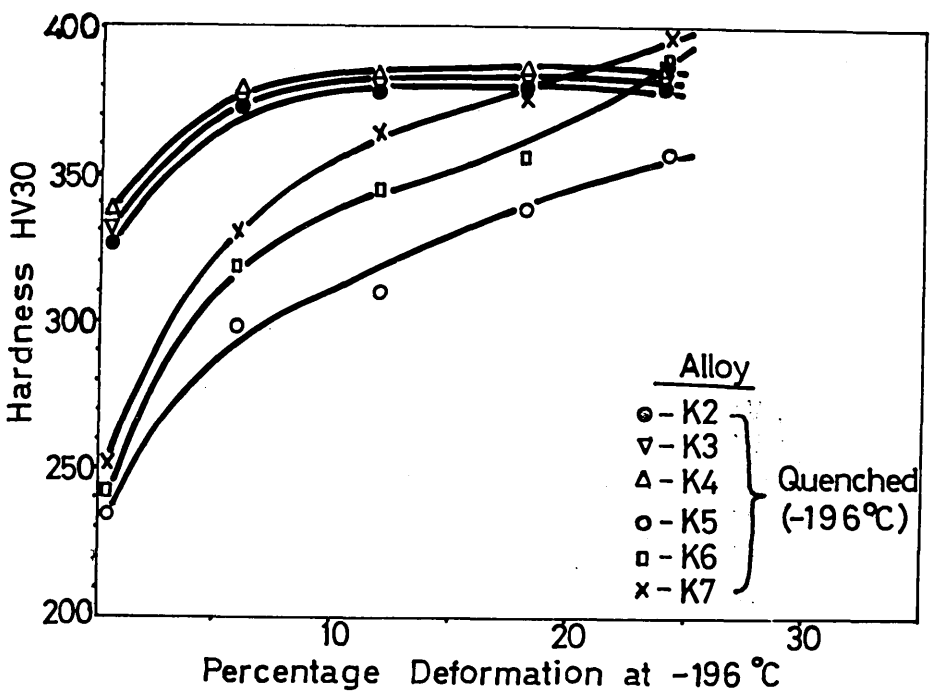
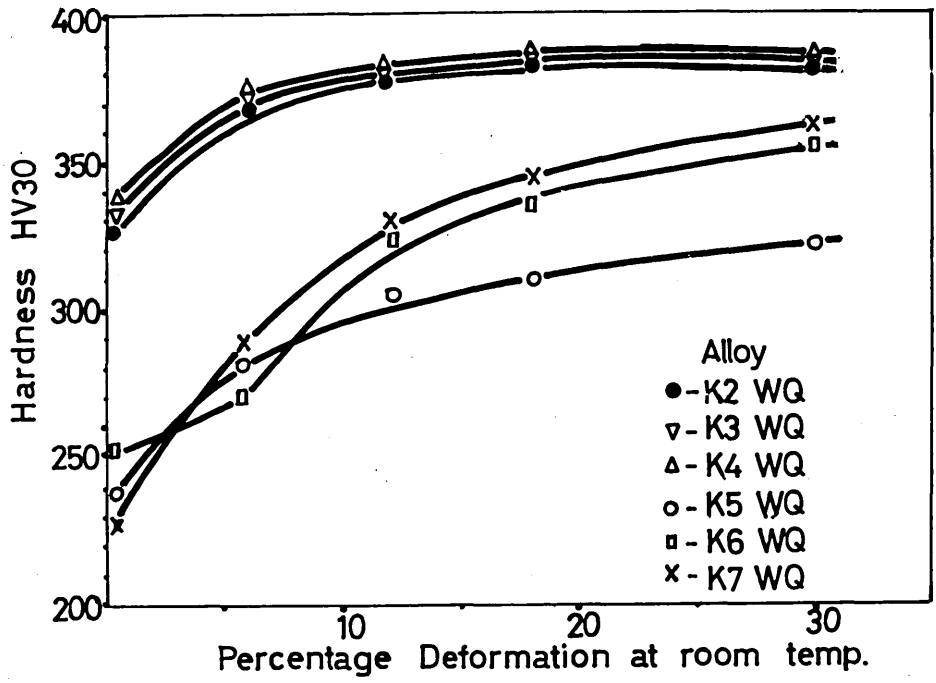


Fig. 87 Effect of deformation at room temperature on the matrix structure in alloys K2 → K4 water quenched.

Fig. 88 Effect of deformation at  $-195^{\circ}\text{C}$  on the matrix structure in alloys K2 → K4 water quenched.

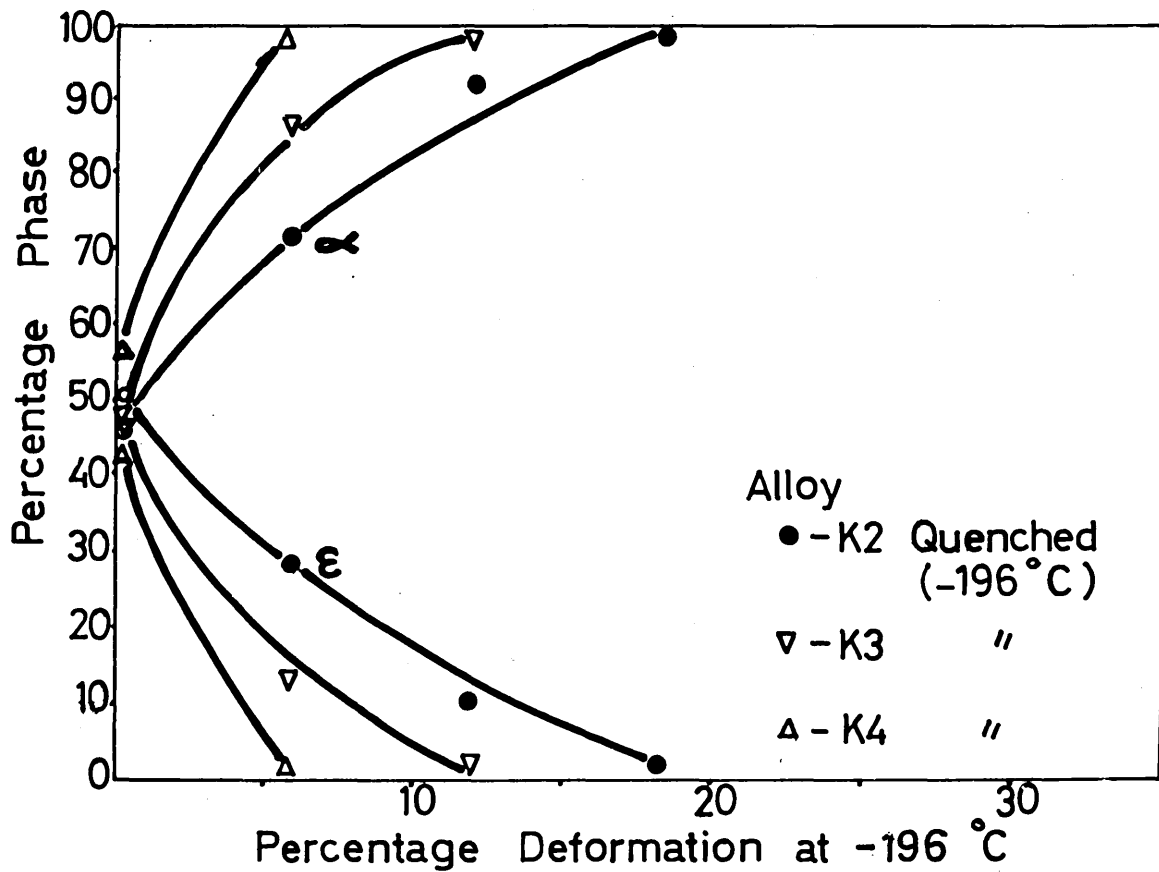
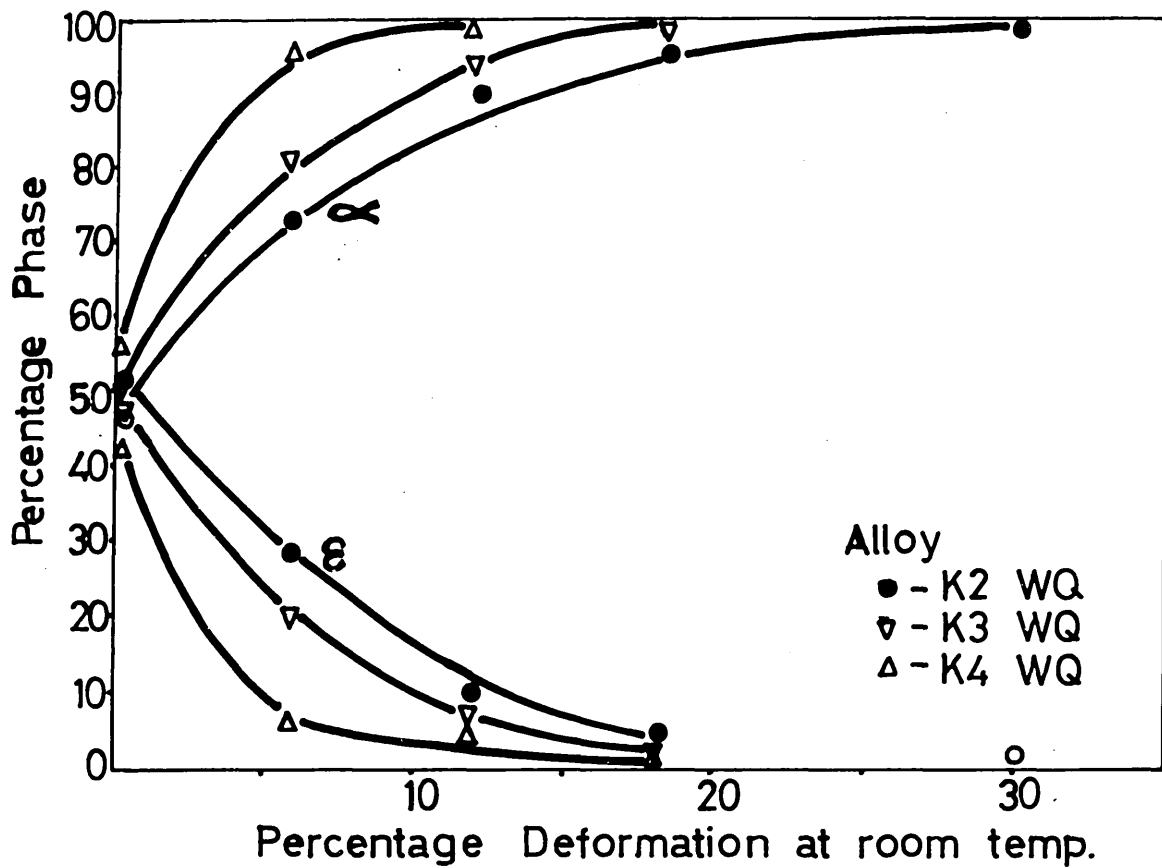


Fig.89 Effect of deformation at room temperature on the  $\epsilon$  phase  
in alloys K5  $\rightarrow$  K7

Fig.90 Effect of deformation at  $-196^{\circ}\text{C}$  on the  $\epsilon$  phase in alloys  
K5  $\rightarrow$  K7.

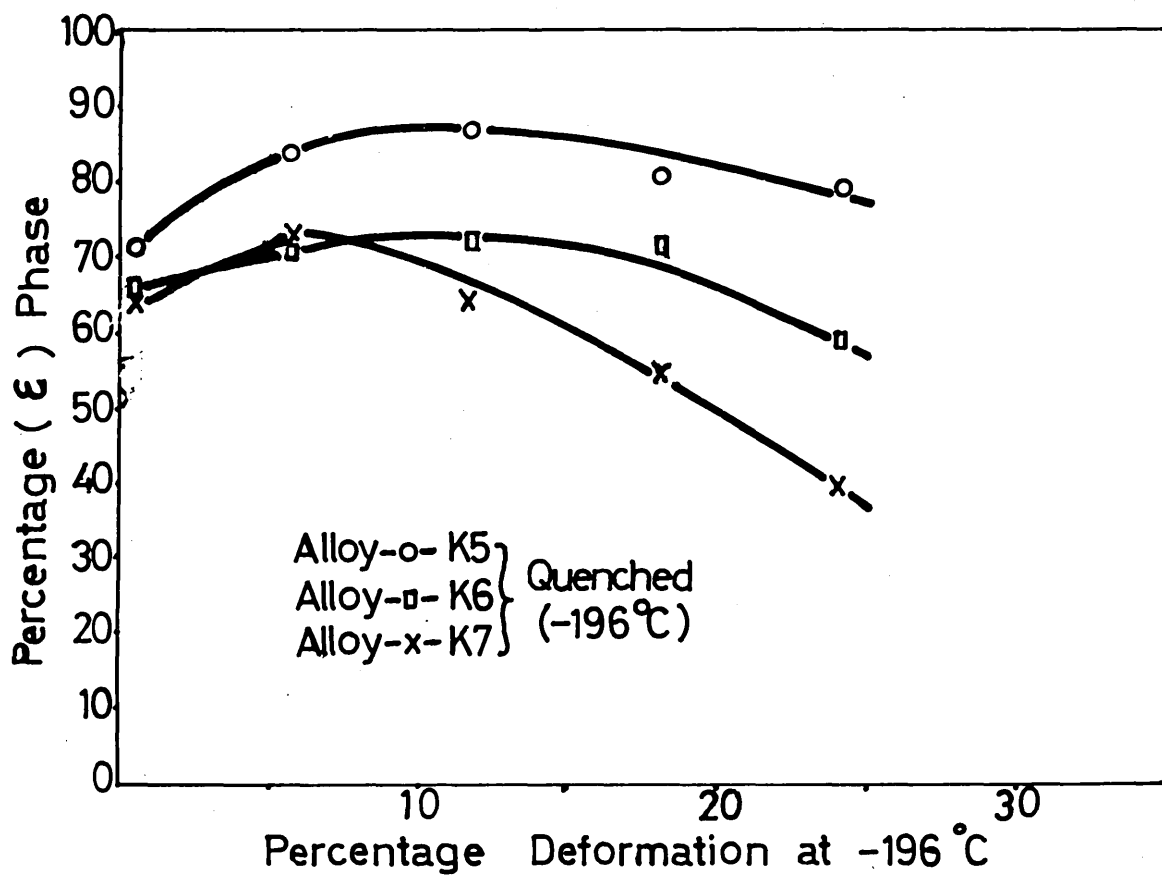
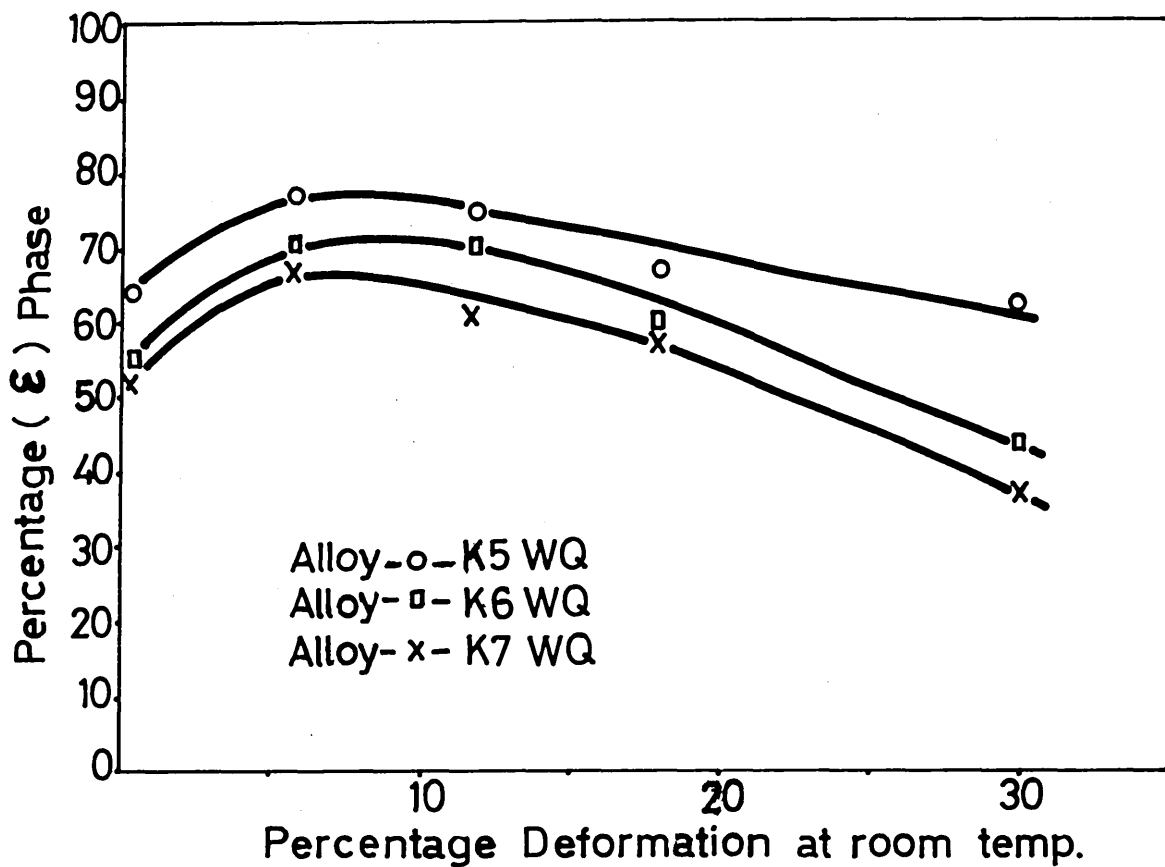


Fig. 91 Effect of deformation at room temperature on the  $\alpha'$  phase  
in alloys K5  $\rightarrow$  K7.

Fig. 92 Effect of deformation at  $-196^{\circ}\text{C}$  on the  $\alpha'$  phase in alloys  
K5  $\rightarrow$  K7.

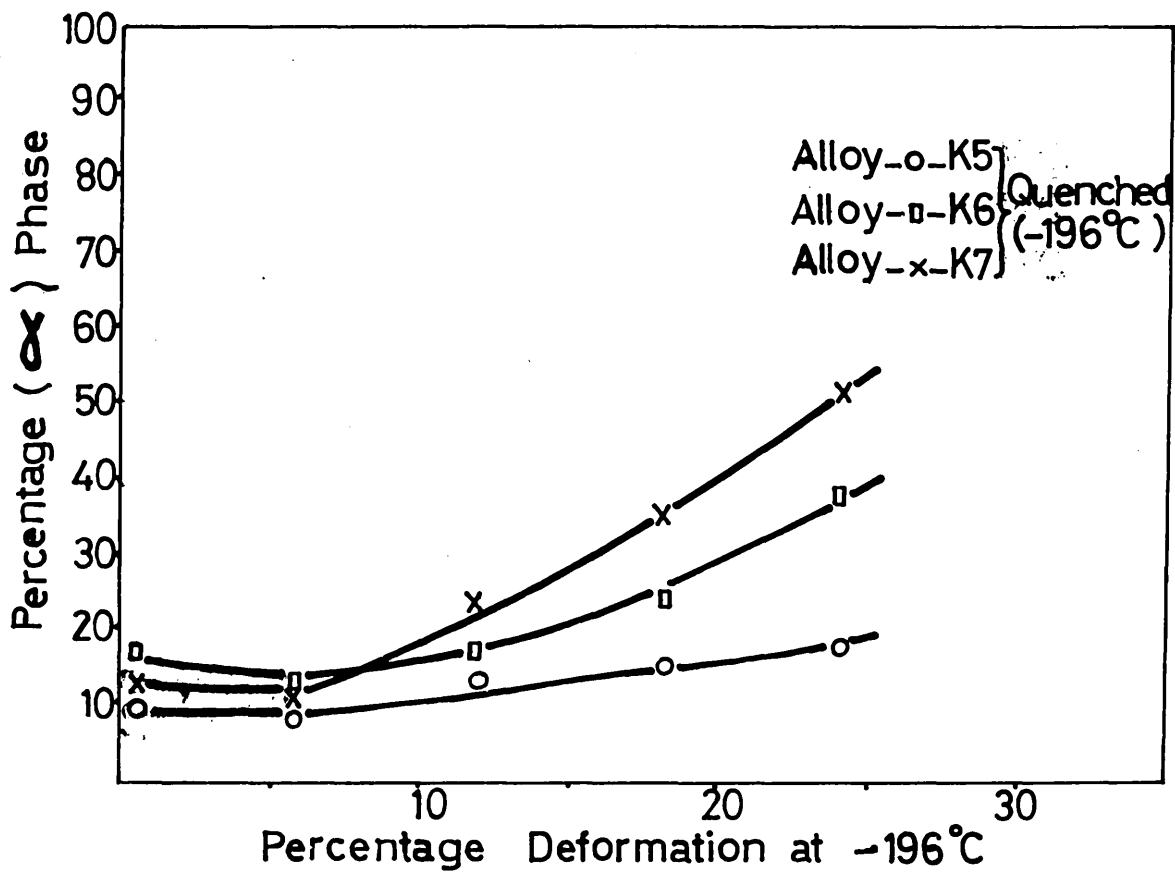
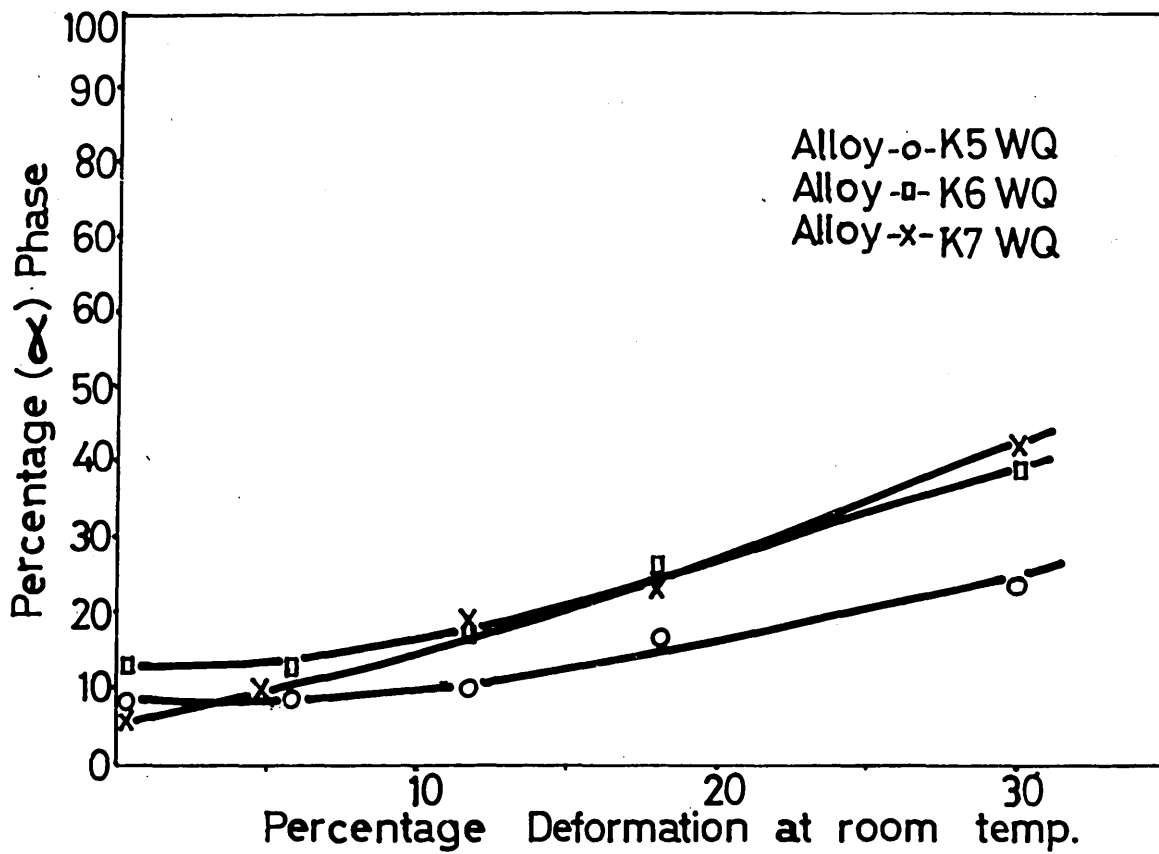


Fig. 23 Effect of deformation at room temperature on the  $\gamma$  phase  
in alloys K5  $\rightarrow$  K7.

Fig. 24 Effect of deformation at  $-196^{\circ}\text{C}$  on the  $\gamma$  phase in alloys  
K5  $\rightarrow$  K7.

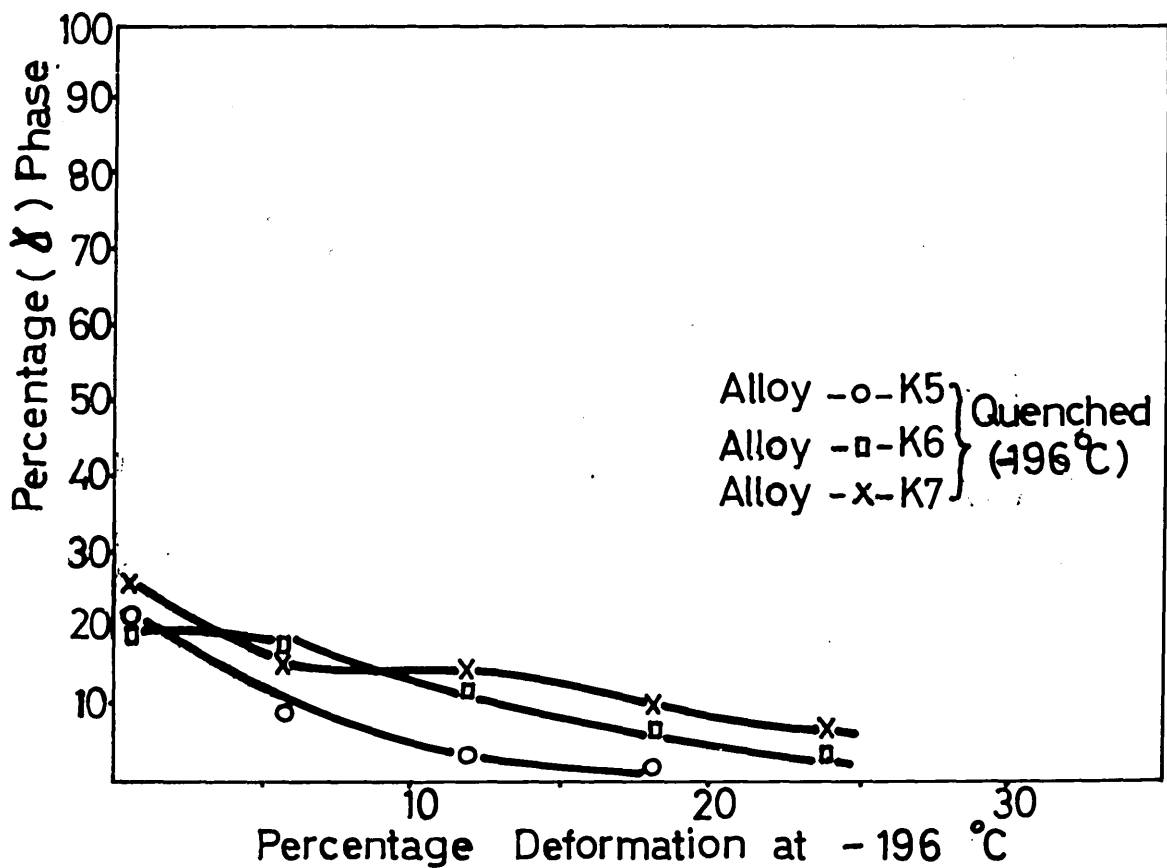
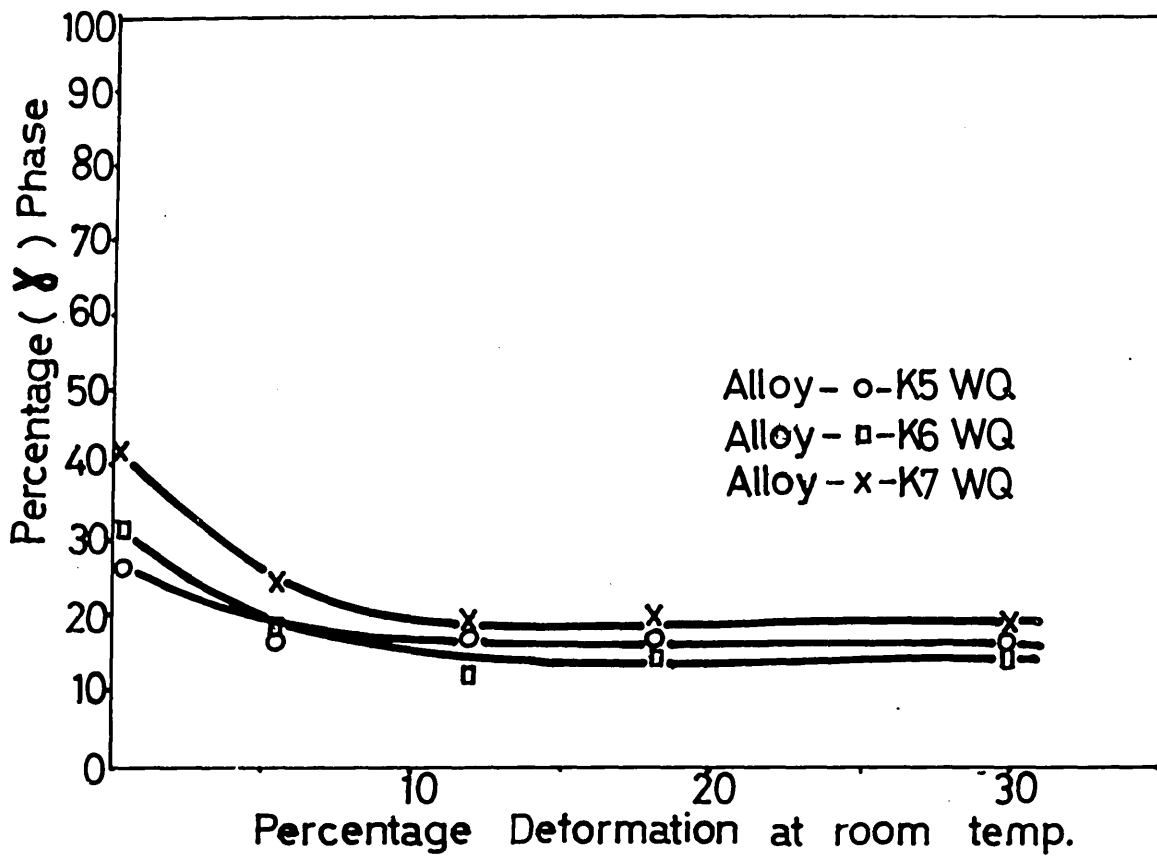


Fig. 95 Optical microstructure  
of alloy K7 quenched and  
6% deformed at  $-196^{\circ}\text{C}$ .  
Mag 1800.

Fig. 96 Optical microstructure  
of alloy K7 quenched and  
deformed at  $-196^{\circ}\text{C}$ , showing  
austenite grains (dark  
 $\epsilon$  martensite (white)) and  
within the austenite. M

Fig. 97 Optical microstructure  
of alloy K5 quenched and 6%  
deformed at  $-196^{\circ}\text{C}$ , showing  $\alpha$   
martensite (black), inside  $\epsilon$   
band (white) and austenite  
(grey). Mag 1800.

Fig. 98 Optical microstructure  
of alloy K5 quenched  
18% deformed at  $-196^{\circ}\text{C}$   
showing  $\alpha$  martensite  
 $\epsilon$  martensite (white)  
austenite (grey). Ma.

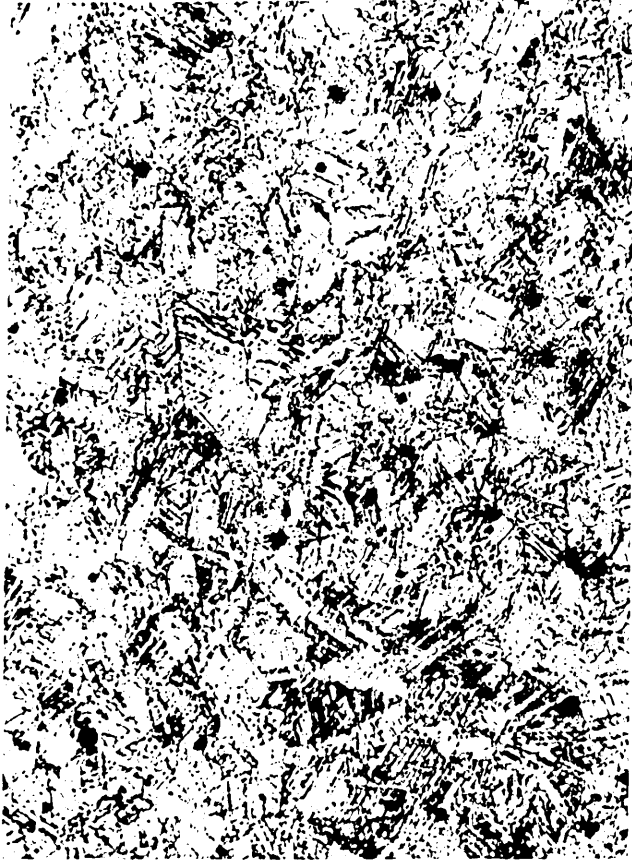


Fig.99 Optical microstructure of alloy K4 quenched and 6%  
deformed at  $-196^{\circ}\text{C}$ . Mag 1300

Fig.100. Optical microstructure of alloy K6 quenched and 18%  
deformed at  $-196^{\circ}\text{C}$ , showing elongated  $\alpha'$  grains inside  
bands. Mag X2250.

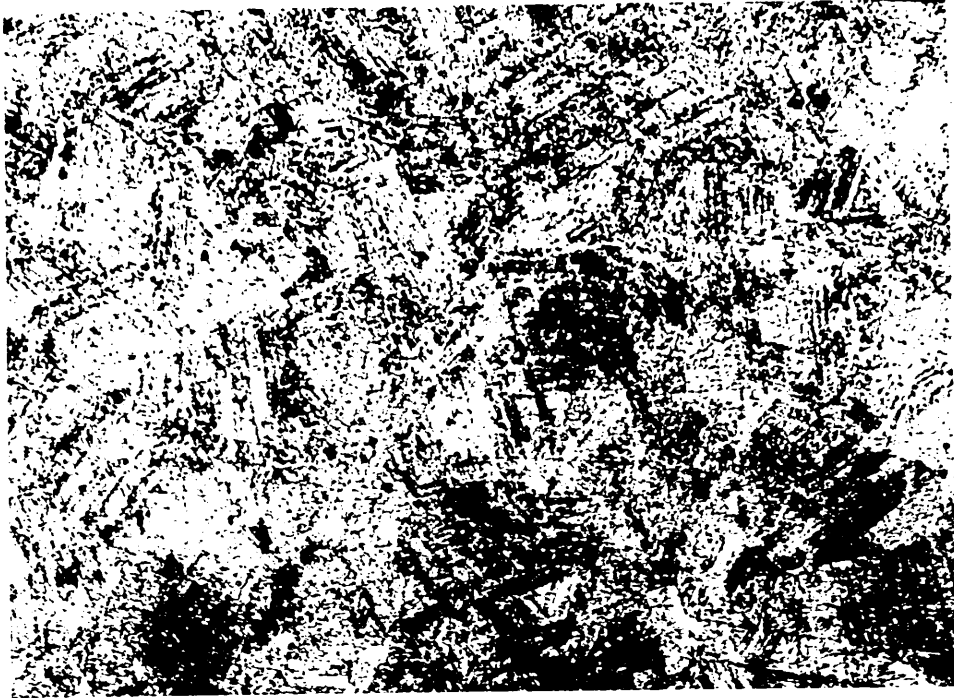


Fig. 101. Optical microstructure of alloy K7 quenched and 6% deformed at  $-190^{\circ}\text{C}$ , showing the transformed region of austenite (brown) to  $\epsilon$  martensite and growth of  $\alpha$  martensite (blue) inside  $\epsilon$  martensite (yellow).  
Mag 12800.

Fig.102. Optical microstructure of alloy K7 quenched and 12% deformed at  $-196^{\circ}\text{C}$ , showing the increased  $\alpha'$  martensite regions (blue) inside  $\epsilon$  martensite (yellow) and austenite (brown). Mag X2800.

Fig. 108. Optical microstructure of alloy K7 quenched and 18% deformed at  $-196^{\circ}\text{C}$  showing  $\alpha$  martensite (blue),  $\epsilon$  martensite (yellow) and austenite (brown). Mag X2800.

Fig.104 X-ray diffraction trace of alloys K8 and K7 water quenched showing  $(10.1)_{\epsilon}$ ,  $(200)_{\gamma}$  and  $(200)_{\alpha'}$  peaks used for phase determination.

Fig.105 Electron micrograph of alloy K7 quenched and 15% deformed at  $-196^{\circ}\text{C}$ , showing twin related martensite laths (dark), inside  $\epsilon$  laths (grey) and retained austenite (R.A.) along the lath boundaries. Mag X.40,000

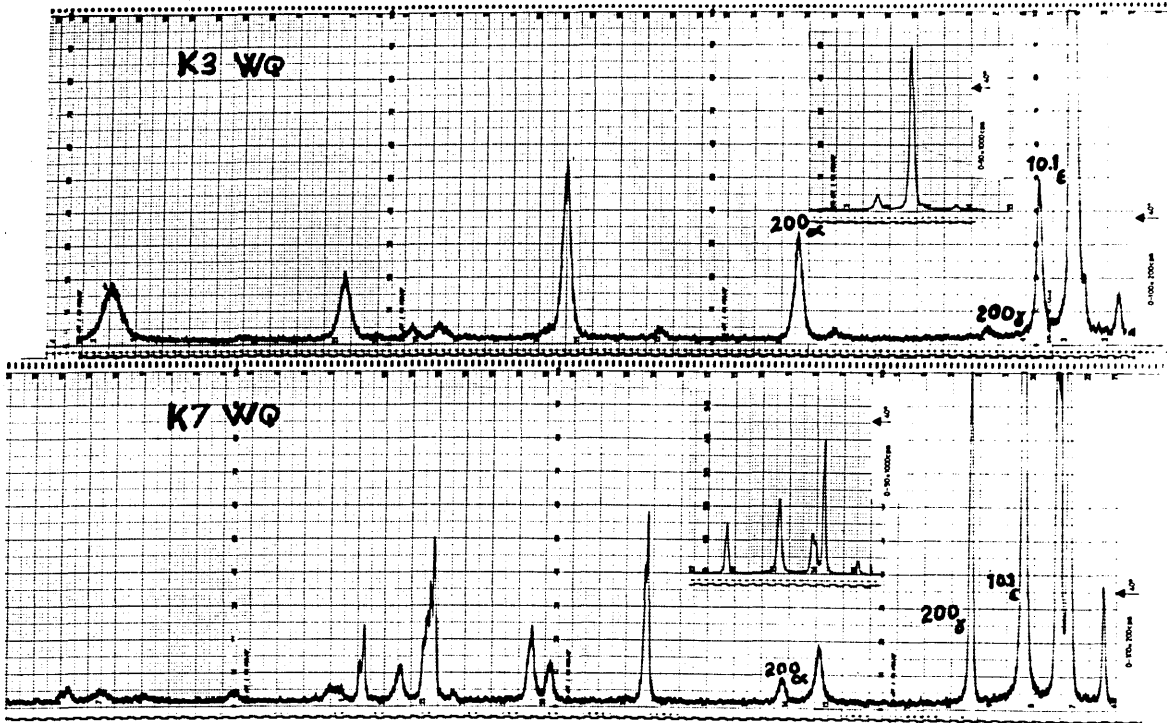


Fig.106 Composite electron micrograph of alloy K7 quenched and  
10% deformed at  $-196^{\circ}\text{C}$ , showing  $\alpha$  martensite at the  
intersection of  $\epsilon$  bands. Mag X100,000



Fig.107 Composite dark field of Fig.106 using  $(11.1)_{\epsilon}$  reflection,  
showing thin  $\epsilon$  martensite twins.

Fig.108. Diffraction pattern of  $(12.1)_{\epsilon}$  Twin.



Fig.109. Electron micrograph of alloy R7 water quenched and  
18% deformed at  $-196^{\circ}\text{C}$ . Mag 2150.000

Fig.110. Electron diffraction patterns of  $\langle 110 \rangle_{\delta}$  and  $\langle 11\bar{5} \rangle_{\delta}$  zones.

Fig.111. Dark field of Fig.109 using  $(110)_{\delta}$  and  $(111)_{\delta}$  reflections.

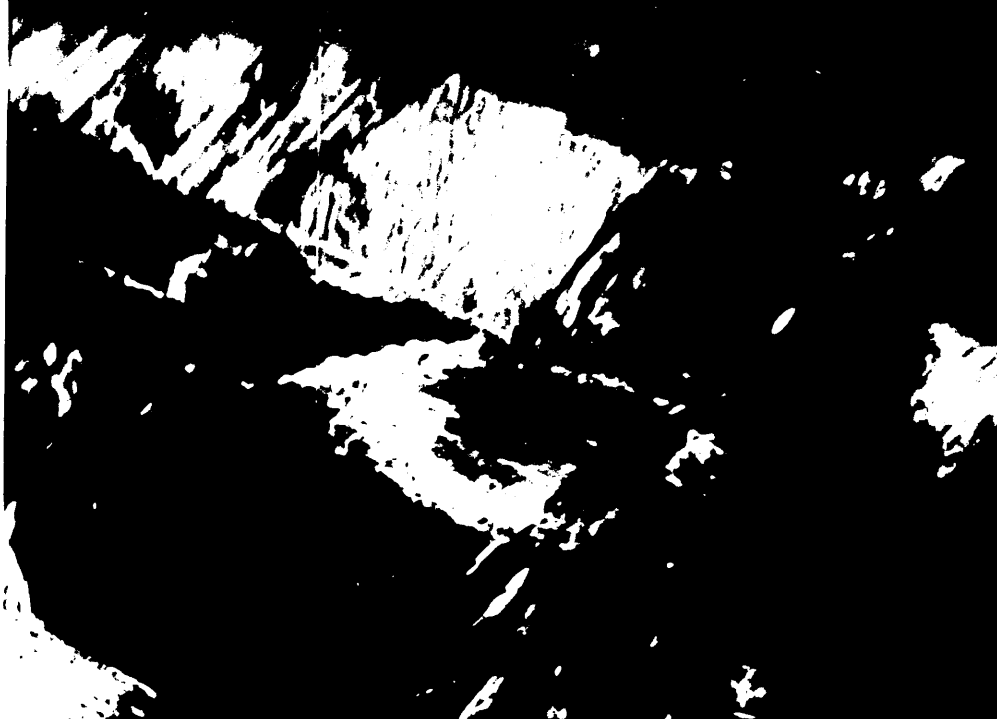
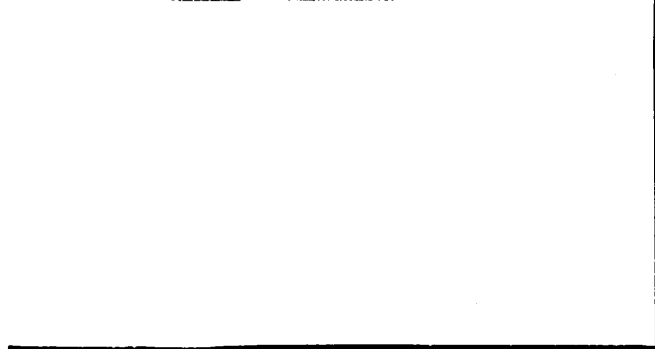
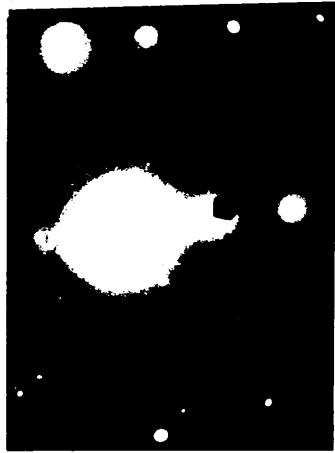
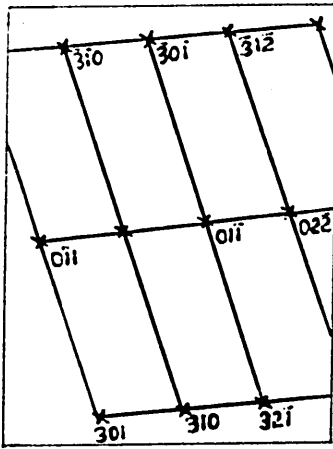


Fig.112. Electron diffraction pattern of $(\bar{1}00)_{\alpha'}$	Fig.113 Electron micrograph of alloy E7 quenched and 18% deformed at -190°C showing $\alpha'$ martensite laths. Mag.X 100,000	Fig.114 21 di is cr ( $\bar{1}$ an
---	--	---

Fig.115. Dark field of Fig.113  
using  $(01\bar{1})_{\alpha'}$  reflection.

Fig.116. Dark field of Fig.113  
using  $(\bar{2}2\bar{2})_{\alpha'}$  reflectio

$x - [\bar{1}33]_{\alpha}$



$x - [\bar{1}33]_{\alpha} \quad o - [\bar{1}12]_{\alpha}$

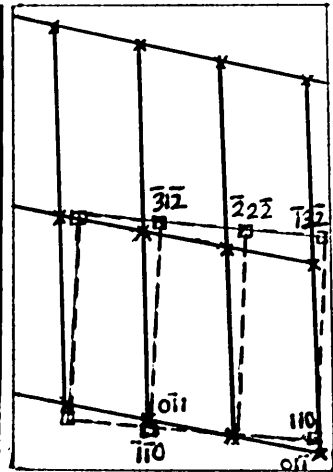


Fig.117 Effect of deformation at room temperature on the hardness of alloy K2 water quenched and aged for 2 hours.

Fig.118 Effect of deformation at  $-196^{\circ}\text{C}$  on the hardness of alloy K2 quenched to  $-196^{\circ}\text{C}$  and aged for 2 hours.

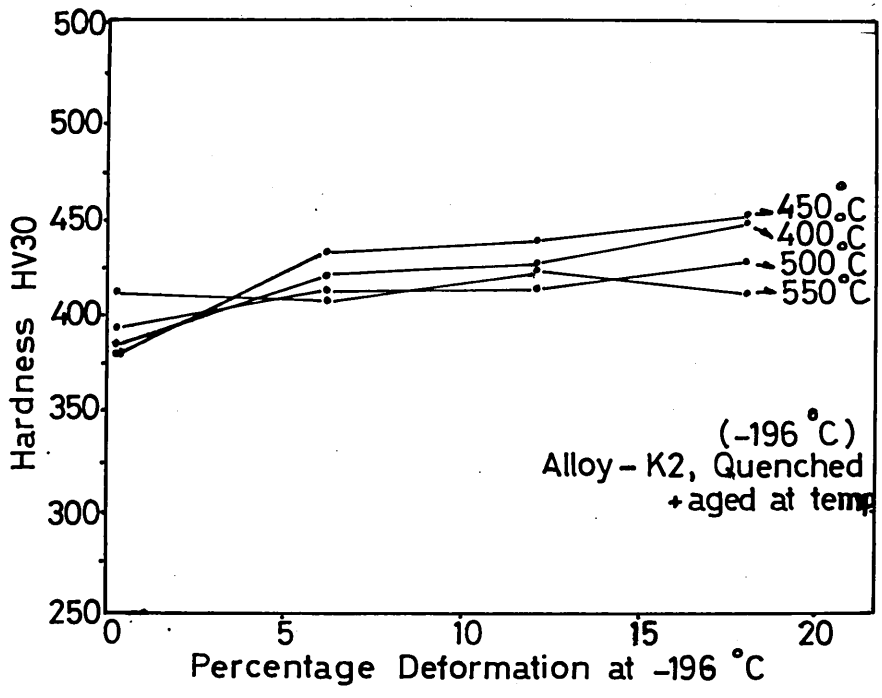
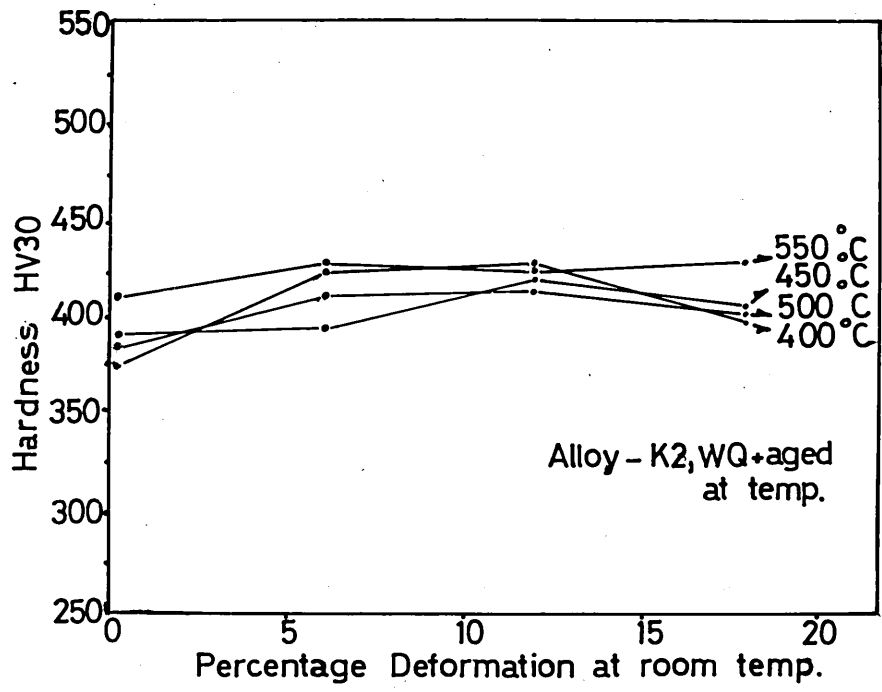


Fig.119. Effect of deformation at room temperature on the hardness of alloy 43 water quenched and aged for two hours.

Fig.120. Effect of deformation at  $-196^{\circ}\text{C}$  on the hardness of alloy 43 quenched to  $-196^{\circ}\text{C}$  and aged for 2 hours.

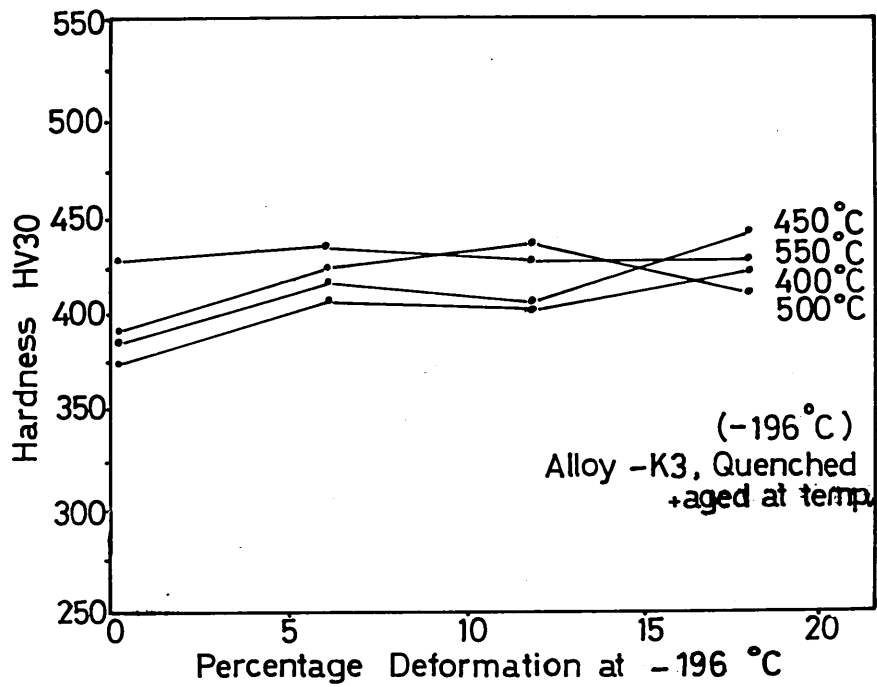
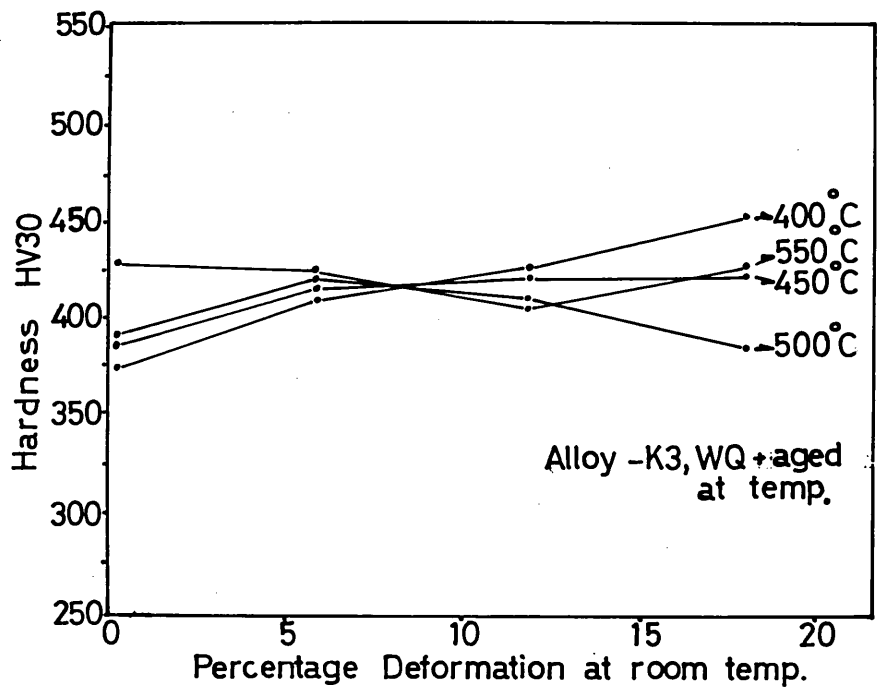


Fig.121. Effect of deformation at room temperature on the hardness of alloy K4 water quenched and aged for 2 hours.

Fig.122. Effect of deformation at  $-196^{\circ}\text{C}$  on the hardness of alloy K4 quenched to  $-196^{\circ}\text{C}$  and aged for 2 hours.

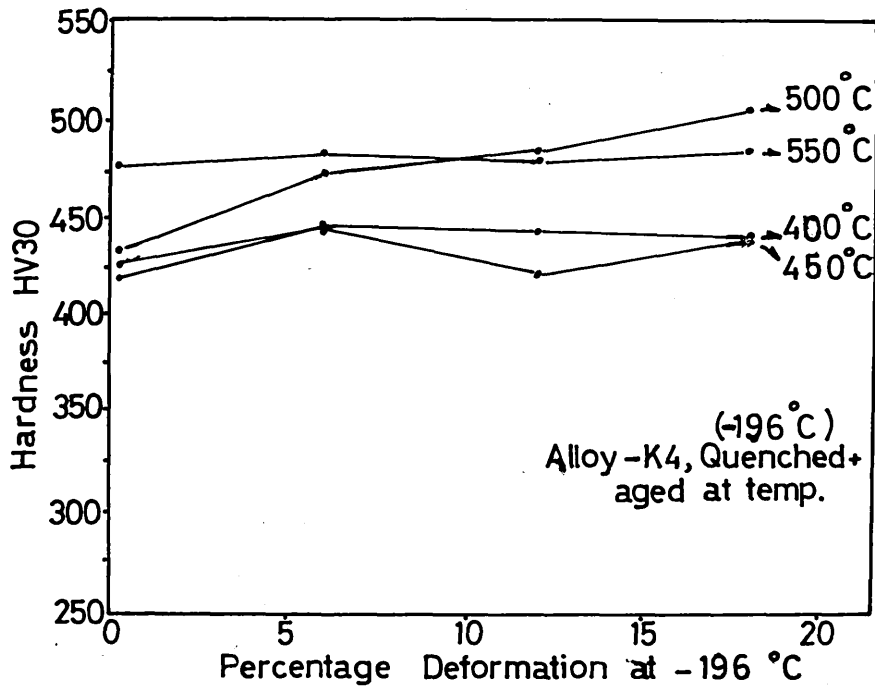
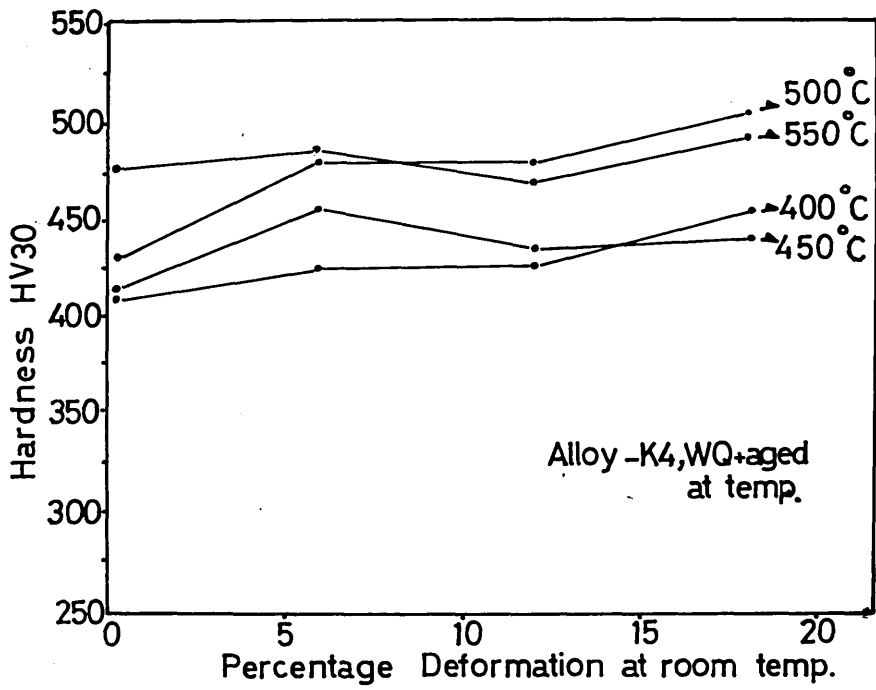


Fig.123. Effect of deformation at room temperature on the hardness of alloy #5 water quenched and aged for 2 hrs.

Fig.124. Effect of deformation at  $-196^{\circ}\text{C}$  on the hardness of alloy #5 quenched to  $-196^{\circ}\text{C}$  and aged for 2 hrs.

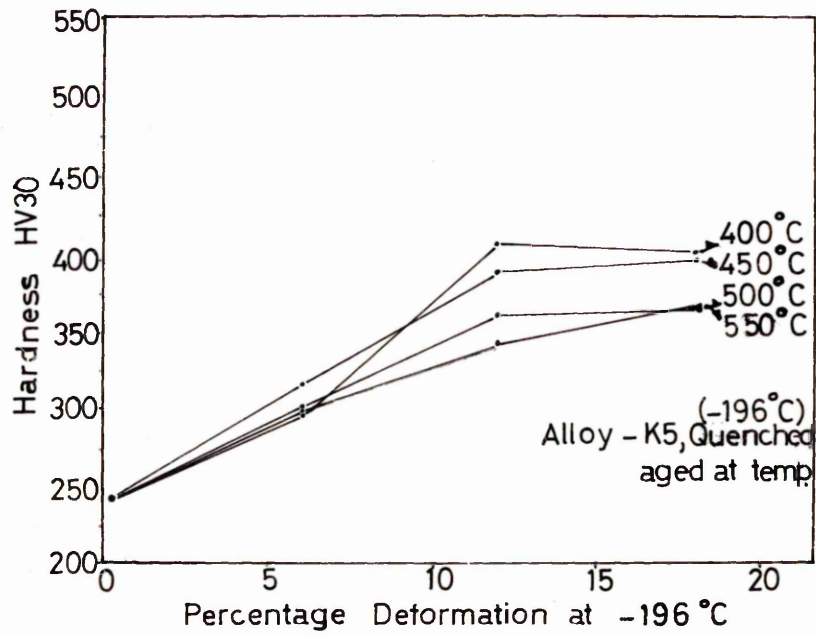
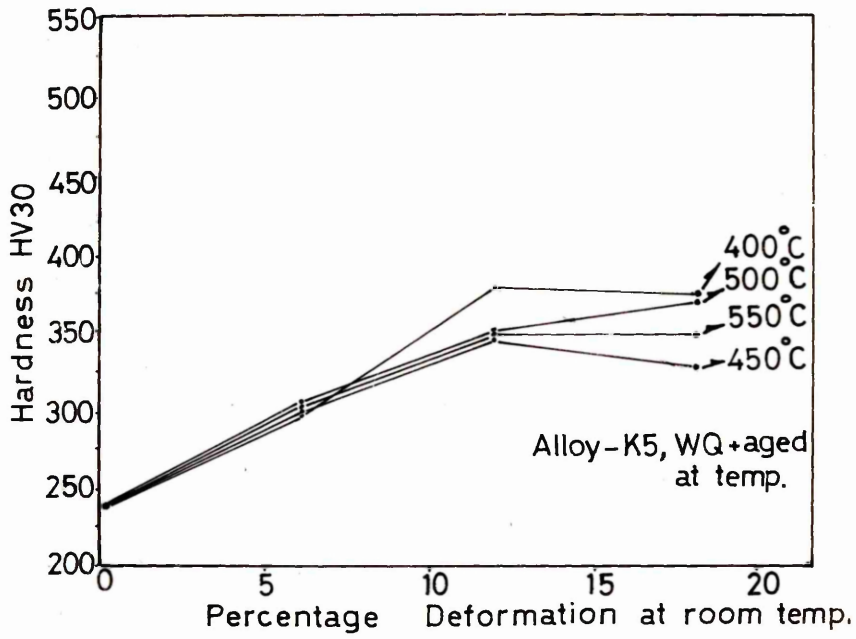
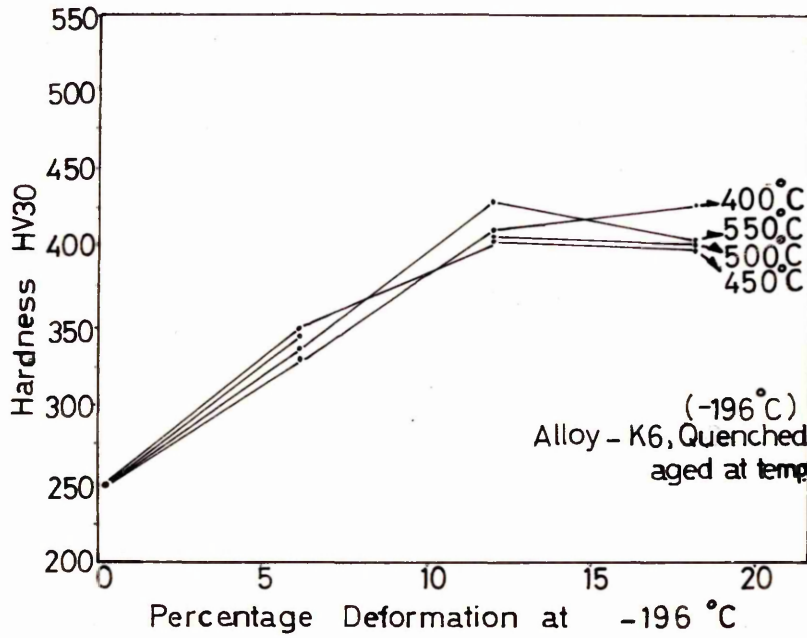
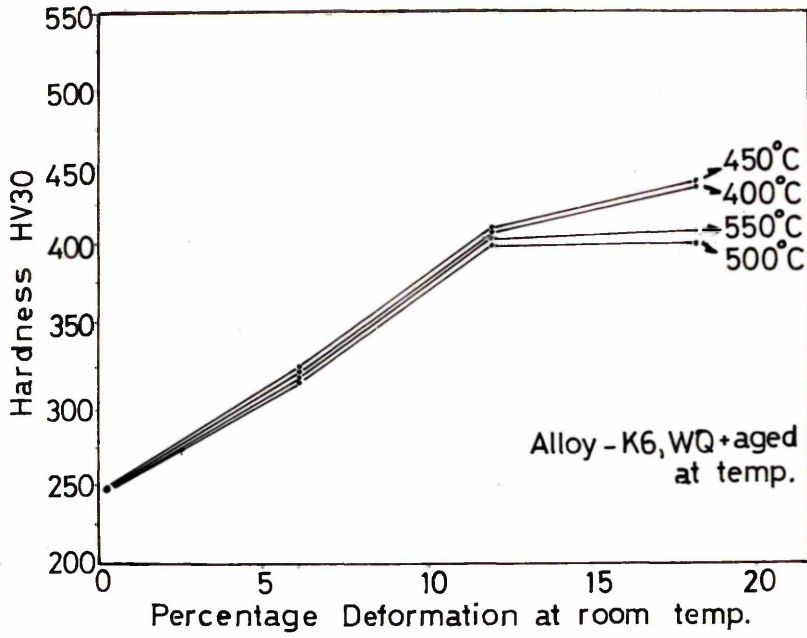


Fig.125. Effect of deformation at room temperature on the hardness of alloy K6 water quenched and aged for 2 hrs.

Fig.126. Effect of deformation at  $-196^{\circ}\text{C}$  on the hardness of alloy K6 quenched to  $-196^{\circ}\text{C}$  and aged for 2 hrs.



cf  
value shown  
in T-387

Fig.127. Effect of deformation at room temperature on the hardness of alloy K7 water quenched and aged for 2 hrs.

Fig.128. Effect of deformation at  $-196^{\circ}\text{C}$  on the hardness of alloy K7 quenched to  $-196^{\circ}\text{C}$  and aged for 2 hrs.

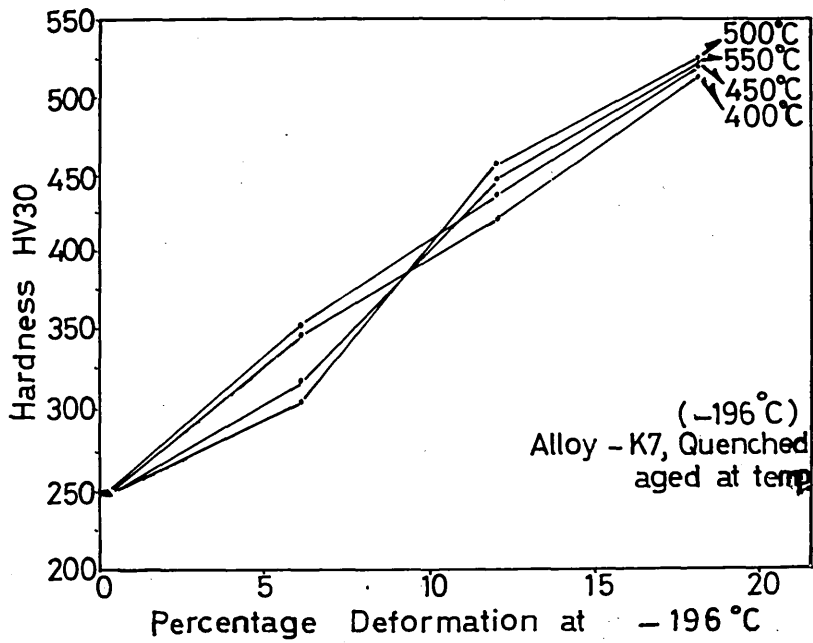
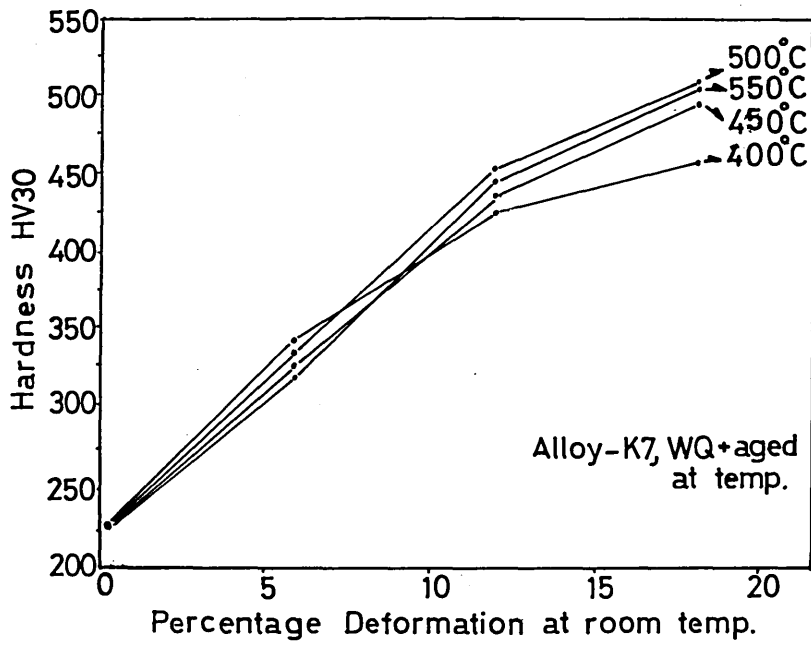


Fig.129. Electron micrograph of alloy K7 quenched and 18% deformed at  $-196^{\circ}\text{C}$  and aged for 2 hours at  $550^{\circ}\text{C}$  showing twin  $\epsilon$  martensite crystals. Mag X100,000

Fig.130. Electron diffraction pattern of  $(\bar{1}1.0)_{\epsilon}$

Fig.131. Electron diffraction pattern of  $(12.1)_{\epsilon}$  Twin.

Fig.132. Dark field of Fig.129 using  $(0\bar{1}.1)_{\epsilon}$  reflection.

Fig.133. Dark field of Fig.129 using  $(\bar{1}1.\bar{1})_{\epsilon}$  reflection.

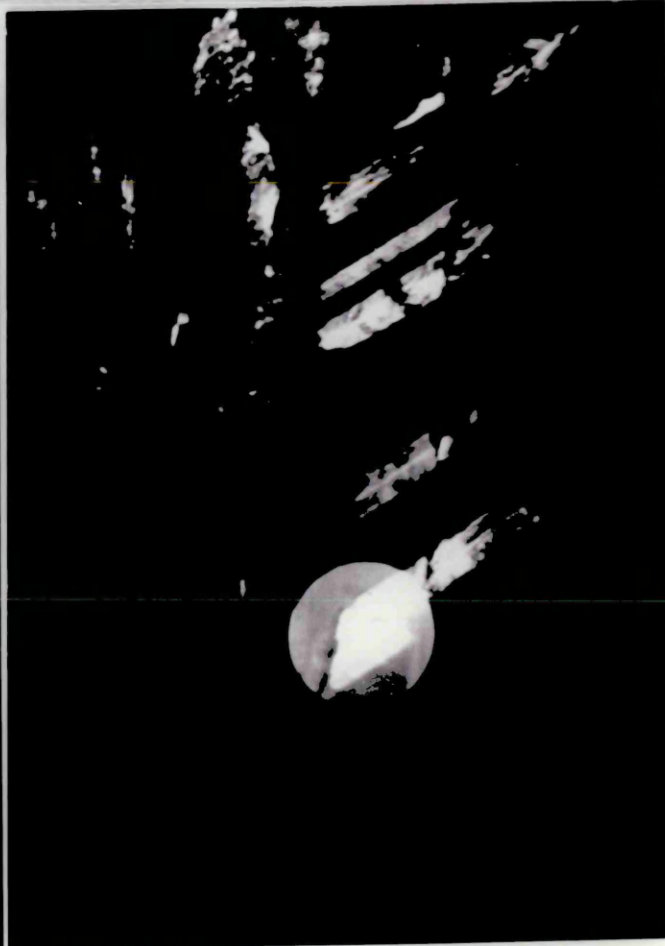
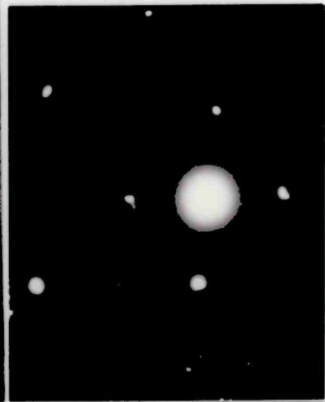


Fig.134. Electron micrograph of alloy A7 quenched and 10% deformed at  $-196^{\circ}\text{C}$  and aged for 96 hrs at  $550^{\circ}\text{C}$ , showing precipitates and faulted particles. Mag 1100,000

Fig.135. Electron diffraction pattern.

Fig.136. Dark field image from same area as above.

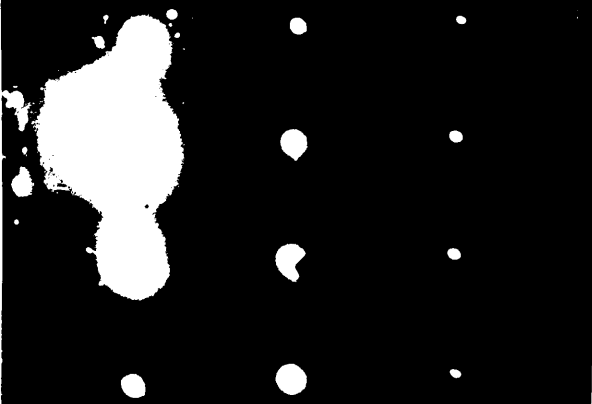
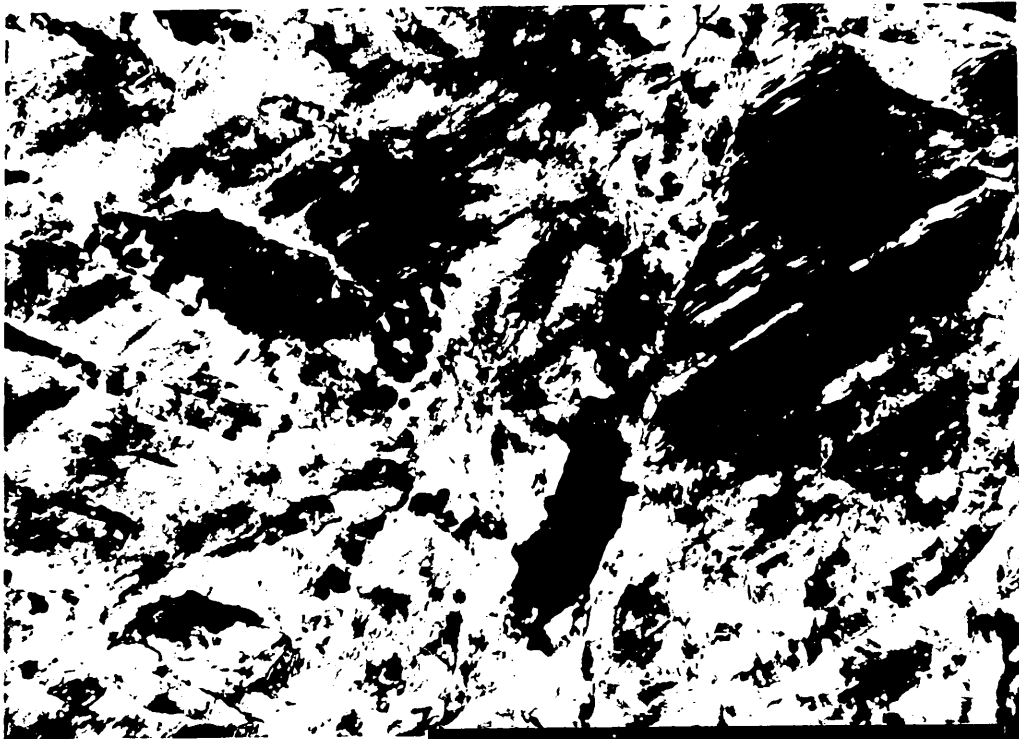


Fig.187. Dark field image of alloy E7 quenched and 18% deformed at  $-196^{\circ}\text{C}$  and aged 96 hrs at  $550^{\circ}\text{C}$ , showing finely dispersed precipitates. Mag X100,000

Fig.188. Electron diffraction pattern of  $\langle 100 \rangle_{\alpha'}$ ,  $\langle 111 \rangle_{\alpha'}$ ,  $\langle 110 \rangle_{\gamma}$  and hexagonal precipitate zones. ( $A_3B$  type).

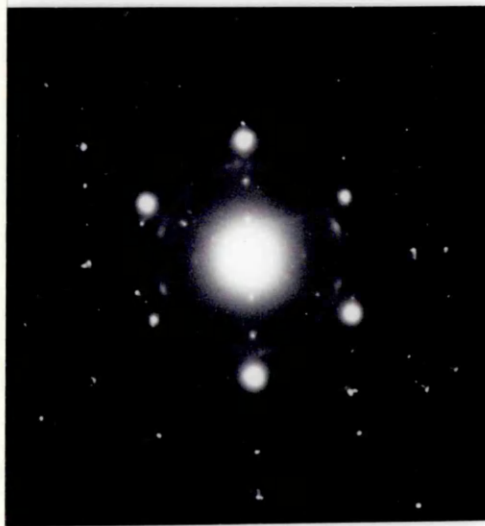
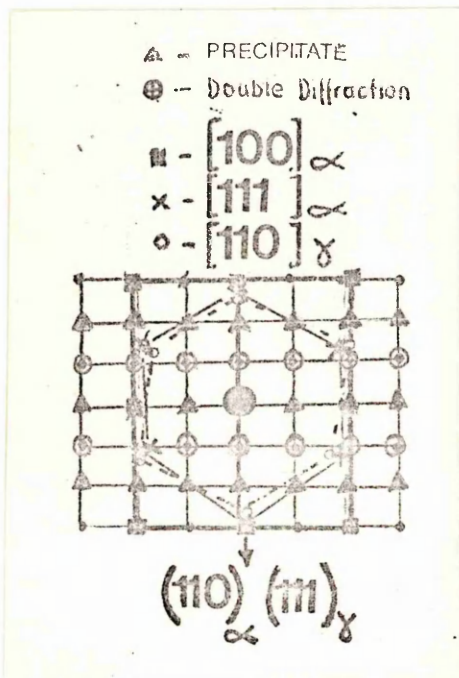
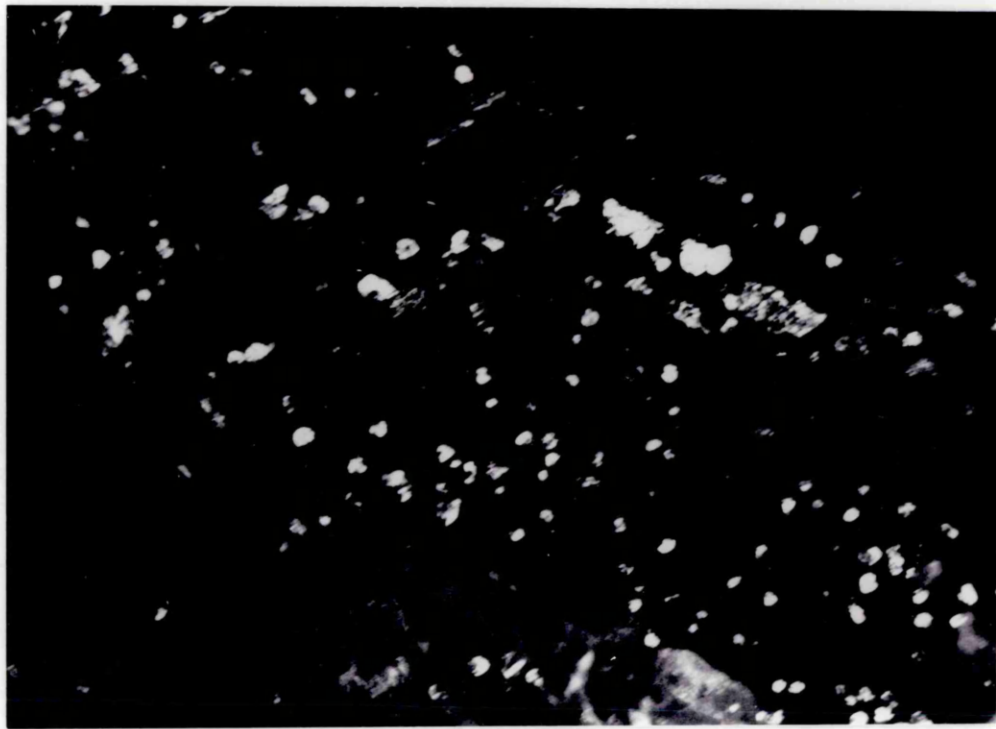


Fig.139. Effect of ageing temperature on the mechanical properties of alloys E2 → E4. (Ageing time 2 hrs).

Fig.140. Effect of ageing temperature on the mechanical properties of alloys E2 - E4 (ageing time 2 hrs).

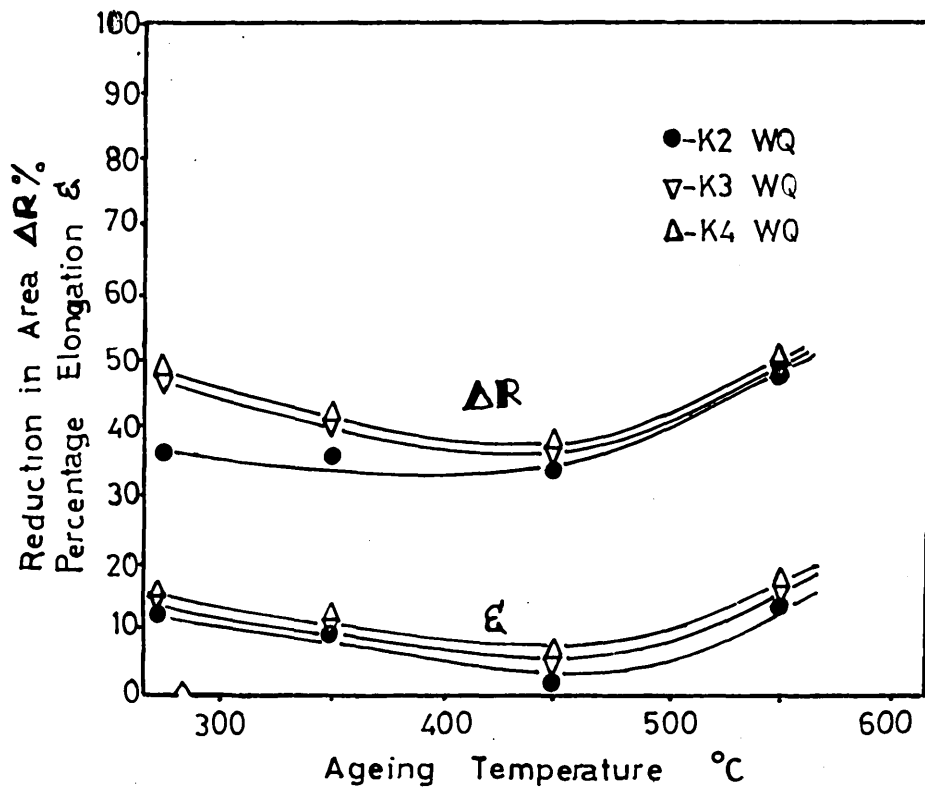
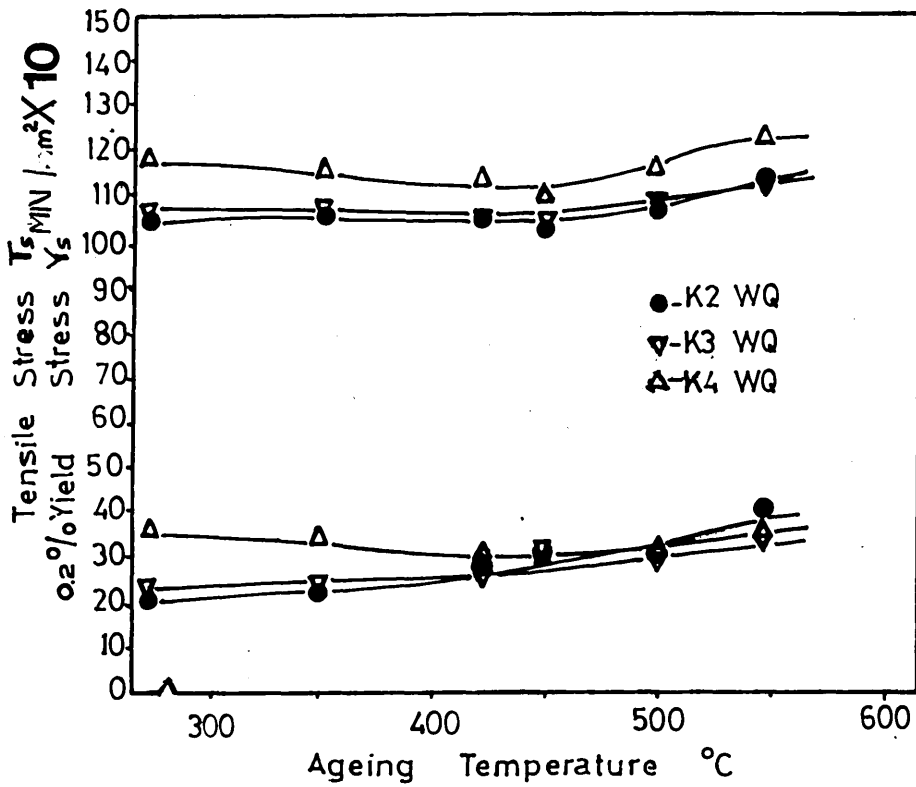


Fig.141. Effect of deformation on the mechanical properties  
of alloys H5 → H7

Fig.142. Tensile test piece design.

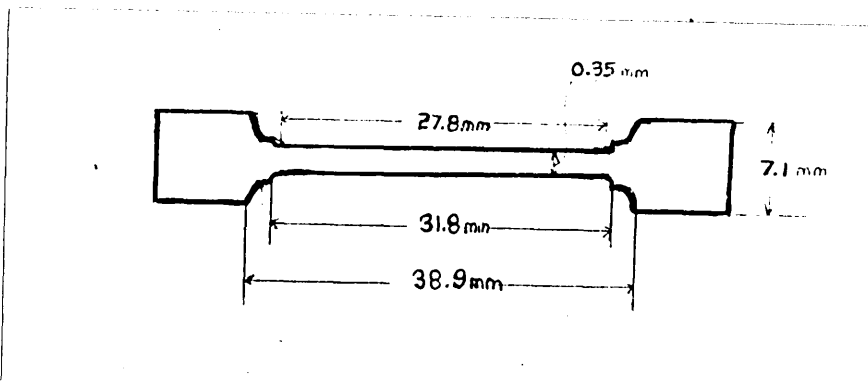
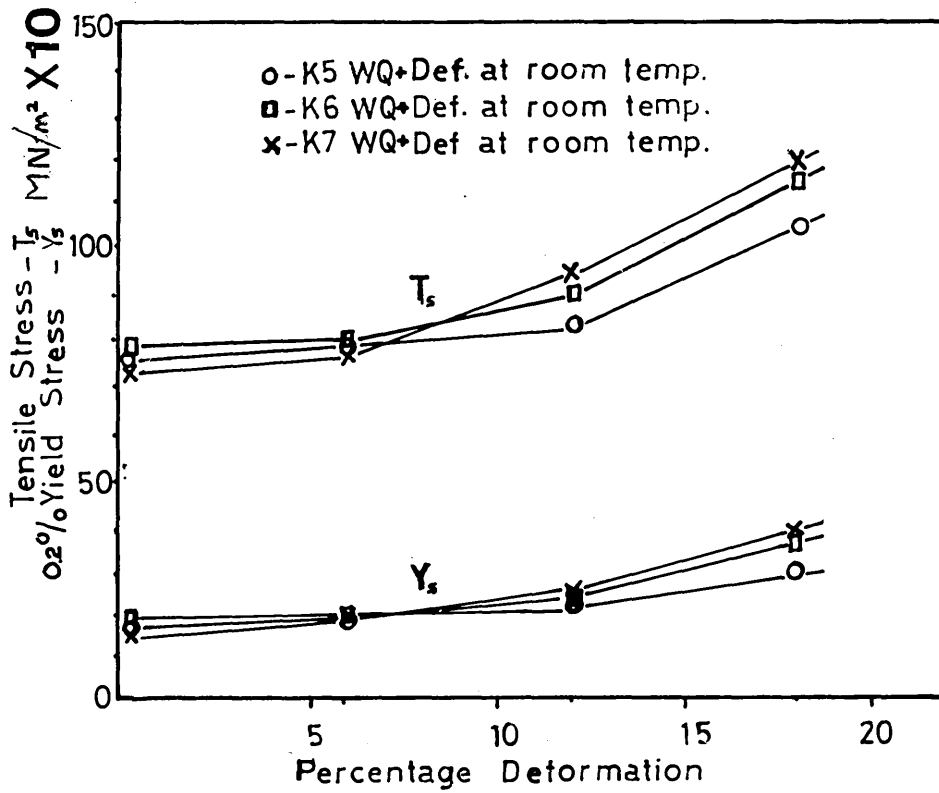


Fig.143. Mechanical properties of alloys K5 → K7. (Ageing time  
2 hrs).

Fig.144. Percentage elongation for alloys K5 → K7.

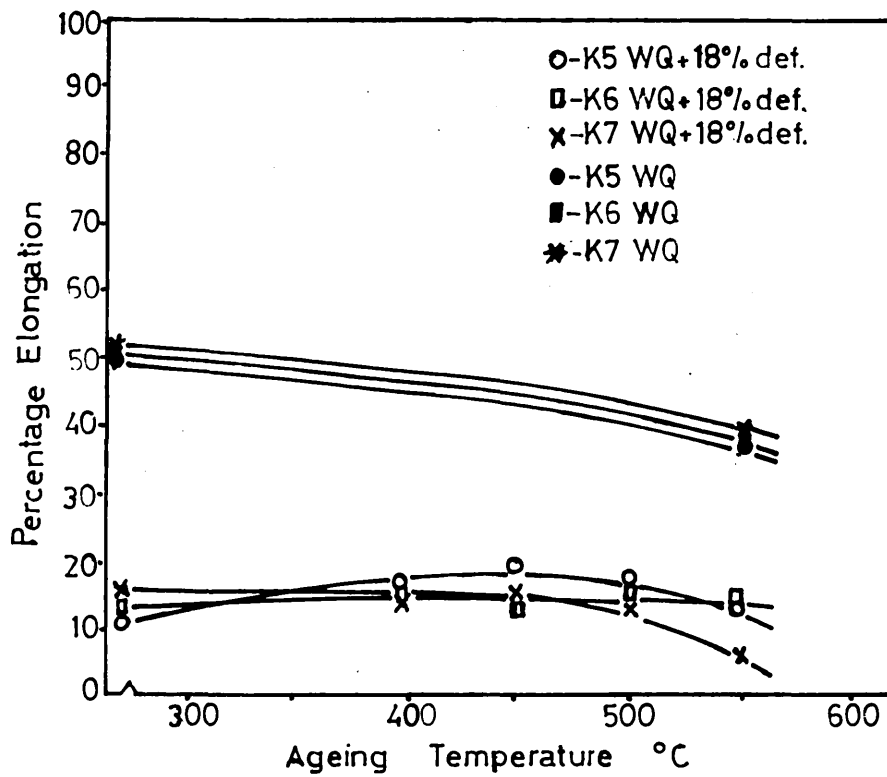
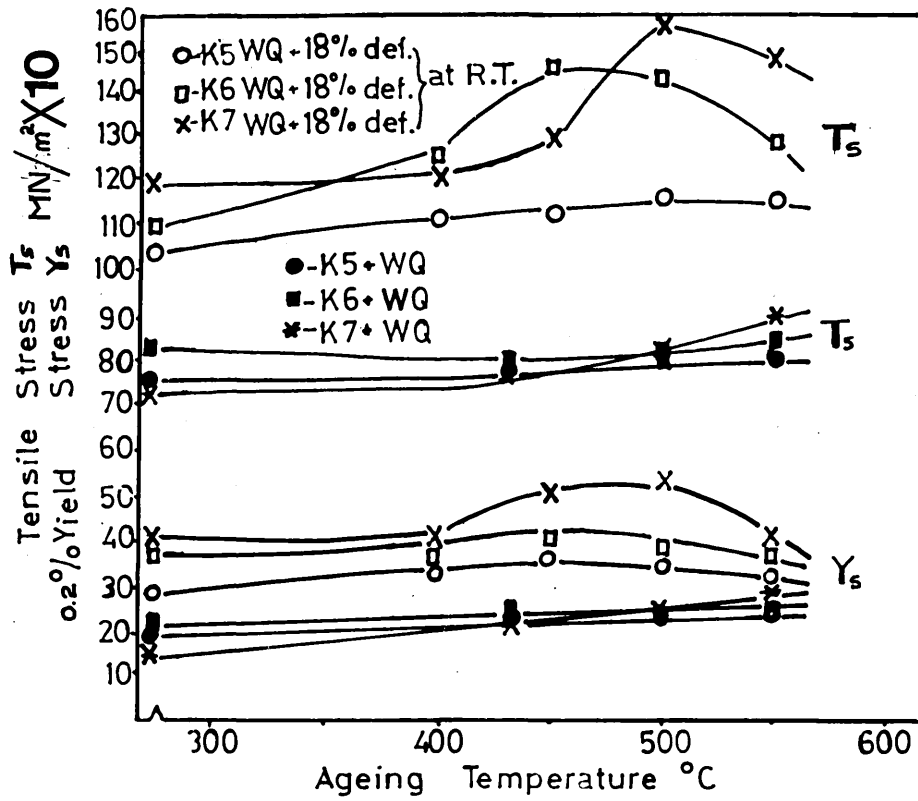


Fig.145. Impact properties for alloys K2 - K7.

Fig.146. Effect of ageing temperature on the impact properties  
of alloys K2 - K4. (ageing time 2 hrs).

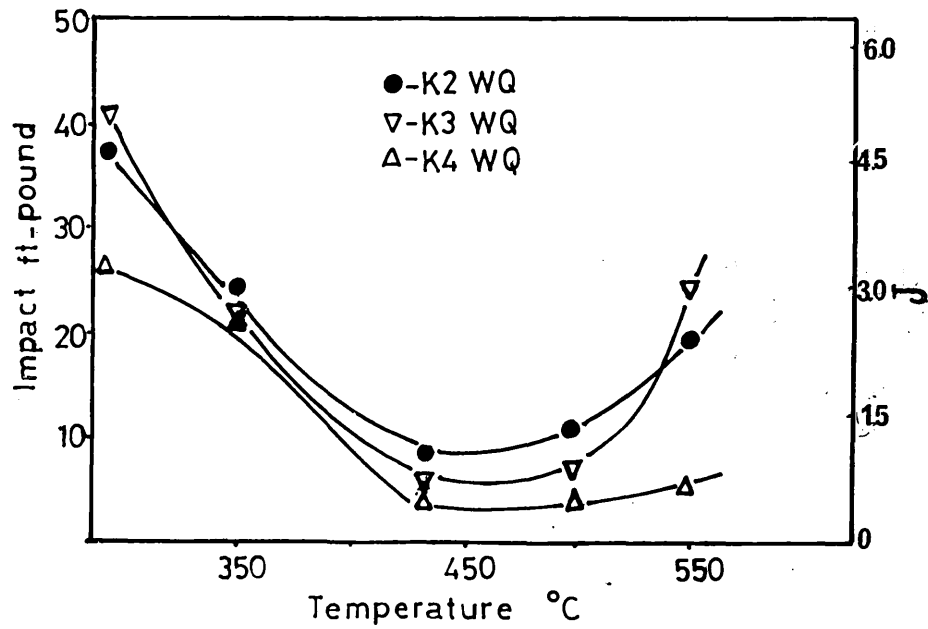
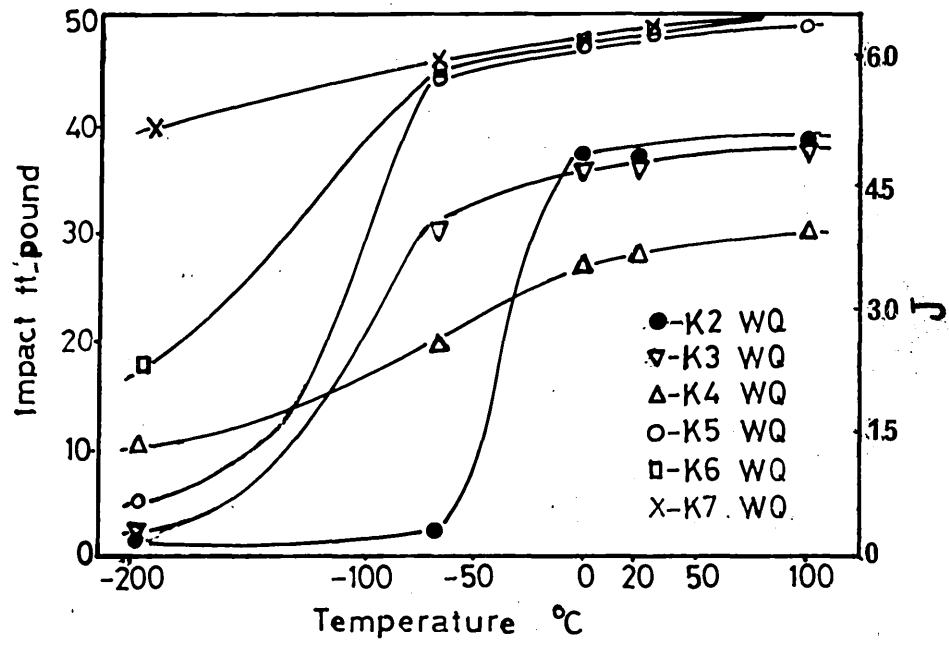


Fig.147. Impact properties of alloys K5 → K7 quenched and 18% deformed at  $-196^{\circ}\text{C}$ .

Fig.148. Effect of ageing temperature on the impact properties of alloys K5 → K7 quenched and 18% deformed at  $-196^{\circ}\text{C}$ . (ageing time 2 hrs).

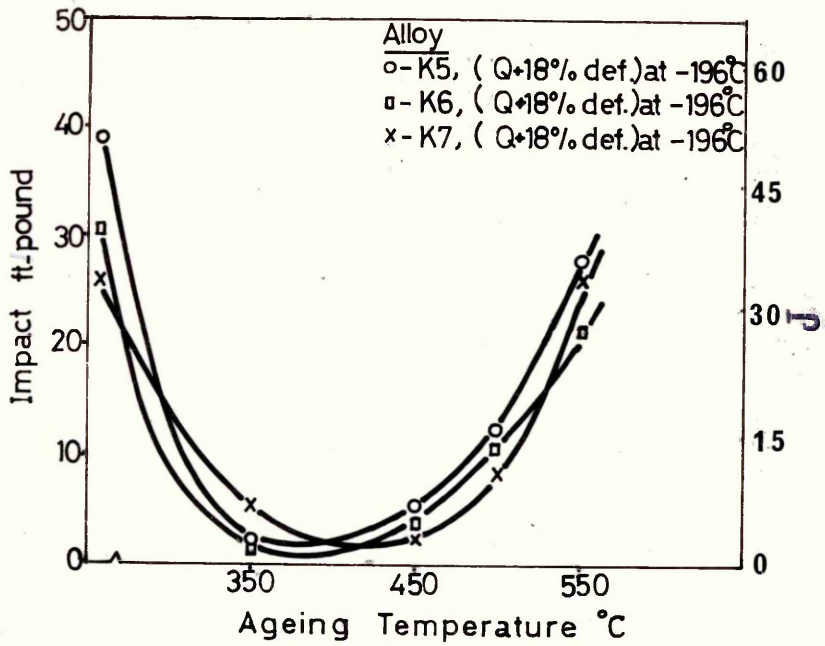
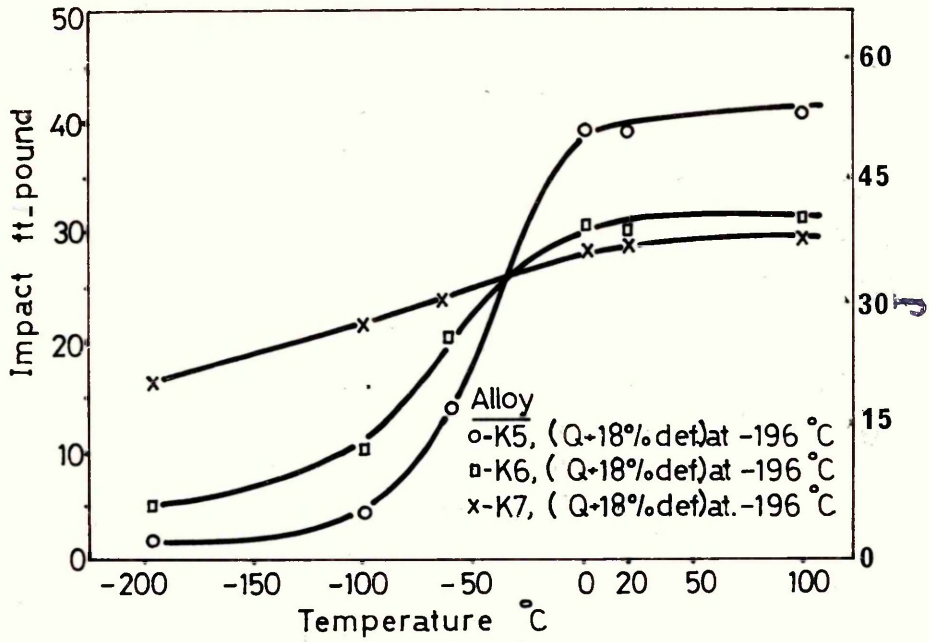


Fig.149. Stereographic traces for habit plane determination  
of alloy K3.

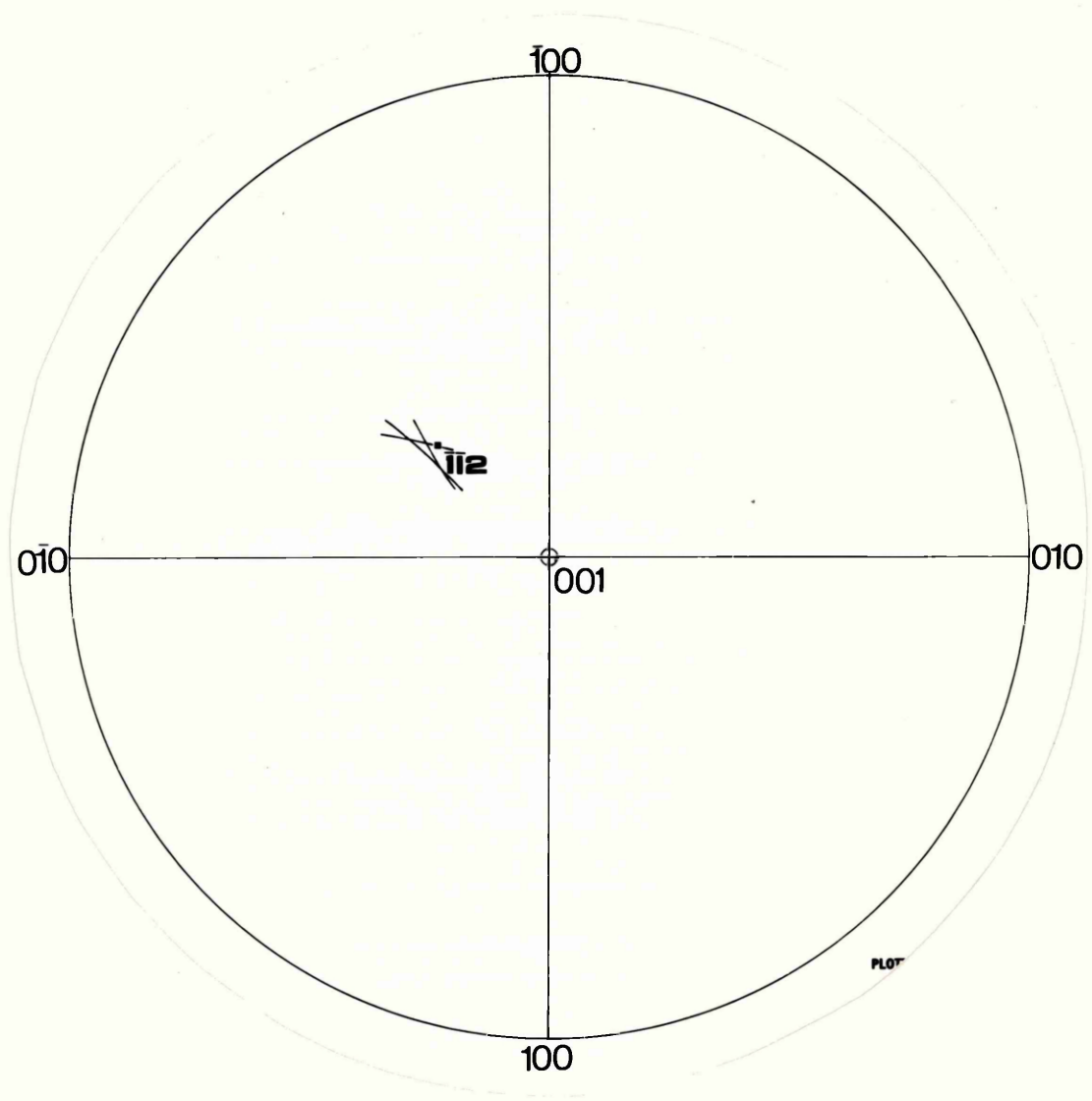


Fig. 150. Stereographic traces for habit plane determination  
of alloy K7.

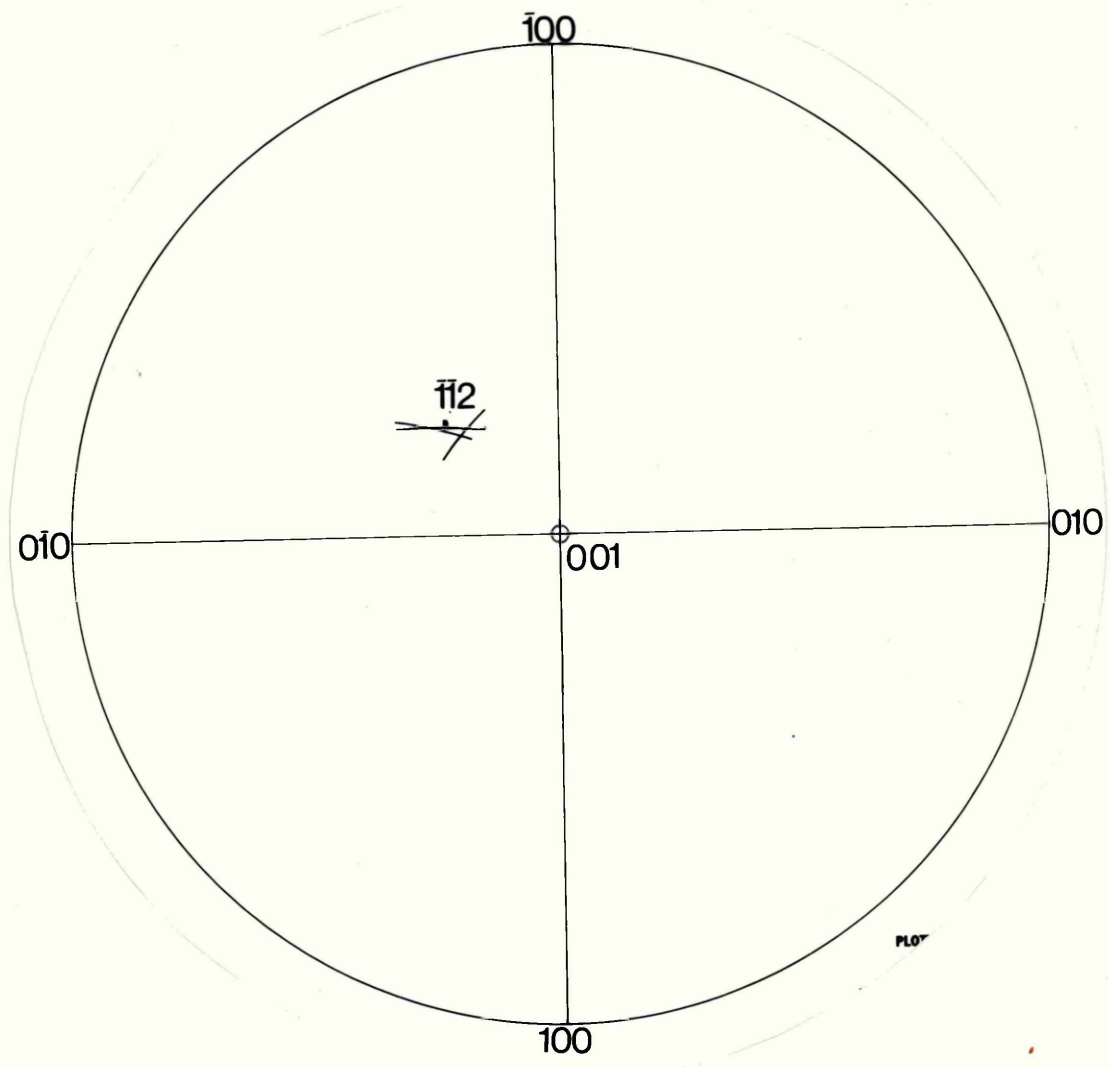


Fig.151. Atomic arrangement associated with the minimum atomic shifts required to produce a bcc unit cell from cph lattice. Shaded atoms are the cube corners, black atom is body centred. (49)

Fig.152. Contraction in  $\langle 10\bar{1}0 \rangle$  cph direction and expansion in  $\langle \bar{1}2\bar{1}0 \rangle$  cph direction produced by cph to bcc transformation.

